UNIVERSITY OF CALIFORNIA SAN DIEGO

"Advances in MultiOmic Liquid Biopsy Technology for Early Disease Detection, Diagnostics, and Monitoring"

A dissertation submitted in partial satisfaction of the requirements for the Doctor of Philosophy

in

Chemical Engineering

by

Benjamin Gabriel Sarno

Committee in charge:

Professor Michael J. Heller, Chair
Professor Dorothy Sears, Co-chair
Professor Sadik Esener
Professor Cheryl Saenz
Professor Geert Schmid-Schonbein
Professor Donald Sirbuly

2021

The Dissertation of Benjamin Gabriel Sarno is acceptable in quality and form for publication on microfilm and electronically:

University of California, San Diego

2021

Dedication

To my mentors colleagues and friends. To my family and especially Analissa Sarno, I would not have found my way without you.

Epigraph

"We cannot build a better world without improving the individuals. Each of us must work for our own improvement, and at the same time we must share a general responsibility towards all humanity"

-Marie Curie

Table of Contents

List of Figures

List of Tables

Acknowledgements

Chapter 3 in its entirety is being prepared for publication submission, *"On-chip Isolation and Mulit-Omic Analysis of Peripheral Blood Nanoparticulae" Benjamin Sarno, Jean Lewis, Jennifer Marciniack, Nicholas Lewis, Kendra Foster, Michael Heller. Lab-on-Chip.*

Chapter 4 in its entirety is being prepared for publication submission, *"Bacterial Outer Membrane Vesicles (OMV) as a Diagnostic Biomarker for Cancers" Benjamin Sarno, Corey Dombacher, Randall Armstrong, Michael Heller, Stuart Ibsen. Small.*

I would like to extend my sincere obligation to the people and institutions who have helped me through the completion of this body of work. Without the support of all of you, I would not have made it through these projects or the challenges within.

Professor Jan Talbot, thank you for your encouragement to start this process. For believing that I could change my path forward with hard work, commitment, and determination. You were the first one to help me believe it was possible.

Dr. Julian Ramirez, with me every step, til' the bitter end.

Professor Stuart Ibsen, I am still unsure what made you believe in something more. Thank you for urging me to reach further. You have forever changed my perspective of what I am capable of.

Professor Michael Heller, for trusting Stu's judgement, for supporting me through every step forward, and for being an incredible friend.

Dr. Jean Lewis, who's advice was always on target, who's patience was unwavering, and who's taste in lab music stood above the rest.

Biological Dynamics for helping with research funding and resources when we needed it most.

CEDAR Research Institute for funding my final work ideas and completion of my dissertation.

Dr. Augustine Obirieze, your dedication and perspective will always motivate me forward. Your friendship is invaluable.

Dana Jimenez, for all the last-minute petitions, special email exceptions, and late paperwork. Thanks for the help!

To all of my friends, family, and colleagues who helped me through.

And most of all, Tara Lafabregue Rodkey, through all my stubbornness. Thank you for fighting on with me.

Vita

2016-2021	**University of California San Diego, La Jolla, CA** Doctor of Philosophy, Chemical Engineering -Diagnostic Translational Technology
2016-2018	**University of California San Diego, La Jolla, CA** Master of Science, Chemical Engineering
2018-Postponed	**Rady School of Management, San Diego, CA** Master of Business, Innovation
2011-2015	**University of California San Diego, La Jolla, CA** Bachelor of Science, Chemical Engineering

Publications

Dielectrophoresis: Developments and Applications from 2010 to 2020

Advances in Multiomic Liquid Biopsy Technology for Early Disease Detection, Diagnostics, & Monitoring

Plasma Biomarker for Post-Concussive Syndrome: Pilot Study using an AC Electro-kinetic Platform

Electrochemical Attack & Corrosion of Platinum Electrode in DEP Diagnostics

On-chip Isolation and Mulit-Omic Analysis of Peripheral Blood Nanoparticulae

Method for in situ Mesocosm Water Table Manipulation in Amazon Peatlands

MultiOmic Biomarker Analysis of PDAC Cancer Patient Blood Samples ***Manuscript in preparation***

Bacterial Outer Membrane Vesicles (OMV) as a Diagnostic Biomarker for Cancers ***Manuscript in preparation***

Abstract of the Dissertation

Advances in MultiOmic Liquid Biopsy Technology for Early Disease Detection, Diagnostics, and Monitoring

by

Benjamin Gabriel Sarno

Doctor of Philosophy in Chemical Engineering

University of California San Diego, 2021

Professor Michael J. Heller, Chair

Professor Dorothy Sears, Co-Chair

The primary objective of this dissertation is to develop improve and expand the foundational electrokinetic technology available to the medical field. Dielectrophoresis (DEP), the movement of polarizable particles in an electric field gradient, is a unique and compelling method for manipulating biologic samples under both high and low conductance conditions.

Effective for particles ranging from nanoparticulate matter to cell clusters and complex biological samples from whole blood and cerebrospinal fluid to urine and tears. Where research has developed many new applications, one major limitation has been discovery and particle selectivity. While the phenomenon makes many, previously improbable interactions possible, the lack of control for fine differentiation between minor particle differences makes selective isolation and discovery difficult. The problems manifest themselves during damaging down-steam purification and target isolation processing. Strict attention to device architecture and electronic signal parameters offer greater degrees of control, but confounding and inevitable conditions like joule heating and electrothermal flow can make material of interest more difficult to protect. However, careful design and control of sample conductivities, wash buffer chemistries and collection protocols make explorative efforts a reality. This clarified potential may offer confidence to future researchers to apply the DEP phenomena to discovery-based explorative research efforts.

CHAPTER 1: Introduction

"Dielectrophoresis: Developments in Technology and Application From the Past Decade"

ABSTRACT:

The 20th century has seen tremendous innovation of dielectrophoretic (DEP) technologies, with applications being developed in areas ranging from industrial processing to micro- and nanoscale biotechnology. Of 2600 patents held by the United States Patent and Trademark Office, 106 were filed in 2019 alone. This review focuses on DEP-based technologies and application developments between 2010 and 2020, with an aim to outline the progress and to identify potential areas for future research. Broadly, this review covers DEP research, with focuses on theory, technological development and biotechnology-based applications. Greater emphasis is placed on reviewing applications, as theory of basic device operation has matured and the field remains largely empirical due to difficulties in modeling biological systems. Specific DEP topics covered include: cell sorting devices; virus and bacteriophage manipulation; blood biomolecule isolation; nanoparticle isolation; DEP nanofabrication; and liquid DEP.

Dielectrophoresis is a physical phenomenon, but as a tool leveraged by engineering and imaginative scientific design, offers unique capabilities that may help solve unresolved problems. Biotechnology likely offers DEP the greatest promise, as it demands more robust, more selective processes with versatile and timely automation. Innovations in reagents, along with more precise reaction protocols, all-in-one processes will advance DEP into the organ-on-a-chip and lab-on-chip technology spaces. Though publication rates and content communicate a maturing of the

field, in a broader sense, DEP is adolescent at best. The developments of this decade will continue to evolve and with complimentary advances in chemistry, material science and engineering, build optimism for the field moving forward.

INTRODUCTION:

Nearly 2600 years stand between today and the initial Greek postulates of the dielectrophoretic phenomenon, with scholarship beginning in earnest in the 1930's and industrial applications taking root in the 1950's [1,2]. Like many electrical phenomena, the theoretical underpinnings found in Maxwell's theories of the mid-19th century flourished in the early 20th century. Hundreds of applications have been developed, ranging from industrial processing to micro and nanoscale biotechnology, since H.S. Hatfield developed a dielectric separation technique and built a pilot plant to use the phenomenon to separate cassiterite from quartz [3]. A cursory Google Scholar search for "dielectrophoresis" produces nearly 29,700 entries since 1951 when the term dielectrophoresis was first coined by H.A. Pohl in his paper, *"The Motion and Precipitation of Suspensoids in Divergent Electric Fields"* [4]. More notable is the commercial promise of dielectrophoretic-based technologies, with over 2600 patents held by The United States Patent and trademark Office (USPTO), and 106 filed in 2019 alone.

Spurred on by a few seminal papers preceding 1990 and the maturing of industrial processes, biotechnology applications have led the dielectrophoresis (DEP) field for the past 30 years, e.g. 20 of the latest 21 United States patents for DEP coming from biotech origins. Figure 1 shows the distribution of publications and United States patent holdings since 2010 from PubMed and The United States Patent Office and Trademark websites, respectively[5,6]. The bulk of patents and publications before 2010 were nascent discoveries of range and potential, whereas much of

translational progress in DEP has occurred in the past ten years. Yearly publications steadily increased between 2000 and 2010, while the annual publication content across 2010-2020 remained relatively constant, with two spikes in 2015, and 2019 (respectively a 21% and 37% increase over the decade's average. The very same PubMed, open source search for "Dielectrophoresis" produces a total of 112 results from 1951 to 2000, followed by 613 from the 2000's, and 981 publications from 2010 to present day. Figure 2 shows the categorized distribution of publications across all three decades. There has been a shift from fundamental DEP technology development to more of an applications focus, with a nearly 20% increase in application patents across the two decades[5]. This change in publication distribution shows a maturity in DEP fundamentals, while new applications remain abundant.

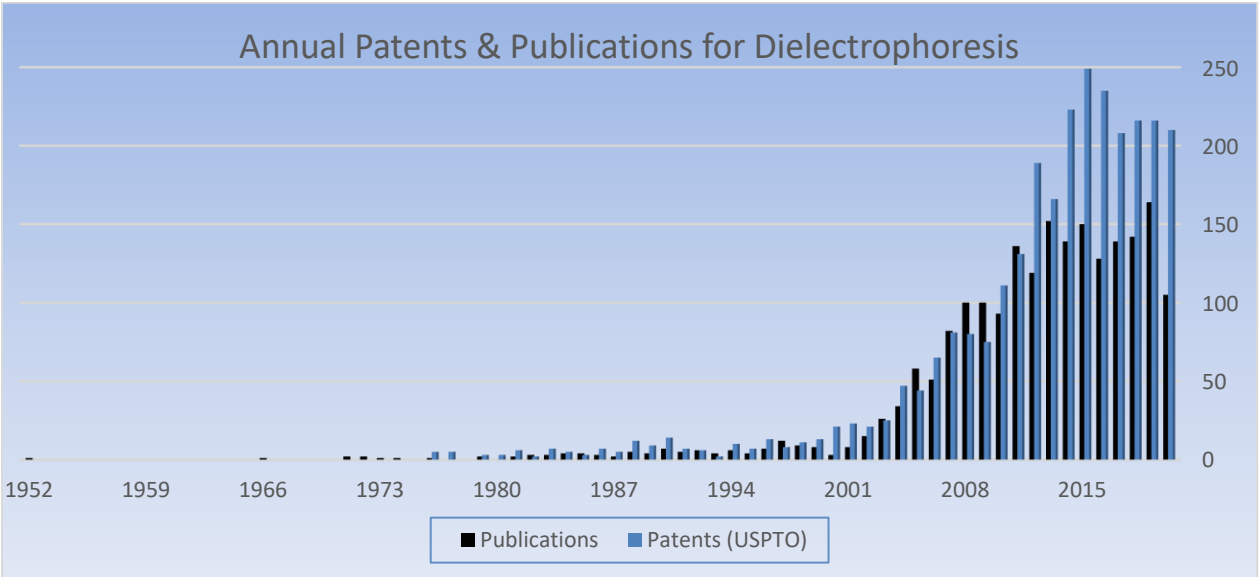

Figure 1.1: An overlaid distribution of patents and publications in the DEP field, starting with the 1952 Pohls' industrial process and up to March 2020. Statistics were taken from PubMed, open source, date restricted search for *"Dielectrophoresis"* and a date restricted search of the USPTO database for *"Dielectrophoresis".* There was a large rise in annual patents and publications between 2000 and 2010, which has maintained relatively constant through this past decade.

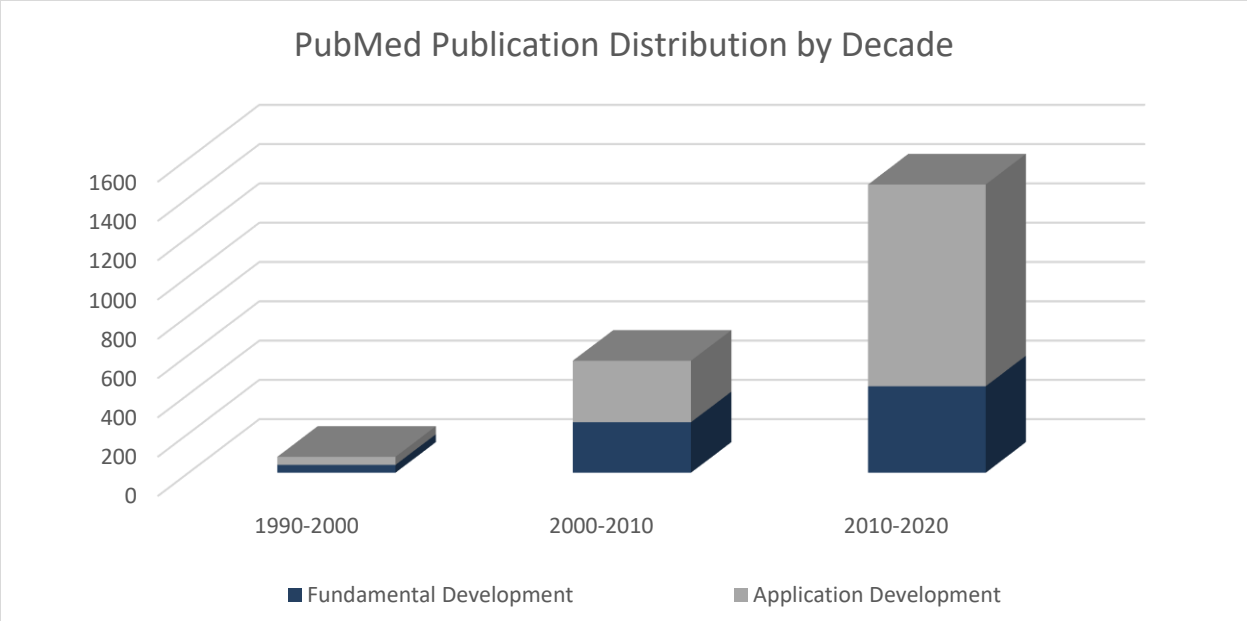

Figure 2.1: The categorized distribution of publications across three decades. Data from the USPTO shows a clear shift from fundamental DEP technology development to a clear focus on applications with nearly 50% of the DEP publications were application-based in the 1990's, rising to approximately 55% between 2000-2009 and to 70% of the publications for the 2010-2020 decade.

This review focuses on work of the past decade to outline the progress of DEP-based technologies and applications, in hopes that it may serve as a guidance moving forward. This review will examine theory, technological developments, DEP-based biotechnology applications and novel research into DEP-based nanotechnology. The greatest emphasis is placed on applications, as theory of basic device operation has matured and the field remains firmly empirical due to difficulties in modeling biological systems. Specific DEP topics include: cell sorting devices, virus and bacteriophage manipulation; blood biomolecule isolation, nanoparticle DEP, DEP nanofabrication, and liquid DEP. Other recommended, DEP-centric reviews focused on different time periods, applications, theory, and technological aspects are widely available [7–12].

BACKGROUND/THEORY:

It is important to begin with the basic principles, as they provide fundamental context for all the advances in computer modeling, fabrication techniques, and materials science that have been realized in the past decade. Dielectrophoresis is the movement of uncharged particles through a medium as a result of a non-uniform electric field. Classic, time-averaged, DEP theory is based on applying Maxwell's equations to a homogeneous, single particle in a semi-infinite medium where the electric field gradient across the particle is small. Within this approximation, the equation reduces to the following equation, with positive values signifying a force towards an increasing electric field gradient.

$$F_{DEP} = 2\pi\varepsilon_m R^3 Re[CM]\nabla(E^2)$$

The terms are as follows: ε_m is the absolute permittivity of the theoretically infinite and homogenous medium, CM is the frequency-dependent Clausius-Mossotti factor relating to the polarizability of the particle and medium; R is the particle radius, and $\nabla(\mathrm{E}^2)$ is the gradient of electric field magnitude, squared. Unlike electrophoresis, which relies on a particle's charge, DEP force affects any material that can be differentially polarized from its suspending medium. The Clausius-Mossotti relation is a unitless number that quantifies the interaction between the particle and medium in terms of their respective complex polarizabilities, and determines the DEP force direction. It is written below in its complex form,

$$CM^* = \left(\frac{\varepsilon_p^* - \varepsilon_m^*}{\varepsilon_p^* + 2\varepsilon_m^*}\right) \; or \; CM^* = \left(\frac{\sigma_p^* - \sigma_m^*}{\sigma_p^* + \sigma_m^*}\right),$$

where both the complex permittivity (ε_p^*) and the complex conductivity (σ_p^*) are frequency dependent[13,14]. Conductivity terms tend to dominate the CM relation below ~50-100 kHz and

permittivity terms above ~1 MHz, with a transition region in between. The specific Clausius-Mossotti versus frequency relationship depends on the respective properties of the constituents of the system. For a given electric field gradient, DEP may exist at all electric field frequencies other than the crossover frequency, i.e. $Re(CM) = 0$, where there is no differential polarizability between the particle and the medium. It also marks a transition between positive and negative CM relation frequency regimes, so frequency selection provides an additional lever for particle manipulation. For example, mammalian cells in aqueous buffers have a negative-to-positive crossover frequencies in the range of 1-20 MHz, regardless the medium's conductivity. Other biological samples like bacteria, many phages, various vesicles, complex protein structures and nucleic acids largely exhibit a positive CM relation in the conductivity-dominated frequency range, even in high conductance media such as phosphate buffered saline (PBS) or plasma. It is important to note that this is a simplified model of dielectrophoresis that describes the first-order driving terms. Further For theoretical modeling and real consideration of these classical physical effects, are available in numerous electrical, micro/nano systems engineering and physics papers that will happily take you down the rabbit hole [15–18].

As alluded to above, biological particles are quite conductive, due to maintaining a static charge, so at DC, electrophoresis dominates any translational DEP effect. An AC signal is needed to temporally average out the electrophoretic force on the particle, and mitigates against ion screening, electrolysis, and electroosmotic flow. Frequency choice may also control the electrochemistry in some unique cases[19]. Additional factors may dramatically affect the electrical properties of the constituents as well, such as the local ion concentration in the medium or temperature of the system. For example, the relative dielectric constant of pure water is 80 at 25 °C and approximately 65 at 60 °C[20]. Joule heating and dielectric loss in the medium is significant

under high voltage operation, so substantial heating may occur, especially in mediums with high ion concentrations[21].

The system's electric field gradient (∇E^2) is heavily dependent on device geometry, providing an engineering opportunity to control particle trajectories. Due to the relatively low force magnitudes, DEP is largely used in quasi-static conditions, where the particles will collect into either the high or low field gradient regions, according to the conditions, rather than to actively transport a particle. For example, traveling wave DEP requires careful phasing across multiple interdigitated electrodes and flow-fractionation uses DEP to steer particles in a flow stream, both only under tightly controlled conditions [22–24].

Even within the "small, spherical particle" assumption generally applied for biological samples, particle size is a driving force in achieving particle selectivity[25]. Fluid drag is proportional to cross section, i.e. $F_{drag} \propto r_{particle}^2$, whereas $F_{DEP} \propto r_{particle}^3$, meaning that smaller equivalent particles are increasingly controlled by fluid forces, e.g. Brownian motion or convective currents, rather than by DEP forces, especially as particles shrink below ~50 nm [16,26]. The magnitude of the actual transient effects on cells and other large particles can be approximated from the creeping-flow limit of Navier-Stokes hydrodynamic flow equations under static conditions, but not in flow-focusing systems where the Reynolds numbers are generally in the range of 1-10 [16]. Despite this limitation, DEP's wide region of operation across a range of particle sizes (~10^{-8} - 10^{-3} m), materials, media, and dielectric properties, lend to its functionality [26–29].

TECHNOLOGY:

Despite the wide range of applications that dielectrophoretic-based devices can address, very little has translated out of the research lab to meet the demands placed on a commercial product. However, there are a select few laboratories and companies, at different stages of developing DEP-based systems, Dr. Ali Beskok of Southern Methodist University, Dr. Michael J. Heller of UC San Diego, Biological Dynamics in San Diego and Menarini-Silicon Biosystems, an Italian company, which appears to be the only one to have a publicly available product [30]. Broadly speaking, much of the research in biotechnology-focused DEP devices and applications has been more proof-of-concept research which have offered insight into the full range of versatility that can be accomplished within the engineering constraints of electronics, electrochemistry and device architecture. The impractical nature of most DEP technologies has however kept DEP-based biotechnologies from penetrating the market, at least to date.

While the fundamentals of DEP devices are well understood, complementary advancements in materials, chemistry, and engineering capability, are accelerating the pace of innovation in the field. This is especially true of increased access to multi-physics simulation software and supplemental computer aided design packages [31,32]. Similarly, new potential applications for DEP-based devices are growing rapidly with our developing understanding of fundamental biology and biochemistry; as well as new biotech laboratory tools and workflows. Greater than half the awarded US patents found under the keyword search for "dielectrophoresis" between the years of 2010 and 2020 are filings for coatings, buffers or methods applicable to DEP device technologies[6]. Of the remaining patents nearly half of these total filings represent electronic control modules, chip cartridges, housings, or incubators and not actual new device ideology. This closer analysis of the US patent trends for DEP technology across the last decade suggest that commercial focus is in implementation rather than fundamental development.

Menarini-Silicon Biosystems has developed a DEP-based bioinformatics platform that offers functionality for forensic and oncological research. This DEP microfluidic device can be used to sort single cells for diagnostic and prognostic cell analysis, as well as sample profiling [30]. The DEPArray NxT technology is the only DEP technology that offers a commercial, ready-to-order device that offers the recovery of pure single cells. The device is targeted and designed heavily towards personalized medical applications and combines microelectronic and microfluidic processing across a 300,000 micro well tray for ultra-high precision cell sorting and selection. Each DEP "cage" has the capacity to hold and manipulate a single cell by coordinating signals between the adjacent cages. The device allows for 2 different sample preparations sequences and methods that facilitate both live and dead/fixed cell processing. The microfluidic device offers a direct, all-in-one process stream that allows lab operators to input the cell suspension into the DEPArray cartridge and insert the entire device into the instrument for automated sample processing. With the signal introduction, cells are organized onto respective electrodes, and cells are registered in the software based on fluorescent labels added during sample preparation. The instrument allows for the selection of target cells, imaging, analysis, and comparisons within the mass sample. After processing and analysis, target cells are manipulated across the array plate with electrical signals and deposited into a collection or recovery tube for downstream processing and analysis.

The DEPArray device began in 2002 with the concept of electronic, or DEP, cages for the capture, control, and manipulation of a single microparticle [33–35]. The first prototype device was constructed on a simple printed circuit board and used Saccharomyces cerevisiae yeast cells to demonstrate electronic detection and manipulation of microorganisms. The original platform was evolved to a CMOS-controlled chip that allowed the group to achieve single cell resolution [34].

With this CMOS device, the Menarini group was able to achieve the first 20 μm x 20 μm DEP cage and successfully integrated on-chip actuation and sensing, allowing the capture and manipulation of immortalized cell lines, yeast clusters, RBC's and microbeads. This early prototype also enabled exploration of "flowless label-free cell separation". The first commercial targeted DEPArray system was developed between the years of 2006 and 2010, when the microelectronics and microfluidic platform were integrated together within a cartridge [36]. During this time, the Menarini group also developed the hardware and software for fluorescent imaging and analysis. The DEPArray V2 was introduced in 2014 and offered instrumentation and cartridge compatibility similar to their first-generation device, but with improved image-based single cell sorting processes, single cell resolution and 100% purity capabilities. The most current, DEPArray NxT, was released in 2016, and represents the third generation of the device. It focuses on a new framework that offers a more compact benchtop device instrumentation at higher performance[37].

The DEPArray NxT technology shows a capable sample processing ability with single-cell control and selectivity, making it a promising, flexible platform [30]. Unfortunately, the system requires expensive, proprietary instrumenttion along with complex imaging technology and software to operate as described, limiting access to well-funded research laboratories. The machine still requires complex and off-device sample preparation, increasing process variability and requiring a trained technician. The available sites are still too few to meaningfully sample rare cells, e.g. circulating tumor cells, thus conventional methods of enrichment are required. Continued development of the instrument, especially in automation, could lead to the first DEP-based technology to achieve real diagnostic and biotech market penetration.

The respective laboratories of Dr. Ali Beskok and Dr. Michael Heller have produced a longer-term series of promising results and show potential for the development of a marketable

DEP technology, which are described chronologically below. Beskok's group has designed and developed a DEP device using an interdigitated microelectrode, AC DEP device for biomedical and food safety applications. They started in 2008 with a focus on using a DEP-based technology for food security testing, beginning by studying colloidal particle motion with their new device. This research motivated a re-design using a box-shaped, castellated electrode layout, and the group redirected efforts after realizing the variability between foods demanded too much trial-and-error to be realistic [38,39]. In 2010, Ai *et al*. employed platinum electrodes and a unique nanochannel device architecture to achieve DC DEP induced particle transport [40]. In the same year, Koklu *et al*. further iterated on the square box, castellated microelectrode configuration to achieve nDEP capture of bacterial spores from *Bacillus subtilis* and *Clostridium sporongenes,* and demonstrated device use under biologically viable conductivities [41]. The latter enabled research in undiluted patient samples, rather than needing mitigate electrochemical damage through dilution of sample. In the same publication, the group demonstrated global electroosmotic fluid flow across the device interface. The group discussed implementation of an on-chip biosensor to allow for rapid detection, by immunostaining the captured material.

Seungkyung Park would continue progression of the application to high conductivity bioanalytics through 2011 working collaboratively with Dr. Samuel Young of Johns Hopkins Emergency Medicine. First, working on an all-in-one nucleic acid isolation and analytic device, Zhang *et al*. developed an eight chamber, multilayered device to electrokinetically isolate and process DNA particles for gene analysis [42]. Park *et al.* continued development of the high conductivity device, implementing a new multi-chamber, sequential flow microfluidic device with an angled linear gold electrode arrangement [33]. The device used positive DEP to separate target cells from sample buffer to selectively draw *Escherichia coli* to a collection chamber and to allow

the remaining sample to flow through into a waste chamber. Simultaneously, Beskok's group continued to develop the microfluidic and electrokinetic design to improve cell separation and cell sorting technologies, along with examining impedance spectroscopy methods for quantitative biology. Sabuncu *et al*. used a castellated electrode design to selectively separate and capture B16F10 clonal mouse cells, based on melanin concentrations [34]. In the same study, an impedance spectroscopy device, using a 4-electrode chamber design, was used to interrogate T-cell leukemia Jurkat cells.

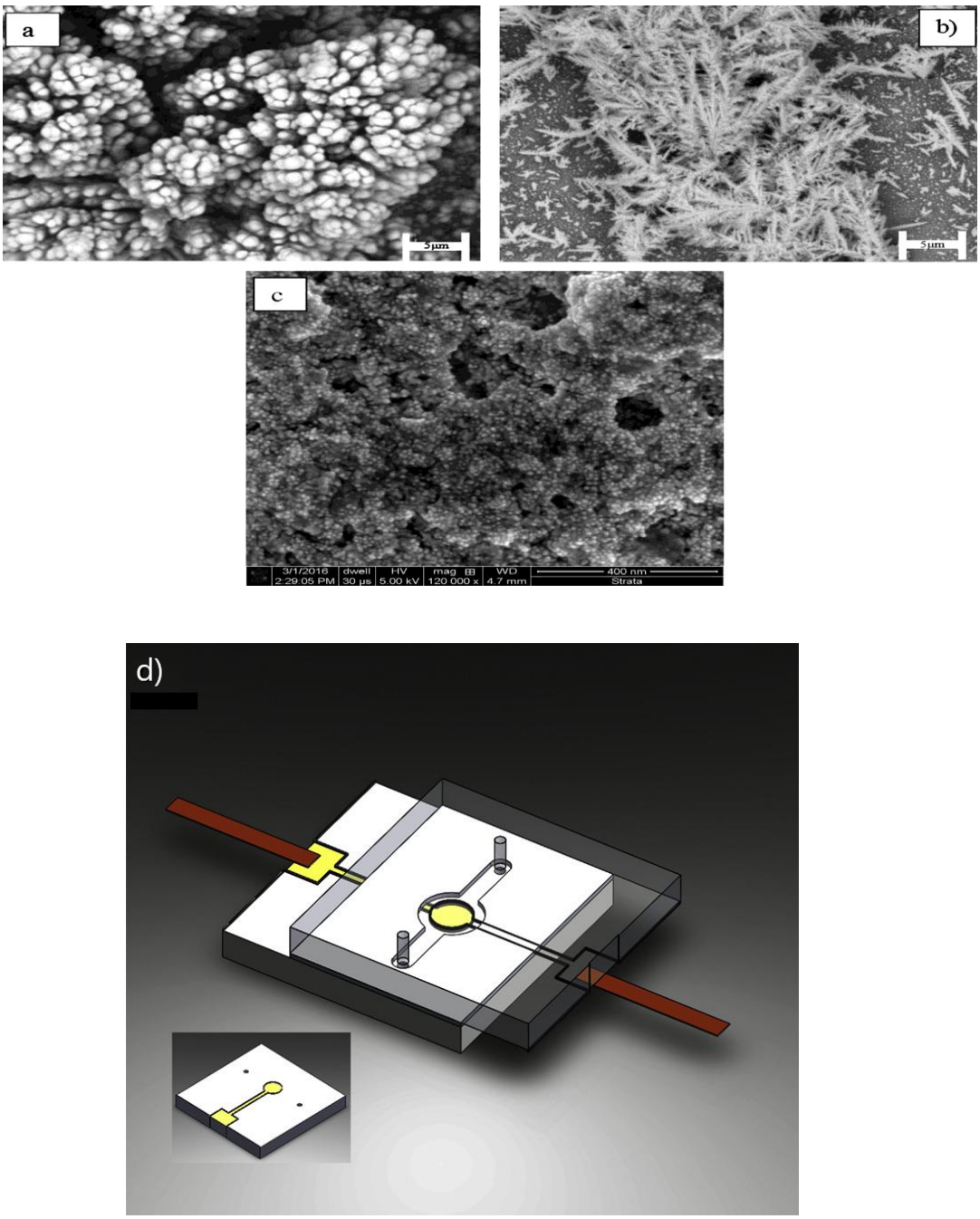

Figure 3.1: Koklu *et al*. SEM images of a) platinum black electrode, b) gold nanostructured electrode and c) gold granulated electrode d) A rendering of the microfluidic device. Two electrodes (4 mm diameter) aligned on top of each other. A double-sided tape formed the microfluidic channel where sample was introduced via pipette. *(Courtesy of: Electrochimica Acta, 2016)*

The group further developed their impedance spectroscopy device by studying the silicon-water interface [35–39]. In an effort to improve the particle impedance measurements, Koklu *et*

al. used a rough, or granulated, electrode to increase the sensitivity of their low frequency impedance measurements [48]. They further reported a greater biocompatibility between granulated gold nano-electrodes and the leukemic Jurkat T-cells as compared to platinum black electrodes, which also simplified device construction. Koklu *et al*. then demonstrated low conductivity DEP enhancement with fractal gold nano-electrodes, combining their optimized, rough electrodes with the box-shaped, castellated electrode configuration [49]. *Saccharomyces cerevisiae* yeast cells were manipulated using a 1 V_{pp}, 5 MHz signal to minimize electrothermal effects. The group used their dielectric spectroscopy method to optimize frequency ranges to achieve the most effective DEP forces. Most recent is their DEP microwell microfluidic cell sorting device, published in 2019. Mansoorifar *et al.* constructed a series of cell capture and characterization devices utilizing a SU-8 epoxy microwell array (30 µm microwell diameter) with their well-developed gold electrode impedance platform [50,51]. The device was used over an 8-hour window with low conductivity buffers to determine cell viability versus necrosis of PC-3 prostate cancer cells and 100 µM Enzalutaminde. The performance improvements as result of incremental development of their chips offer the possibility of a system designed to quantify drug efficacy in high conductance samples.

A series of developmental successes from the Dr. Heller laboratory at the University of California San Diego (UCSD) Bioengineering and Nanoengineering Departments ultimately resulted in a commercial DEP device designed to isolate small particles out of biological fluids. Nanogen, a San Diego based company called cofounded by Dr. Heller, began fundamental work on electrokinetic microarray technologies in the early 1990's, which was among the first application of microelectronic and photolithography techniques to biotechnology and biomedical diagnostics. These early microarray devices, operated mainly at DC, used electrophoresis to

spatially manipulate DNA probes, creating configurable regions of "electronic hybridization" and "electronic stringency" [52–55]. The primary focus was the DNA genotyping of point mutations for cancer, genetic and infectious diseases [56–58], but later work experimented with DEP by using the microarray devices with an AC signal to prepare biological samples and separate cancer cells [59–61]. Unfortunately, the DEP separations required considerable dilution of the samples, making the technique interesting but not yet viable for clinical diagnostics. Much of Nanogen's intellectual property came with Dr. Heller as he transitioned to UCSD, and this early work set the stage for future efforts directed at overcoming DEP's high conductance limitations.

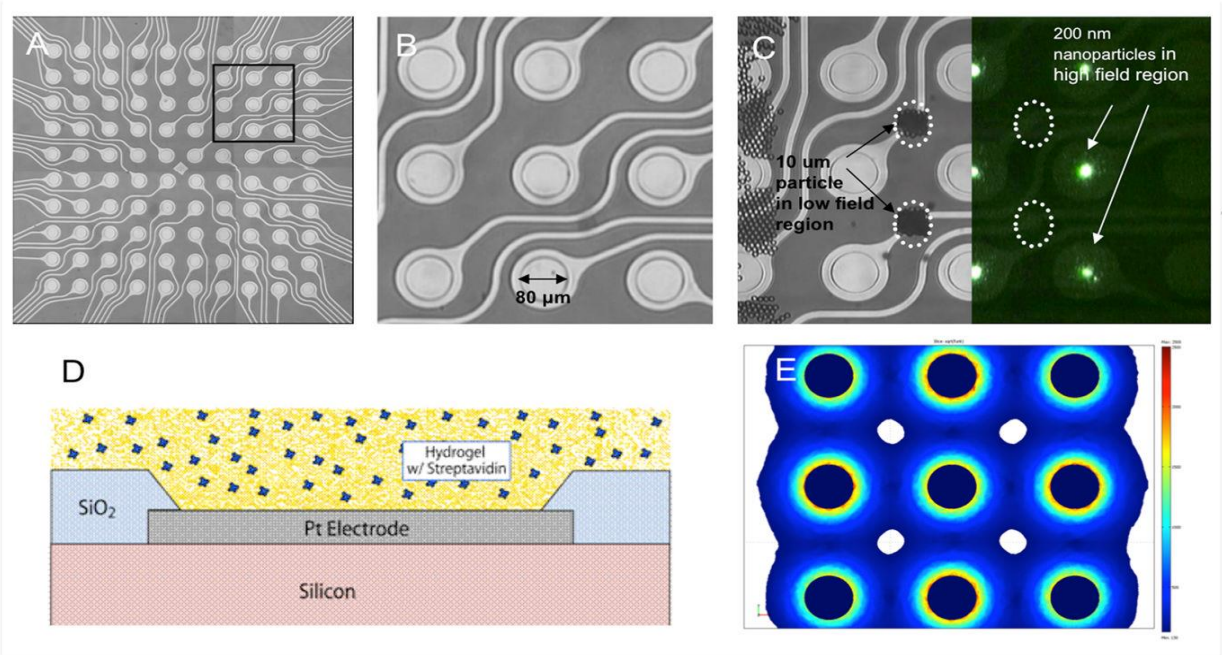

Figure 4.1: A) Early iteration of the Heller lab device, 100 platinum electrodes microarray. B) 3×3 subset of microelectrodes. C) Composite image of half bright field/ half green fluorescence showing the separation of 10µm particles into the low field regions and the fluorescent 200nm nanoparticles in the high field regions D) Cross-sectional diagram of the original microarray design lay-up. E) Early COMSOL Electric field rendering for the microarray displaying high field positive DEP regions on the electrode edges and negative DEP regions represented by the white circles. *(Courtesy of: Electrochemistry Communications, 2009)*

The terms electronic hybridization and stringency were used to describe the function of the device. The primary applications were for DNA genotyping of point mutations for cancer, genetic and infectious diseases[61]. In later work, these microarray devices were also used in the AC mode to carryout DEP for sample preparation of bacteria from blood, and for cancer cell separation applications[54,59]. Unfortunately, the DEP separations required considerable dilution of the samples, making the technique interesting, but not viable for actual clinical diagnostic applications. However, this earlier work demonstrated the conductance limitations of DEP and helped set the stage for future efforts directed at overcoming that problem.

Continued developments of this device with a microarray of circular electrodes, powered in a checkerboard pattern, were discussed in 2008, 2009 and 2011, showing microparticle isolation and nucleic acid capture in high conductance media [62–64]. This research and respective patents resulted in the formation of Biological Dynamics in 2010. Sonnenberg *et al.* published in 2012 a demonstration of selective particle, high conductance, capture and isolation using the device [65]. They were able to achieve clear negative DEP migration of red and white blood cells and positive DEP collection of nucleic acid and protein nanoparticles on the periphery of the electrode's surfaces by diluting human blood samples with a high conductance buffer and applying 20 V_{pp} at 10 kHz. A paper in 2013 showed capture of stained mitochondria in a 1.46 mS/cm storage buffer and of stained bacteriophages spiked into whole blood [66]. The mitochondrial protocol required pre-staining of the mitochondria along with a significantly greater signal strength of 50 V_{PP} at 10 kHz for 30 minutes to achieve effective concentration and capture. In 2014, cancer related circulating cell-free DNA were extracted from leukemia patient blood samples (undiluted plasma and whole blood) using Biological Dynamics microfluidic devices [67]. The DNA was first isolated for 10 minutes using an 11 V_{pp}, 10 kHz AC signal, then rinsed for 10 minutes in 0.5x PBS while still under electrical stimulus. All DNA samples were then eluted from the device and processed through PCR amplification and sequencing.

Ibsen *et al*. continued with the same platform to test for drug delivery nanoparticle recovery from blood plasma [68]. A suspension of fluorescently labeled, silica shell nanoparticles in 1X PBS was spiked into human plasma at a ratio of 10 µL to 90 µL, respectively, and were interrogated using a 12 V_{pp}, 15 kHz AC signal. Both protein aggregates, viewed in bright field, and nanoparticle fluorescence became visible around 30 seconds post signal introduction. Fluorescent intensity began to plateau around 7 minutes and electrode saturation began to occur at the 10-minute mark,

whereupon the fluorescent images were taken. The group reported that a large amount of off-target protein, naturally present in plasma, coated the electrodes in aggregates and substantially limited the devices from capturing greater quantities of target nanoparticles.

Follow up experiments to this work measured the chip's capacity for exosome or extracellular vesicle (EV) capture [69]. Chronic Lymphocytic Leukemia plasma samples, spiked with concentrated exosomes from cell culture media, were tested at 10 V_{pp}, 10 kHz. EVs were isolated on-chip for 10 minutes followed by an in-situ 10-minute wash in 0.5X PBS, then dried to confirm EV capture by SEM imaging. Extracellular vesicles have been shown as important biomarkers for many diseases and continued work from this group focused on early detection and diagnostic devices for a number of cancer types [70].

Lewis *et al*. continued to use the Biological Dynamics DEP system to rapidly isolate extracellular vesicles (EVs) directly from undiluted whole blood, plasma, and serum; and then used in-situ immunostaining to quantify cancer biomarker expression [71]. After DEP collection and 0.5X PBS rinse, directly conjugated antibodies against the biomarkers glypican-1 and CD63 were flowed on to the chips without any additional processing steps. Twenty pancreatic ductal adenocarcinoma (PDAC) patient samples were identified from 11 healthy patient samples with a 99% sensitivity and 82% specificity. Glypican-1 was increased in PDAC and benign pancreatic diseased (BPD) patients relative to healthy patients. CD63 in PDAC was greater than the normal group but, within this small population, there were no statistically significant differences between BPD and normal groups nor PDAC and BPD groups. Also, ten colon cancer patient samples were processed and the three with metastatic diseases were identified. The difference between metastatic and non-metastatic were greater than the difference between colon and normal patients. This assay

was not capable of distinguishing between the confounding factors of increased biomarker-to-exosome ratios and increased number of exosomes. Additionally, there may be differences between cancer and non-cancer exosomes. Further development of the assay and the DEP system is needed to separate these differences.

Lewis *et al*. followed up with demonstration the DEP microarray platform in diagnosing glioblastomas and other brain tumors [72]. Similar protocols as applied by Lewis *et al*. were applied for seamless, on-chip EV isolation and immunofluorescent detection [17]. Glial fibrillary acidic protein (GFAP) and Tau were used as biomarkers to characterize meningioma, brain metastasis, and glioblastomas. First, patients without brain cancer were processed using the DEP device, and minimal or no immunofluorescence was measured. Next, aliquots of the respective blood plasma samples were spiked with EVs derived from the U87 glioblastoma cell line, where immunofluorescence showed high levels of both GFAP and Tau. Seventeen patients with tissue-confirmed glioblastoma, metastasis, or meningioma were then analyzed using the DEP chip system. These patients exhibited 65% higher GFAP and 94% higher Tau levels than the maximum observed in the control group. However, it is possible that neither GFAP nor Tau may be markers specific to glioblastoma, considering they were also detected in metastatic and meningioma patients. These biomarkers have also been reported to be expressed in patients who have experienced trauma, stroke, or Alzheimer's.

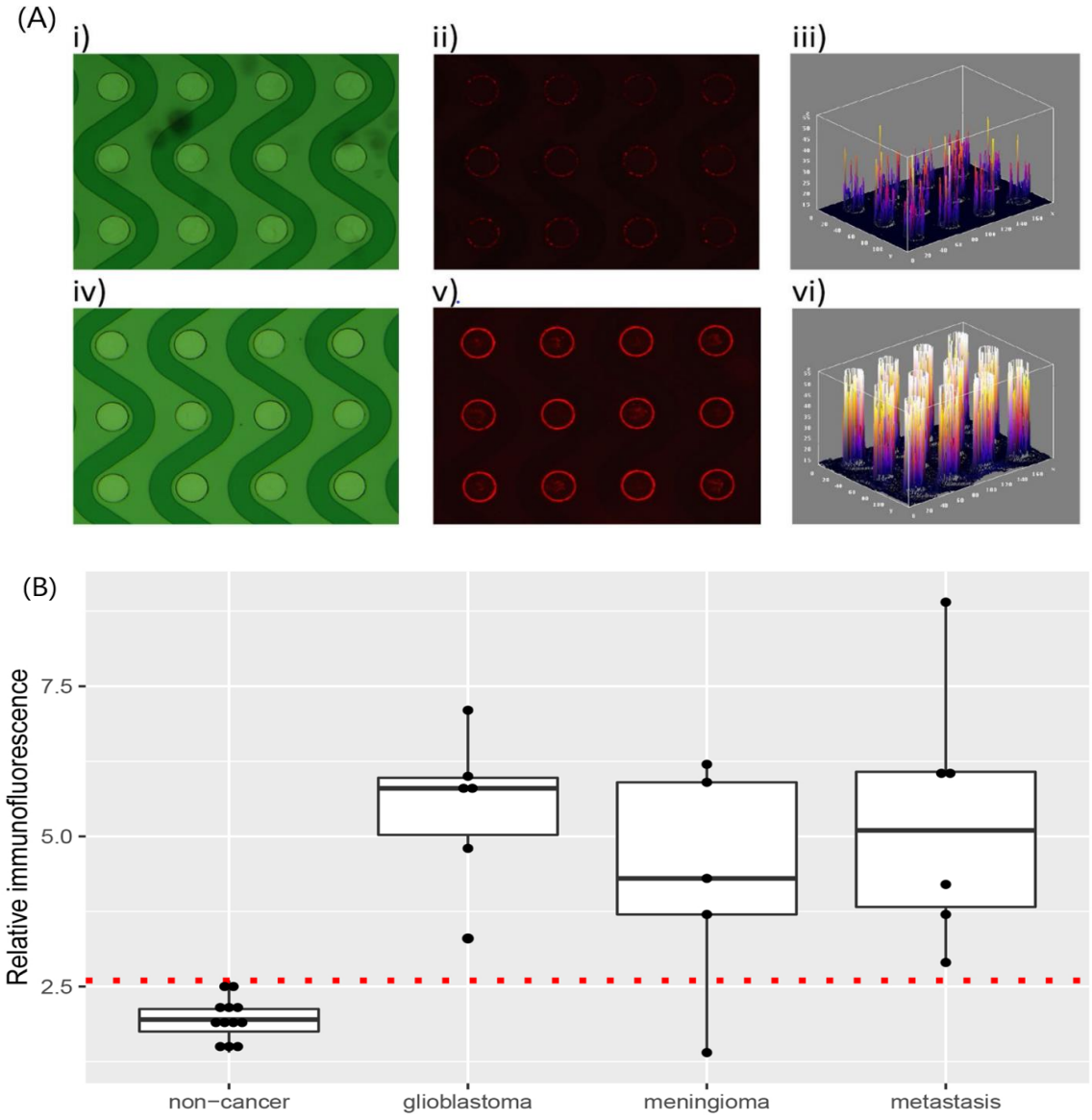

Figure 5.1: A) DEP-isolated EVs from brain cancer patient plasma (bottom row), but not normal plasma (top row), contain high levels of Tau. Plasma from a healthy donor (panels i–iii) or from a brain cancer patient (panels iv–vi) were each applied to a DEP chip. EVs immobilized onto the DEP chip were permeabilized with saponin, then positively labeled with anti-tau antibodies and visualized with Alexa Fluor 594-conjugated secondary antibody (red). Panels i and iv show the brightfield images for each chip; panels ii and v are the corresponding fluorescent images, and panels iii and vi are direct 3D projections for panels ii and v, showing relative quantitation. B) Tau: The red dotted horizontal line demarcates the discrimination threshold of 2.6 relative immunofluorescence units. Sixteen of 17 tumor samples (94%) exceeded this threshold. *(Courtesy of: Nature: Scientific Reports, 2019)*

The Heller group continued working on improving, expanding, and validating DEP devices and supporting assays. Heineck *et al.* explored the limits of DEP device function using two different architectures, with the end point being either electrode failure or sample degradation [19]. The group, testing sinusoidal signals across frequency and voltage, found that biological fluids and buffers, naturally corrosive and highly conductive, will degrade platinum electrochemically at low frequencies and cause the medium to locally hydrolyze and/or boil at high frequencies, with a transition frequency around 10 kHz. The study points to favorable frequency windows where targeted particle capture can be maximized while mitigating degradation of both the electrode and the target material. To prove the device durable, consistent, and dependable enough for clinical applications, device and protocol optimizations are continuously being performed alongside much broader, blinded patient diagnostic trials.

APPLICATIONS:

Yeast & Bacteria

A large amount of DEP research has focused on the manipulation and isolation of various particles within microfluidic platforms. While the array of particles investigated is wide, a significant emphasis has been placed on manipulating cells and single celled organisms. First achieved by Pohl and Hawk in 1966, the separation of live and dead yeast cells set a stage for thousands of biological experiments and hundreds of device designs, in the pursuit of a mammalian cell separation method and is still a relevant research topic today [10].

Zhao *et al*. developed an alternating current (AC) DEP microfluidic device for measuring lateral migration of yeast cells [73]. The device contains two metal electrodes separated from the main flow channel, which allows the DEP signal to selectively segregate differentiable cells.

Dielectrophoretic forces orient the cells along the sides of the insulated primary flow chamber where they flow through respective outlet orifices. The orifices are specifically fabricated on both insulating layers to have widths that vary by 50 μm and the asymmetry of these features produces an electric field gradient that spans the width of the primary flow chamber. Therefore, lateral migration can be controlled by selecting a frequency that splits cell populations with different crossover frequencies. This chip was used to determine a crossover frequency of 17 MHz for dead yeast cells and 43 MHz for live yeast cells. As both live and dead yeast cells flow along the center line of the primary chamber, applying a signal between these two crossover frequencies causes live cells move laterally towards the smaller orifice (high field gradient) while the dead yeast cells simultaneously migrate toward the larger orifice. This device shares a similar fundamental similar architecture to the original work by Pohl and Hawk, yet this unique device architecture allows for a one step isolation and collection.

Moving from yeast to bacteria, Chen *et al.* fabricated a microfluidic DEP platform that is capable of trapping, counting, and detecting Shewanella oneidensis. This device achieved rapid, label-free detection of S. oneidensis using a castellated, or interdigitated, electrode configuration with a central flow channel [74]. Observing with real-time fluorescence imaging and Raman spectroscopy, bacteria were trapped by positive DEP at an applied voltage of 3 V. A device developed by Su *et al.* uses a DEP device with a quadrupole electrode array to test the susceptibility of gram-negative bacteria to β-lactam antibiotics [75]. This DEP antimicrobial assay was tested using four standard strains and 78 clinical isolates, spanning 13 important gram-negative bacteria species. The minimal inhibitory concentrations (MIC) of cefazolin, ceftazidime, cefepime, and doripenem were determined using both their DEP assay and standard broth dilution testing. Morphological changes, including cell elongation, cell swelling, or lysis, were directly observed

in 90 minutes from susceptible, gram-negative bacteria under 1X MIC. The DEP and conventional assays were in 95.6% agreement with a major error rate of 2.9% for the DEP assay.

Cell Transfection

A unique application formulated by Chang *et al.* allows for improved bacterial transfection [76]. They were able to develop a versatile loading technique with gene editing, drug delivery, and molecule loading potential using a silicon, 3D nanochannel electroporation platform. This 3D nanochannel electroporation (NEP) device can precisely and benignly process 60,000 cells/cm^2 via a two-step transfection protocol. Positive DEP selectively positions and holds single cells in silicon nanochannels for subsequent electroporation; optimal conditions were found to be 50 V and 100 kHz. The difficult-to-transfect cell line NK-92 were tested on the 3D NEP-DEP device, resulting in placement of 79% of the cells in nanochannels and, of those cells, 93% were successfully transfected.

Cancer Cell Manipulation

Dielectrophoresis has offered some unique applications for cancer detection, diagnosis and treatment. Researchers have shown DEP-based devices selectively isolating target cancer cells based on their type and condition. Henslee *et al*. used a contactless DEP (cDEP) device to isolate breast cancer cells from a heterogeneous mixture of live cells [77]. Their study included MCF10A, MCF7, and MDA-MB-231 human breast cells which represented early, intermediate, and late-staged breast cancer, respectively, and each cell type exhibited distinct responses to the trapping signal. MDA-MB-231 cells were selectively isolated from a heterogeneous mixture of all three cell types at 20 V_{rms} and 30 V_{rms} over a frequency range of 180-210 kHz and 155-175 kHz,

respectively. Douglas *et al.* developed a microfluidic chip that coupled fluid flow with orthogonal DEP forces to displace and enrich cancer cell subpopulations expressing an aggressive phenotype [78]. cDEP was used to attract the cells with aggressive phenotypes to posts in the chamber. The mouse ovarian surface epithelial (MOSE) cell line was used to illustrate the device's ability to separate cells having genotypic similarities but varying levels of malignancy. Maximum trapping efficacy occurred at 350 V_{rms} and 30 kHz, with cells maintaining their viability after separation. Additionally, separating cells with similar bioelectric properties can be improved by optimizing DEP-drag force balance via flow rate. This device sets the stage for *in vitro* models that mimic the *in vivo* behavior of tumor evolution.

Soltanian-Zadeh *et al*. developed an insulator-based DEP (iDEP) device to investigate the response of cancer cells to drugs [79]. Their system selectively trapped breast cancer cell lines LCC1 and LCC9 and analyzed the effect of Obatoclax, an anti-cancer drug, had on these cells. Aliquots of cells were exposed to 100 nM, 500 nM, and 1 μM Obatoclax, with each increased concentration of drug exposure resulting in a higher crossover frequency for both cell lines. Untreated LCC1 had a crossover frequency of 700 kHz which increased to 900 kHz after introduction of 1 μM Obatoclax and LCC9's initial crossover frequency shifted from 100 kHz to 400 kHz with 1 μM Obatoclax. Trapping efficiency was altered by Obatoclax: at 900 kHz, untreated LCC1 cells had a 33% trapping efficiency, which increased to 56% with 1 μM Obatoclax treatment. At 1 MHz, the drug resulted in a decrease in trapping efficiency from 41% to a range between 27-36%. For LCC9, trapping efficiency went down with an increase in drug concentration between 100-800 kHz, but the relationship flipped at 900 kHz and 1 MHz.

Elitas *et al*. developed an electrochemically stable microfluidic chip using 3-D carbon electrodes, using a multi-step photolithography process on a silicon wafer, for cell characterization [24,80–82]. The electrode geometry was 100 μm tall and 50 μm in diameter, with a 15 μm spacing between electrodes. A 10^6 cell sample was made from U937 cultured cells suspended in a sucrose/glucose/BSA-low-conductivity buffer. The U937 monocyte's and macrophage's respective crossover frequencies were found to be 17 kHz and 30 kHz. They then characterized the monocyte/macrophage cell suspension under no-flow conditions using a series of tests across a range of frequencies from 1 kHz to 20 MHz. DEP cell separation was then established between the specific subpopulations using a 1 μL/min flow rate and a 10 V_{pp}, 30 kHz signal, yielding a 70% enrichment, as confirmed by fluorescently activated cell sorting (FACS) analysis.

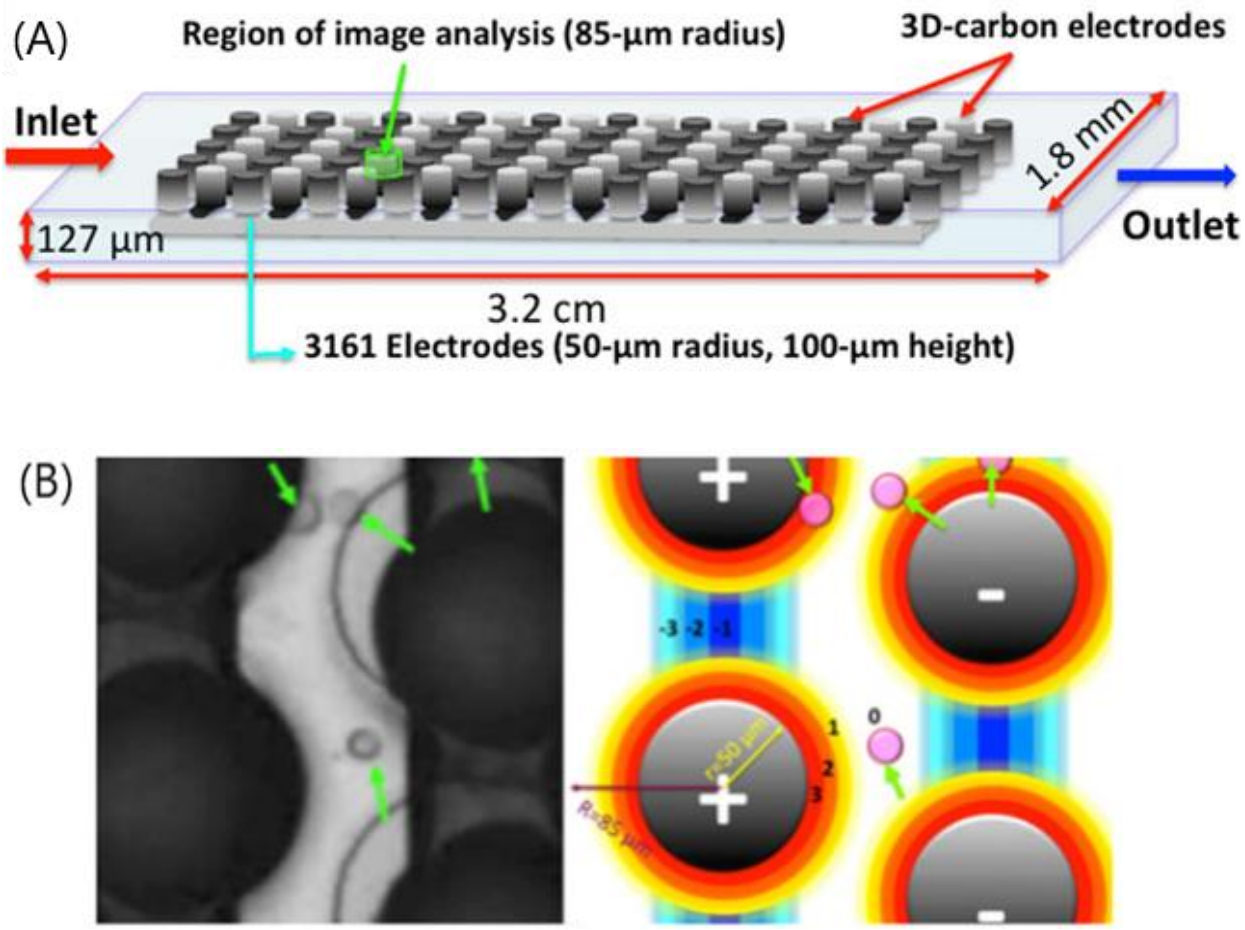

Figure 6.1: (A) Design of the 3D-carbon DEP chip. (B) Microscopic image of the cells exposed to DEP forces, and illustration of the image analysis performed for the captured image. *(Courtesy of: Electrophoresis 2019)*

Virus

Iswardy *et al.* fabricated a DEP microfluidic device for immunofluorescent detection of the dengue virus (DENV) [83]. Silica beads (1 µm) modified with mouse anti-flavivirus monoclonal antibodies were trapped via negative DEP. The device used a V-shaped guiding electrode with a U-shaped capture electrode and an AC signal of 15 V_{pp} at 1 MHz frequency, where the beads are repelled from the large electric field gradient at the guiding electrode tip. An additional drag force aided particles towards the capture electrode, and all the forces had to be balanced for successful

capture. Whole viral particles were captured by modified beads and Anti-DENV envelope protein antibodies and fluorescently conjugated donkey anti-rabbit IgG antibodies were utilized as fluorescent probes.

Ding *et al.* improved on a gradient-iDEP device which employs sawtooth-patterned insulating structures that incrementally decrease in pitch to concentrate the Sindbis virus [84]. Previous iDEP devices utilized gap distances that decrease from 945 μm to 27 μm by increasing the side length and width of the PDMS triangles. These devices generated sufficient electric field gradients to isolate bacteria and cells within the final three sets of gates. Instead, they fabricated a gradient iDEP device with a pitch that varies from 30 μm to 3 μm. This geometry creates a characteristic electric field determined by device architecture, which increases linearly throughout the channel. Due to particle size, these devices required significantly larger applied voltages to achieve direct viral capture compared to more traditional, bead-based virus isolation assays. Fluorescently labeled viral particles showed no obvious capture below 70 V, but fluorescent intensity consistently increased from 70 V to 200 V and stabilized above 200 V, indicating significant capture. The device showed 2x and 6x increase in Sindbis viral concentration as compared to immunofluorescent techniques, enzyme linked immune assays, western blots and green fluorescent protein binding. The device ultimately demonstrated direct capture of submicron particles using a DEP-based microfluidic device, eliminating the need for modified bead-based capture of viruses.

Blood-based DEP Separation

D'Amico *et al*. constructed a DEP isolation device using a quadrapole electrode configuration to isolate E. Coli from dilute, low conductivity, red blood cell/bacteria cultures[85].

The membrane-less microfluidic DEP dialysis system successfully isolated and concentrated *E. coli* and *Staphylococcus aureus (S. aureus)* bacteria using a label-free capture and wash assay. They cultured *E. coli/S. aureus* in human whole blood, selectively isolated red blood cells and bacteria; and then re-suspended red blood cells and bacteria into a dilution buffer solution. A permeabilization agent was added to the suspension and sample conductivity was then adjusted. The device leveraged the selective effect of the permeabilization agent on red blood cells, leaving *E. coli* and *S. aureus* unaffected. Researchers applied a 1 MHz, 15 V_{pp} AC signal to the device with a 10 μL/min flow rate. Under these conditions, the system successfully isolated 79 ± 3% of the targeted bacteria and they did not find any drop in device efficiency for any samples under 10^5 cells per process cycle. Quantitative PCR was performed to prove a 307-fold enrichment of bacterial DNA relative to the human DNA content in original specimen.

Bulk blood processing:

Given the prevalence of DEP microfluidic platforms for cell sorting, it is conceivable that it could be used for continuous, efficient, and high-throughput blood plasma isolation. High conductance limitations and dilution restrictions, which may lead to cell rupture due to osmotic imbalances, have handicapped the ultimate success of a lot of these technologies. Cell sorting for blood or near-biological buffers (~1.4 S/m) is unlikely due to dielectric loss factors at typical frequencies for cells. Exchanging cells into a lower conductance buffer introduces a number of steps, sources for error and places substantial osmotic pressure on suspended cells, reducing their viability. Other DEP blood processing devices that can operate at normal biologic conductivities are more limited by throughput capacity.

S. Yan *et al*. constructed a microfluidic chip using a series of layered flow channels that allowed for selective separation of red and white blood cells, leaving the main flow chamber with clean plasma, albeit blood had to be diluted before DEP separation to control sample conductance[86,87]. Yang *et al.* fabricated a DEP chip for continuous extraction of blood plasma from undiluted human whole blood, requiring no pre-processing steps and achieving nearly 100% purity and a plasma yield of 31% [88]. The device is comprised of a main channel with an additional, perpendicular side channel at its midpoint. ITO electrodes are placed adjacent to the side channel and repel red blood cells from continuing down the main channel using negative DEP. Hydrodynamic forces then push the red blood cells into the side channel while blood plasma flows unimpeded past the electrodes to the end of the main channel. This is achieved using a 20 V_{pp} AC signal with a 100 kHz frequency. Pure plasma was extracted from approximately 7 μL of whole blood in less than 15 minutes. Increasing the voltage past 20 V_{pp} or decreasing the frequency below 100 kHz may lead to burning the ITO electrodes. However, reducing the distance between the electrodes or fabricating electrodes with finer edge features could produce a greater electric field gradient with a lower operating voltage. More stable metal electrodes could replace ITO to allow greater processing power, but this device offers a way forward for future efficient on-chip blood plasma extraction. The group feels the external force and injection flow rate in this device could be optimized to meet the efficiency and throughput needs dictated by commercial and clinical applications of blood plasma extraction.

Cancer/Stem/Patterning

Alinezhadbalalami *et al*. fabricated a cDEP device with an array of insulating posts which was used to isolate prostate tumor cells with stem-like properties from other malignancies, and

separate aggressive ovarian cancer cells from early stage cells [89]. Additionally, the U251 glioblastoma cell line and its spheroid counterpart, SF-U251, were differentiated based on their respective dielectric properties. SF-U251 cells required higher voltages for successful trapping, but cells also exhibited greater crossover variance than the U251 cells. Also, the group demonstrated direct immunofluorescence of samples on the device. These two glioblastoma subpopulations expressed distinct difference in nestin and GFAP transmembrane expression, respectively, which may have led to the distinct DEP characteristics.

Tsutsui *et al*. developed a microfluidic iDEP-based device that uses an external flow to pattern mouse embryonic stem cells (mES) in poly(ethylene glycol) (PEG) microwells[90]. The microstructured hydrogel was patterned on a planar indium tin oxide (ITO) electrode and formed the positive DEP traps for the cells. The device achieved a seeding density of 10^7 cells/mL and successful cell trapping in less than one minute. Using live/dead fluorescence assays, it was confirmed that the isolated cells formed viable and homogeneous monolayers within the microwells, showing potential for future on-chip drug testing, complex tissue microenvironment testing, etc.

Bajaj *et al*. developed custom microelectrodes for DEP patterning of mES and C2C12 skeletal muscle myoblasts [91]. The DEP platform, running between 1-10 MHz, was coupled to a stereolithography apparatus to pattern and encapsulate mESs, mouse embryoid bodies, and C2C12 spheroids in hydrogels with physiologically relevant stiffness. 10 mm x 10 mm arrays of hydrogels were created, illustrating the ability to fabricate large three-dimensional microstructured cellular patterns. Cells exhibited a pearl chain structure after DEP pattering which allowed cell-cell contacts to be established and potential fate decisions to be investigated. Encapsulated mESs

showed a viability of 94% and 91% when patterned with conventional stereolithography and DEP-enhanced stereolithography, respectively. Next, mouse embryoid bodies and C2C12 spheroids were formed before positive-DEP patterning and hydrogel encapsulation. Live/dead assays evaluated after 1, 3, and 5 days showed the viability of the mouse embryoid bodies in the hydrogel, and demonstrating spatial organization of both mESs and cellular spheroids in the hybrid DEP-stereolithography platform. High throughput investigation of multi-cell and multi-material interactions that mimic the cells *in vivo* microenvironment can be achieved using this technology.

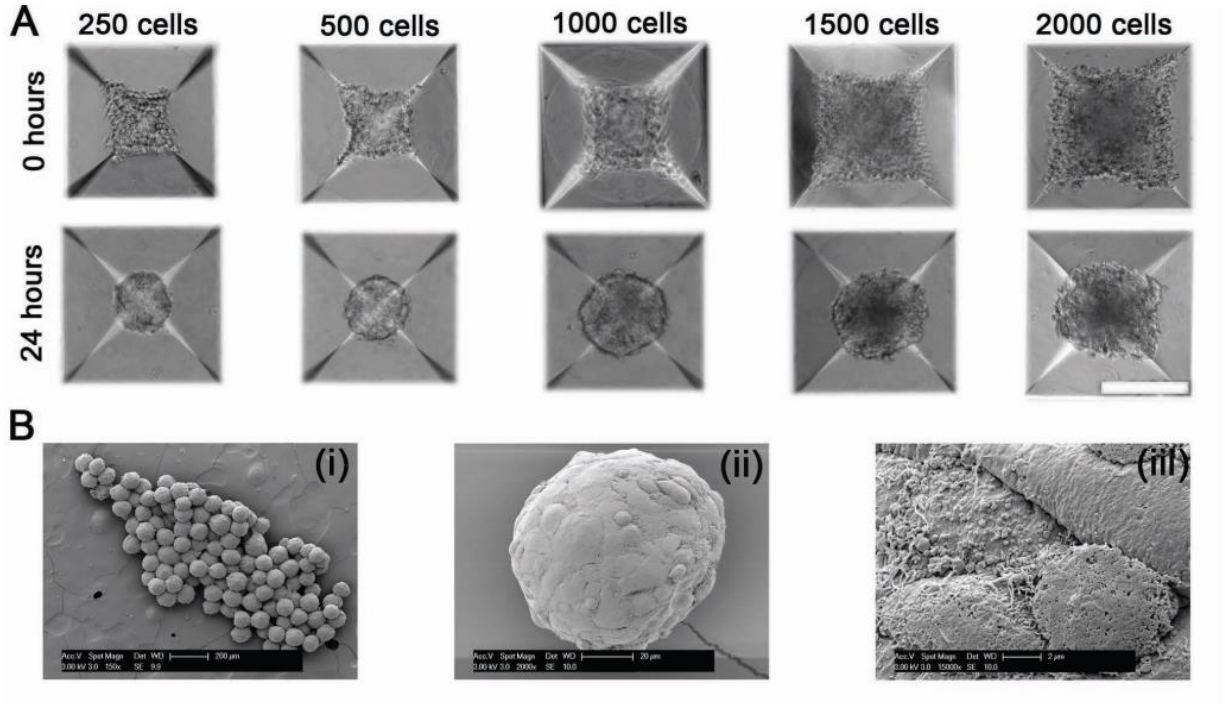

Figure 7.1: Characterization of EBs of mESCs. (A) Different densities of cells (250, 500, 1000, 1500, and 2000) seeded in AggreWell plates at 0 hours and after 24 hours (Scale bar = 200 μ m). (B) SEMs of a 1000 cell mEBs at different resolution (i) Shows the uniformity of the EBs obtained from the AggreWell plates (Scale bar = 200 μ m). (ii) An individual EB (Scale bar = 20 μ m). (iii) Close up of the EB (Scale bar = 2 μ m). *(Courtesy of: Advanced Healthcare Materials, 2013)*

Song *et al*. fabricated a continuous-flow DEP device that sorts stem cells from their differentiated products [92]. Interdigitated metal electrodes were positioned at 45 degrees to the flow

trajectory to selectively steer particles within the stream. Osteoblasts were deflected laterally and followed a zig-zag pattern due to the combination of DEP and fluid forces whereas Human mesenchymal stem cells (hMSC) remained on the original trajectory due to weak DEP forces. hMSCs were collected with a maximum efficiency and purity of 92% and 84%, respectively, while deflected osteoblasts were collected with up to a 67% efficiency and 87% purity. The partial differentiation of hMCSs may describe the heterogenous sorting achieved by this device.

Molecular DEP

As discussed in the theory section, as particles decrease in size, sufficiently larger electric field gradients are required for DEP manipulation and immobilization, which can be achieved through increasing applied voltage and reducing device dimensions. Laux *et al*. fabricated a system for trapping the enzyme horseradish peroxidase using a standard, 0.25 μm CMOS device integrated with 500 nm diameter tungsten cylinders, which were arrayed on a 2 μm pitch [93]. Optimal enzyme capture occurred at 10 kHz and 3.5 V with a threshold voltage near 1.8 V. Bubble formation due to electrolysis occurred and systems were overwhelmed with bubbling below 5 kHz, and fluid motion began to occur above 1 MHz. Enzymatic activity of trapped horseradish peroxidase was characterized by quantifying the fluorescent intensity of rhodamine 123 (Rh123). Rh123 was produced upon oxidation of dihydrorhodamine-123 by horseradish peroxidase and hydrogen peroxide. This confirmed the DEP device's ability to immobilize submicron particles with a modest enough voltage to maintain its natural functionality.

Cao *et al.* developed a iDEP platform capable of rapidly enriching proteins for a high-sensitivity immunoassay[94]. The device comprised of a structure with 5 μm inter-electrode gaps, where these gaps are filled with 100nm nanorods on a 100 nm inter-rod spacing. Iterations of the

device were made with both sawtooth and castellated electrode geometries, and both SiO_2-coated Ag nanorods and pure SiO_2 nanorods were deposited into the gaps. Bovine serum albumin protein labeled with Alexa 488 exhibited dielectrophoresis with respect to the nanorod array with positive DEP capture occurring within 10 seconds using 5 V_{pp} at 1 MHz signal. The fluorescent intensity began to plateau with increased time and negative DEP was observed at 10 MHz. The devices with SiO_2-coated Ag nanorods displayed an enrichment factor nearly ten times greater than the SiO_2 nanorods, and sawtooth electrodes slightly outperformed the castellated electrodes devices. The device constructed with both sawtooth electrodes and SiO_2-coated Ag nanorods had an average enrichment rate of 180-fold per second, the highest reported enrichment technique through 2018. Goat anti-mouse IgG antibodies were then functionalized to the nanorod surface, and mouse antigens were captured via positive DEP (1 MHz, 5 V_{pp}), with an Alexa 488-conjugated rabbit anti-mouse IgG antibody used as a fluorescent probe. The device with sawtooth electrodes and SiO_2 coated Ag nanorods achieved a limit of detection of 275.3 fg/mL.

A vast number of DEP platforms set out to sort particles or cells from heterogeneous mixtures based on bioelectric properties. Jones *et al*. developed an iDEP microfluidic device that continuously separates DNA molecules by size [95]. The device contained insulating flow chambers with an inlet and five different outlets, where one outlet lies along the centerline of the device and the other four are directed radially outward from the junction. A 20 μm constriction following the 100 μm main flow channel generated electric field gradients which imparted a DEP force of varying magnitude on the particles in stream, causing the particles to deflect within the flow stream. DNA particles of different sizes were stratified into the different outlets with high molecular weight DNA (experiencing negative DEP) following the flow lines to the central outlet. Smaller, low molecular weight DNA (undergoing positive DEP) was deflected far enough to be

diverted into the peripheral outlets. Plasmid DNA (1.0, 10.2 and 19.5 kbp) and λ-DNA (48.5 kbp) were tested using signals from 50 Hz to 20 kHz and from 100 to 2400 V_{pp}; and analyzed using time-averaged fluorescence microscopy. At 1000 V_{pp} and below 50 Hz, λ-DNA saw little deflection and flowed into the center outlet, increasing in deflection and stratification with increased frequency until 5 kHz, where sorting significantly decreased. At 2000 V_{pp}, λ-DNA was selectively deflected into the peripheral outlet, albeit very little λ-DNA deflection was observed at 200 V_{pp}. Next, each DNA analyte was individually sorted under 2000 V_{pp} and 100 Hz. 1.0 kbp DNA displayed weak sorting in the outer outlet, 10.2 kbp DNA showed strong sorting in the outer outlet, and 19.5 kbp exhibited center sorting. λ-DNA experienced pronounced center sorting across all tests. The sorting efficiency was discovered to increase linearly with applied AC voltage for all four DNA analytes. Additionally, maximum sorting efficiency occurred at lower frequencies for all four DNA lengths. Next, 10.2 kbp and 48.5 kbp DNA were simultaneously processed through the device to test size sorting, resulting in longer DNA collected in the center and smaller DNA flowing into the outer outlets. The greatest sorting efficiency was 92% for λ-DNA at 50 Hz, but AC-induced agglomeration of λ-DNA occurred at 2000 V_{pp} and 50 Hz and persisted after removal of the signal. Clusters began to form after 10-20 seconds on AC signal exposure, and were estimate to contain 10 or more molecules each.

Barik *et al.* developed a graphene-edge DEP trapping platform that is capable of reversibly trapping nanoparticles and biomolecules with nanoscale precision[96]. Back-gated graphene devices with an 8 nm thick HfO_2 dielectric were fabricated using standard nanofabrication processes. The gate dielectric was deposited using atomic layer deposition (ALD) and monolayer graphene was grown using chemical vapor deposition (CVD), then transferred onto a SiO_2 substrate using a wet transfer method. Devices were patterned such that the top and bottom metal contacts form an

interdigitated pattern. Trapping sites are defined by the width of the gate electrode which enabled capture of particles down to roughly 190 nm. The vertical gap between the two electrodes defines the magnitude of the electric field gradient. Thus, the DEP force is dependent on the thickness of both the graphene and gate dielectric layers. This sub-10 nm gap generates DEP forces that are 10X greater than forces produced by metal electrodes. The crossover frequency of 190 nm, fluorescently labeled, polystyrene beads was found to be 4 MHz. A voltage of 500 mV was measured to be the onset of polystyrene particle trapping and the maximum trapping force occurred at 750 mV, leading to 85% occupation of trapping sites. 40 nm diamond nanoparticles with nitrogen vacancy centers, which act as quantum emitters and thus allow for fluorescent detection, were trapped using a 2 V, 100 kHz signal. Additionally, the graphene device demonstrated an ability to manipulate 10 kbp and 500 bp DNA, pre-stained with YOYO-1 dye, at a 10 pM concentration. A 2 V, 100 kHz bias was used for DNA trapping with the same frequencies as the polystyrene beads for trapping. 2 V, 2.5 V, and 3 V signals produces trapping efficiencies of 32.5%, 65%, and 85%, respectively. The spatial confinement, due to the small device dimensions, enables low-concentration assays and ability to examine localized molecular interactions. Edge-trapping DEP devices can be integrated with graphene nanoresonators or tapered nanotips, which could harness both DEP trapping and mid-IR spectroscopy of low-concentration biomolecules. Additionally, quantum emitters can be positioned with nanometer resolution to build photonic circuits or single-photon source arrays.

DEP Nano/Micro Fabrication

Although a significant percent of DEP research has focused on bioparticulate manipulation, researchers have used DEP for nanofabrication and manipulation. For example, Shekhar *et al*.

developed a DEP-based technique to fabricate high density and aligned arrays of single walled carbon nanotubes (SWCNTs) on metal contacts, separated by a specified length[97]. They found their best nanotube assembly occurred between 300 kHz and 1 MHz and 5 to 10 V. This process has been optimized such that precise control of the number of SWCNTs along the metal is achieved through the concentration of the nanotube solution. A maximum density of 30 SWCNT/μm was achieved, which is the same density as found using chemical vapor deposition (CVD). However the process required a two-step growth process followed by transfer printing to produce aligned arrays. A nanotube concentration of 6.8 μg/mL was used to achieve the maximum reported density, and further increases in concentration led to multilayer nanotube films. The length of the channels which nanotubes were aligned across varied from 2 to 10 μm and the width from 100 to 1000 μm. Interestingly, the quality and density of the SWCNT alignment did not vary with length nor did the linear density of nanotubes depend on channel width when all DEP parameters were held constant.

Similar to fabricating aligned SWCNTs, Collet *et al.* developed a capillary-assisted DEP technique to assemble single nanowires on metal contacts[98]. This method focused on aligning individual nanowires precisely with the device geometry rather than on density. A nanowire solution was brought in contact with the target region and convective flow was achieved in the solution while the liquid evaporates. This resulted in an increase in nanowire concentration at the liquid-substrate interface followed by DEP trapping of a single nanowire. Finally, capillary forces held the nanowires in place as the liquid solution evaporates. An applied AC voltage of 3.2 V_{pp} and 50 kHz to a solution containing silicon nanowires ~50 nm in diameter and 5 μm long resulted in a proper nanowire alignment in 81% of specified locations. A mixed solution of silicon and indium arsenide nanowires were used to create alternating arrays of aligned nanowires by

switching the applied signals frequency from 50 kHz to 500 kHz for alignment of silicon and indium arsenide, respectively.

Seichepine *et al.* used a liquid-coupled floating-electrode DEP method to integrate 1024 carbon nanotubes (CNT) onto a complementary-metal-oxide-semiconductor (CMOS) platform without the need for a transfer step[99]. 80% of sensor locations contained one-to-five CNTs after DEP alignment, and each CNT sensor was individually addressable. Using a 10 V_{pp}, 300 kHz signal to effect positive DEP forces, CNT deposition was tracked over time using a voltage-contrast scanning electron microscope (VC-SEM). After 45 minutes, nearly 100% of electrode pairs were connected by DEP-deposited CNTs. For sufficiently long deposition times, 100% of DEP sites were filled with dense CNT assemblies. SEM images taken at 20, 30, and 40 minutes of DEP assembly indicate that CNTs are attracted to the edges of grounded electrodes.

Tang *et al*. utilized a DEP microfluidic platform to fabricate 3D Galinstan (a liquid metal made primarily from gallium, indum and tin) microstructures that enhanced the devices DEP trapping capabilities[100]. The device is comprised of a glass substrate with an array of 80 μm diameter, planar, chromium/gold circular microelectrodes. First, a liquid droplet of Galinstan is suspended in deionized water and broken into Galinstan microdroplets (2 μm average) via ultrasonic agitation, and a native oxide forms on the droplet's surface. A microfluidic device isolated the droplets out of suspension within 10 seconds by positive DEP using a 15 V, 20 MHz AC signal. A uniform distribution of droplets was achieved using a 50 μL/min flow rate, whereupon the voltage was reduced to 5 V and the flow rate was lowered to 1 μL/min. The native oxide formed on the microdroplet surfaces was then removed by flowing a 0.1 M NaOH solution, which was coupled with an increase to 10 V to promote the formation of larger droplets. Galinstan

subsequently wetted the microelectrode surface to form a hemisphere with a small contact angle. Lastly, a 1000 μL/min flow rate was used to remove unmerged microdroplets. The heights of Galinstan hemispheres ranged from 25 μm to 40 μm, as measured by curing PDMS over the microstructures. The height can be changed by varying the immobilization time with the aspect ratio increasing to approximately 1 by immobilizing for 40 seconds. This process was repeated for smaller planar electrodes, down to a minimum diameter of 20 μm. The DEP device, with its micro-structured Galinstan, displayed its ability to enhance DEP trapping of 80 nm WO_3 particles, with trapping occurring at 15 V and 1 MHz. The area of the glass slide covered by immobilized WO_3 particles was used to evaluate whether the Galinstan-improved particle trapping compared to planar electrodes alone. A better analysis would have compared particle trapping using gold hemispheres with the same aspect ratio as Galinstan hemispheres as opposed to just excluding microelectrode area. It is well documented that electric field gradients that produce DEP forces arise from micro/nanoscale features of the metal electrode or insulating structure. Therefore, it is conceivable that the 40% increase in particle trapping achieved by the Galinstan hemispheres may arise simply from its microstructure.

Cha *et al*. used DEP to cold weld 20 nm gold nanoparticles on a mica substrate[101]. This study looked at the influence of nanoparticle concentration, applied signal frequency, and electrode geometry on DEP-assisted cold-welded nanoribbons. DEP experiments were conducted over a voltage range of 1 to 10 V_{pp} and 100 Hz to 10 MHz; and the results were imaged using high resolution transmission electron microscopy (HR-TEM) and atomic force microscopy (AFM). The DEP force led to nanoparticle accumulation at the edges nanostructure while coulombic forces led to nanoparticle chaining, where the cold-welding process was initiated by forces between the particles and the mica substrate. Low nanoparticle concentration failed to begin the welding

process because of too weak of coulombic attractions whereas high nanoparticle concentrations resulted in predominantly radial growth and no elongated structures formed. AFM images confirmed coulombic aggregation of sufficient “nanoleafs”, while COMSOL analysis determined the effects from electrode geometry. Nanoribbons typically formed orthogonally to the electrodes, and specific particle formation was most easily controlled via signal frequency. The nanoribbon’s dimensions varied between 1.6-4.7 nm in height, 11-28 nm in width, and .4-1 μm in length; and the group found that electric field magnitude had little influence on agglomeration but did influence alignment.

Freer *et al.* developed a DEP-based process for high yield nanowire alignment on patterned electrodes[102]. To position single nanowires, a nanowire solution was flowed through a microchannel with electrode-patterned walls to fine tune the net force, where the latter was calculated using the sum of the positive DEP forces, hydrodynamic, and electrostatic double-layer forces. Nanowires aligned parallel to the electric field due to torque derived from their polarization and the alignment process is reversible below the point of high voltage adhesion. The flow rate and voltage was optimized to achieve consistent nanowire assembly using voltages between 320 mV and 404.5 mV for single nanowire configuration and stable, double nanowires on individual electrodes at greater than 404.5 mV. The final array contained 8 sites each with “multi-finger” electrode structures assembled with single nanowires. 98.52% of the 96 total sites were populated with single nanowires using a flow rate of 1.3 ml per min and 350 mV. The group determined a “power law exponent of ~ 2” to describe the relationship between flow rate and applied voltage, which was used to identify the ideal range for achieving single nanowire alignments. All experiments were observed using deep ultra-violet imaging techniques.

Jose *et al*. integrated a gold pyramid electrode with an XYZ micro-scanning stage to produce a mobile 3D DEP platform capable of isolating and concentrating nanostructures at the pyramid tip[103]. Their "modified template-stripping technique" used pre-patterned silicon templates to fabricate gold tips with a 20 nm diameter and sub-nm roughness. The precisely fabricated gold tip produced a highly localized electric field gradient for nanoparticle trapping at the tip's apex. Over an indium tin oxide (ITO) glass substrate, a PDMS ring was patterned to hold the solution for DEP particle manipulation. The tip was suspended 70 μm from the ITO surface as a 10 V_{pp} AC signal was applied between the ITO ground electrode and the metal tip to produce a DEP force within the liquid solution. The device showed the ability to selectively trap and repel single or multiple beads using 100 kHz and 10 MHz signals, respectively, from a water solution containing 2 μm fluorescent polystyrene beads, which were determined to have a crossover frequency of 1.67 MHz. Applying the signal for longer correlated with increased particle concentrations at the tip, improved stability of particles bound to the pyramid tip, and allowed for the capture of 190nm polystyrene beads. Fixed voltages proved more effective at trapping larger beads than smaller beads for both multiple and single trapping tests. SWCNTs were concentrated using a 10 $V_{pp,}$ 100 kHz AC signal with a 50 μm pyramid spacing, with results confirmed using Raman spectroscopy. This platform has the possibility to simultaneously use DEP trapping and probe metallic nanostructures which, along with the micromanipulation stage, may lead to developing novel scanning probe methods.

Leiterer *et al*. used a DEP micromanipulator device to attach silver nanoparticles onto heavily doped silicon AFM tips with nanoscale precision and no chemical modification[104]. 40 nm silver particles, in a $2x10^{11}$ particles/mL suspension, were tested at 7 V, from 1 kHz to 10 MHz, and it was shown that localization increased linearly with frequency using SEM and TEM imaging.

At 1 kHz, DEP was not the dominant factor and instead unreacted Ag ions in the supernatant were electrochemically growing on the AFM tip, and yielding increased growth with both time and voltage. At higher frequencies, particle loading remained relatively constant with voltage at 10 MHz, and proportional to particle density at 1 MHz, with a string-of-pearls effect showing at high concentrations. Tip-enhanced Raman spectroscopy (TERS) was demonstrated with tip prepared by DEP particle loading at 1 MHz.

Rabbani *et al*. used an iDEP microfluidic platform to investigate the DEP-trapping nature of surface-modified SWCNTs[105]. Researchers designed a device containing an array of 15 μm insulating posts with a 1.5 cm microchannel, which was used over a range of 0-1.2 kV and measured using IR fluorescence intensity. SWCNT solutions were prepared with dT30 single-stranded DNA and sodium Deoxycholate (NaDOC) and respectively underwent 5, 10, 20, 60 and 90 minutes of sonication. DEP-trapping, was only reported for the samples with DNA sonicated for 90 minutes and NaDOC at 20 and 60 minutes. DEP trapping began at 300 V and fluorescent intensity began to plateau around 600 V, indicating device saturation. Smaller SWCNTS required greater voltages to achieve DEP trapping. They swept across frequency to determine the crossover frequency and the inverse relationship between *Re*(CM) and the zeta potential of nanotubes with NaDOC.

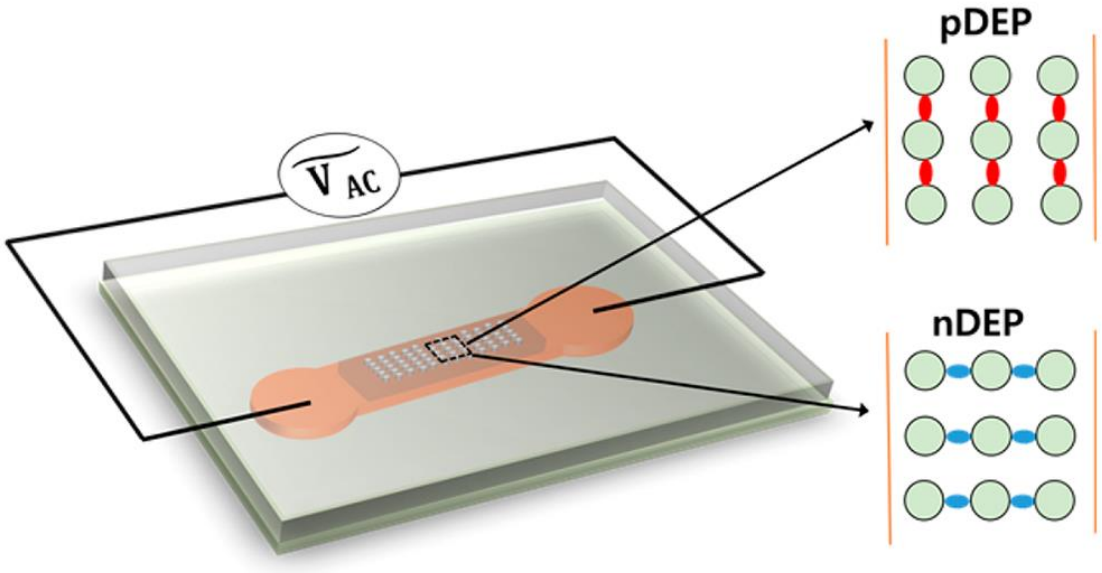

Figure 8.1: iDEP device designed by Rabbani et al. for SWCNT manipulation in an aqueous surfactant-rich microfluidic field. Expansion shows SWCNT orientation to device electrodes when activated. *(Courtesy of: Analytical Chemistry, 2017)*

Constantinou *et al.* used a 3D well electrode DEP device to selectively isolate silicon nanowires with superior electrical properties from other nanowires grown in the same solution[106]. The 3D-DEP device contains an array of wells with copper electrodes and polyimide structures that separate the electrodes and define the sides of the wells. The electrode spacing is 150 μm and the well height is 1 mm. DEP forces are analyzed by variations in the intensity of transmitted light between trapped and untrapped states in each well. Silicon nanowires were grown by the vapor-liquid-solid (VLS) mechanism using a gold catalyst and <111> silicon substrate. The nanowires were 75 nm diameter and 22 μm length. Nanowires were collected by positive DEP under an AC signal of 10 V_{pp} from 1 kHz to 20 MHz, and it was found that nanowires with preferred electrical properties were isolated between 10-20 MHz. The desired nanowires were aligned on metal contacts with a 12 V_{pp} AC signal to produce field effect transistors (FET) and between 50 and 230 nanowires bridged across the 10 μm channels of the transistor. The nanowires aligned using 10

MHz and 20 MHz signals had a 100-fold increase in current per nanowire, a 50% decreased sub-threshold swing, and approximately a 100 times greater mobility relative to nanowires collected at low frequencies.

Rozynek *et al*. developed a hybrid DEP-capillary technique to fabricate stable conductive particle chains using a macroscopic needle electrode and a liquid suspension of particles, consisting of 60 μm silver coated silica shells in silicone oil [107]. A 600 V, 20 kHz signal was applied after placing the electrode tip in the solution, and the electrode was drawn at a rate of 1 mm per second, leading to the formation of particle chains as long as 3 cm, formed in under 1 minute. Pull rates higher than the 1 μm/sec were shown to cause kinks in the chains, and results were limited to micron sized particles. Chains were deposited on surfaces by removing the AC signal. This platform successfully deposited 25 μm, 55 μm, and, 100 μm particles and developed C, S, and L patterns.

DEP Nano/Micro Fabrication/Stem Cells

Ahadian *et al*. used interdigitated platinum electrodes fabricated on a glass substrate to align graphene within poly(ethylene-glycol) (PEG) hydrogels and ultimately produce 3D stem cell scaffolds[108]. Exfoliated multi-layer graphene, at concentrations of 2.55 mg/mL and 5.1 mg/mL, were treated with bovine serum albumin and unpolymerized PEG. Treated graphene was tested for multiple electrical and mechanical properties. Horizontal alignment occurred with a 20 V_{pp} 1 MHz signal across the platinum electrodes, and an additional indium tin oxide (ITO) electrode oriented above the device served to align the graphene vertically. The suspension was then stabilized by crosslinking PEG with UV light. Each hydrogel was introduced to a serum-free media containing undifferentiated mouse stem cells, which were tested as a scaffold in a 37 °C, 50% CO_2 incubation

environment. After 5 days of monitored incubation, the horizontally aligned graphene showed an increase in percentage of viable cells whereas randomly aligned and pristine hydrogels showed minimal increases.

DISCUSSION & CONCLUSION:

In biomedical research and diagnostics, it is a challenge to isolate and identify rare cells and low copy number biomarkers in blood, plasma, and other clinical samples. In the past, DEP has been used for the separation and analysis of cells, and biomarkers such as cell-free DNA and proteins [109,110111–113 114]. Unfortunately, earlier DEP techniques were limited to operating in lower conductance solutions (< 0.1 S/m), which requires considerable dilution of many biological samples, and makes the technology impractical for sample preparation and less suitable clinical diagnostics [59,60].

More recently, newer AC electrokinetic DEP devices allow high conductance samples (0.5 to 1.5 S/m), e.g. blood, plasma and serum; to be used without dilution[62,63,115]**.** Thus, rapid isolation and direct analysis of rare cells, DNA, extracellular vesicle biomarkers and drug delivery nanoparticles can be carried out on un-diluted samples, which may help many aspects of biomedical research and clinical diagnostics [15,19,117–121,65–67,69–72,116]**.** These technological advances still have a long list of practical limitations that must be overcome before any technology can be claimed market-ready.

Ultimately, dielectrophoresis is a physical phenomenon which moves particles in a medium, and a tool for the imaginative designer to use to solve an unmet needs. In biotechnology, there is a constant need for more robust, timely automation of multiple, sequential steps, and where DEP likely has the greatest promise. With innovations in reagents, along with more precise

reaction protocols, all-in-one processes will advance DEP into the organ-on-a-chip and lab-on-chip technology spaces. Such automation and process integration requires a systems-level approach and product development mindset that has been largely unseen in the field. It is also a topic that lacks academic interest or is beyond the engineering scope of most laboratories, leaving the field in a catch-22 situation, as it also has not gained substantial commercial interest, and thus little impetus to address practical limitations.

Projects like the device designed by Menarini-Silicon Biosystems offer clever solutions to single cell manipulation, but they are limited to research tools which cannot presently offer the throughput required for clinical use. As other single-cell technologies continue to get better faster and faster each year, the DEPArray NxT will need to continue to evolve and improve. Devices like that of the Biological Dynamics group offer a truly unique ability to operate with unprocessed blood/saliva/fluid samples but have not yet brought a product to market. The automation and process integration afforded by this and other similar technologies is enabling of point-of-care device, either mobile or in a healthcare setting, or public health monitoring systems [66,84,122].

The other promising direction is towards devices that push the limits of single-molecule detection, where the sample is already prepared, and off-target contamination is minimized. Many projects reported here moving towards high-sensitivity nanostructure-based systems, showing it is a more promising topic for academic laboratories. This field of research is still in its infancy, and will inform not the next DEP devices, but the generation thereafter. The other trend coming out of exploratory efforts show continued efforts towards low-conductance cell sorting methods with their bevy of throughput and sample preparation limitations. The majority of devices, even those highlighted in this review, are still clearly preliminary and first demonstrations of technology. This

said, the future is bright, as novel work will result from cross-pollination with chemistry, material science, and engineering.

As the fundamental physics and theory approach two centuries old, it is clear that application and function of dielectrophoresis still holds a well of opportunity. The iterative process continues and as such will continue to uncover the unaddressed capabilities in DEP technologies. The demands of biotechnology will presumably lead the way forward for DEP innovation with continued advancements in nanoparticle capture and collection for disease diagnosis and monitoring. Applications in nanoparticle drug loading and drug efficacy monitoring still offer an abundance of inventive space. There are opportunities for innovating electronically controlled devices similar to that produced by Menarini-Silicon Biosystems. With a number of research predictions already having been fulfilled, there is little doubt that this integration of technologies will deliver a consistent and reliable DEP-based device that will achieve meaningful penetration in the market.

CHAPTER 2:

"Plasma Biomarker for Post-Concussive Syndrome: A Pilot Study using an Alternating Current Electro-kinetic Platform"

ABSTRACT:

Technology platforms that afford biomarker discovery in patients suffering from traumatic brain injury (TBI) remain an unmet medical need. Here, we describe a pilot study to explore the utility of an alternating current electrokinetic (ACE) microchip device in this context. Blood samples were collected from participating subjects with and without minor TBI. Plasma levels of glial fibrillary acidic protein (GFAP), Tau, ubiquitin C-terminal hydrolase L1 (UCH-L1), and cell-free DNA (cfDNA) were determined using an alternating current electrokinetic (ACE) microchip device followed by on-chip immunofluorescent analysis. Post-concussive symptoms were assessed using the Rivermead Post Concussion Symptoms Questionnaire (RPCSQ) at the one month follow-up. Highest levels of GFAP, UCH-L1, and Tau were seen in the two minor TBI subjects with abnormality on head CT. In patients without abnormal head CT, Tau and GFAP levels discriminates between plasma isolated from minor-TBI and non-TBI patients, with sensitivity and specificity of 64-72% and 50% respectively. Plasma GFAP, UCH-L1, and Tau strongly correlated with the cumulative RPCSQ score, while such correlation was not observed with cfDNA. Plasma UCH-L1 and GFAP exhibited the highest correlation to sensitivity to noise and light ($r=0.96$ and 0.91, respectively, both $p<0.001$). Plasma UCH-L1 and Tau showed highest

correlation with headache (r=0.74 and 0.78, respectively, both p<0.001), sleep disturbance (r=0.69 and 0.84, respectively, both p<0.001), and cognitive symptoms, including forgetfulness (r=0.76 and 0.74, respectively, both p<0.001), poor concentration (r=0.68 and 0.76, respectively, both p<0.001), and time required for information processing (r=0.77 and 0.81, respectively, both p<0.001). In contrast, cfDNA exhibited a strong correlation with depression (r=0.79, p<0.01) and dizziness (r=0.69, p<0.01) We provide proof-of-principle results supporting the utility of the ACE microchip for plasma biomarker analysis in patients with minor TBI.

INTRODUCTION:

Each year, over 1.7 million people in the U.S. suffer traumatic brain injury (TBI), requiring medical attention. Depending on the severity of the clinical presentation, TBI is classified into mild, moderate, or severe. 30 >80% of head trauma patients who present to the emergency room suffer from mild TBI. While the majority of these mild TBI patients are discharged from the emergency room on the same day and recover without detectable long-term sequelae, 30% of mild TBI patients will have persistent "post concussive" symptoms that significantly compromise their quality of life, including headache, fatigue, as well as altered sensation, sleep, and attention span. Notably, ~8% of mild TBI patients demonstrate visible injury to the cerebrum on computerized tomography (CT). Direct and indirect costs associated medical care and productivity loss associated with mild TBI exceeds $60 billion annually. Mild TBI involves complex pathophysiologic processes associated with microscopic shearing of cells in the central nervous system secondary to traumatic biomechanical forces to the head. Such shearing induce damage to the cell, resulting in the release of neuronal and astrocytic proteins or cell-free DNA (cfDNA) not normally found in the extracellular space, including glial fibrillary acidic protein (GFAP), 5 ubiquitin carboxyl-terminal hydrolase L1 (UCH-L1), and Tau. Tau is a microtubule stabilizing

protein abundant in neurons, and released into the extracellular space upon neuronal damage. GFAP is an intermediate filament protein highly abundant in astrocytes, and increased levels in blood or CSF are linked to axonal injury. UCH-L1 is a neuronal protease, with increased levels linked to brain injury. Since ~20% of circulating blood volume perfuses the cerebrum and TBI often compromises the blood-brain barrier, these released proteins can be detected in peripheral blood drawn from TBI patients. The high sensitivity and specificity of GFAP and UCH-L1 as proxy for abnormal CT following TBI have paved way to clearance by the U.S. Food and Drug Administration (FDA) for their use in TBI work-up. In contrast to the number of tools that afford study and characterization of TBI associated structural injuries, there are currently no clinical criteria or biomarkers that afford identification of the minority of mild TBI patients who suffer long-term sequelae despite absence of detectable structural damage to the cerebrum. Currently, study of these symptoms relies on questionnaires, such as the Rivermead Post Concussion Symptoms Questionnaire (RPCSQ), that are administered at regular intervals after the injury. Development of predictive tools for likelihood of post-concussive symptom can meaningfully impact the care of mild TBI patients and advance our understanding of the underlying pathophysiology. Here, we explore the utility of plasma GFAP, UCH-L1, Tau and cell-free DNA in this context using an alternating current electro kinetic (ACE) microchip device. ACE microarray chips use alternating current to isolate macro-molecular complexes from bio-fluids, such as blood or cerebrospinal fluid, in a highly efficient manner. Of note, nearly all plasma GFAP, Tau, and UCH-L1 are found in these macro-molecular complexes. The chip-retained protein can be labeled with fluorescent antibodies or dyes specific for the biomarker of interest. Quantitative on-chip fluorescent imaging analysis is then carried out (Figure 1A). In this pilot study, we correlated the levels of ACE isolated GFAP, UCH-L1, Tau and cell-free DNA from blood drawn

at the time of injury to Rivermead questionnaire results collected at one month after head injury from mild TBI patients.

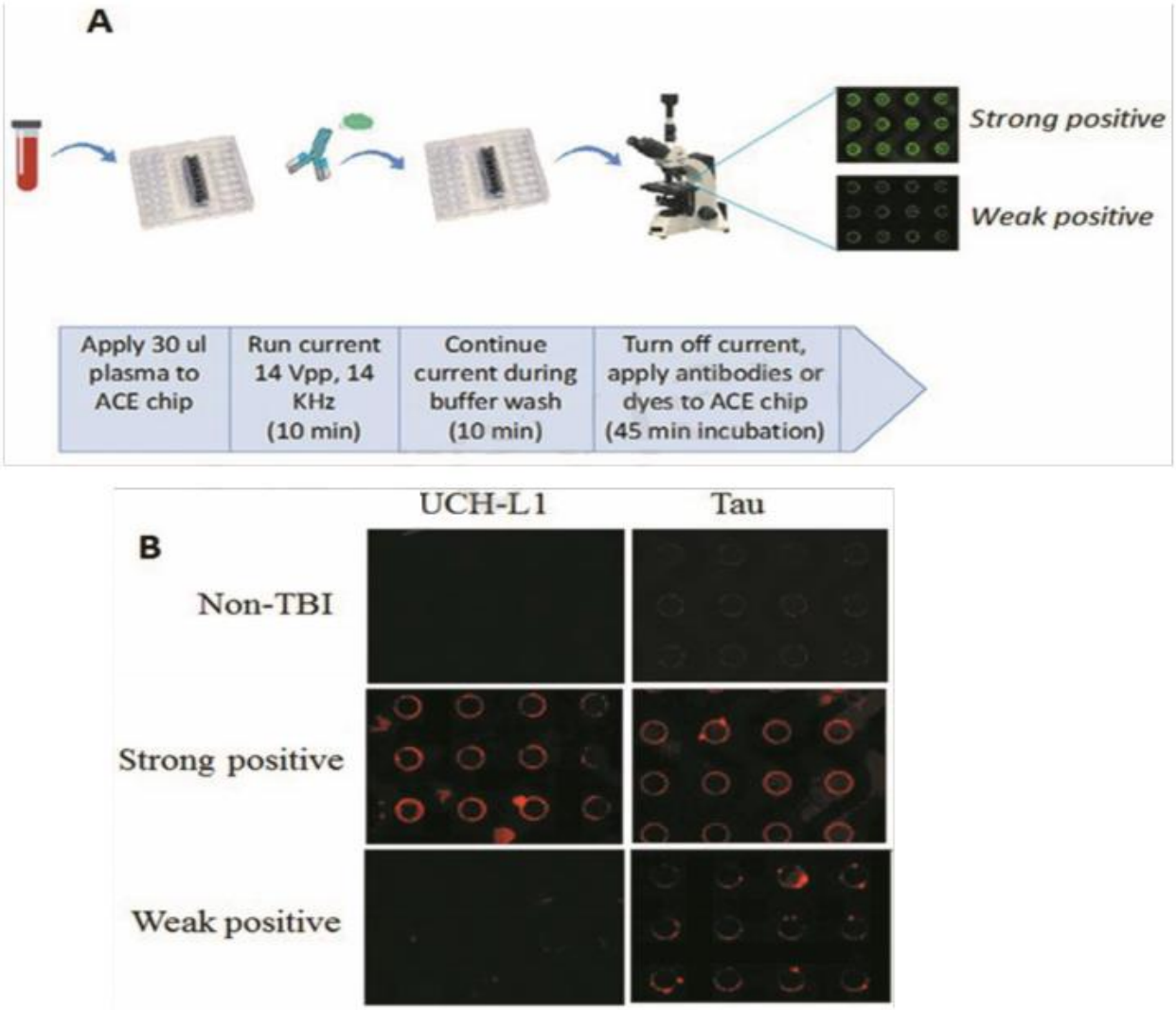

Figure 9.1: A) Overview of ACE microchip immunoassay workflow. Shown is a fluidics cartridge containing the 14 x 52 mm-sized ACE chip configured with 8 sample chambers. When current is applied, extracellular vesicles (EVs) and other nanoparticles are drawn to the edges of the circular electrodes; the buffer wash serves to remove larger unbound cellular debris and smaller soluble plasma components from the chip. The current is then turned off, mixtures of fluorescent antibodies or dyes selective for each biomarker are added, and the concentration of biomarker proteins around the electrodes can be visualized as circular patterns of fluorescence. Image analysis provides a quantitative comparison of fluorescence intensities. B) Representative examples showing relative abundance of UCH-L1 and Tau using the ACE microarray and on-chip immune-fluorescence (IF) analysis. ACE: alternating current electrokinetic. UCH-L1: ubiquitin C-terminal hydrolase L1

RESULTS

Demographics and clinical course of the study cohort

The study enrolled 27 minor TBI subjects and 6 non-TBI subjects between December of 2015 and March of 2016. The demographic of the study population were divided into two groups, 10 females and 17 males with minor TBI conditions, and 3 male and 3 female, non-TBI exhibiting patients. The mean age of the minor-TBI and non-TBI cohort was 58.5±16.4 years and 34.6±10.6 years, respectively. The male to female ratio were approximately 1:1 in both cohorts. All patients in the minor-TBI cohort underwent head CT as a part of their care. Except for the two patients (2/27 or 7%) who showed evidence of contusion on head CT (Figure 2A), all patients had negative head CTs and were discharged from the Emergency Ward on the day of the presentation. The two patients with abnormal head CT were admitted to the hospital for over-night observation. Both underwent interval surveillance imaging demonstrating stability of CT finding before discharge on the following day. The non-TBI patients presented with chest or abdominal discomfort. Diagnostic work-up were unremarkable and the patients were discharged on the day of intervention. Biomarker comparison between subjects with and without abnormal head CT Plasma samples from the study cohort were analyzed for the relative abundance of GFAP, Tau, UCH-L1, and cfDNA using the ACE microarray and on-chip immunofluorescence (IF) analysis. Representative examples of these analyses are shown in Figure 1B. Relative immunofluorescence (rIF) level was determined for each sample. We first posed the question of whether any of the biomarkers were elevated in the two minor-TBI patients with abnormal head CT (subject 5 and subject 8) relative to all remaining patients. We performed this analysis in a qualitative manner since the sample size is too small for meaningful quantitative assessment. Consistent with the published utility of GFAP and UCH-L1,8 plasma from subject 8 showed significantly elevated

levels of both proteins. In fact, this subject harbored the highest level of both GFAP and UCH-L1 for all study cohorts. Plasma from subject 5 also showed significantly elevated UCH-L1 (Figure 2B). Notably, plasma from both subjects 5 and 8 also harbored significantly elevated Tau levels. These observations suggest the utility of plasma Tau as biomarker for structural brain injury after TBI. In contrast, the plasma level of cfDNA in subjects 5 and 8 were not significantly elevated relative to other study cohorts.

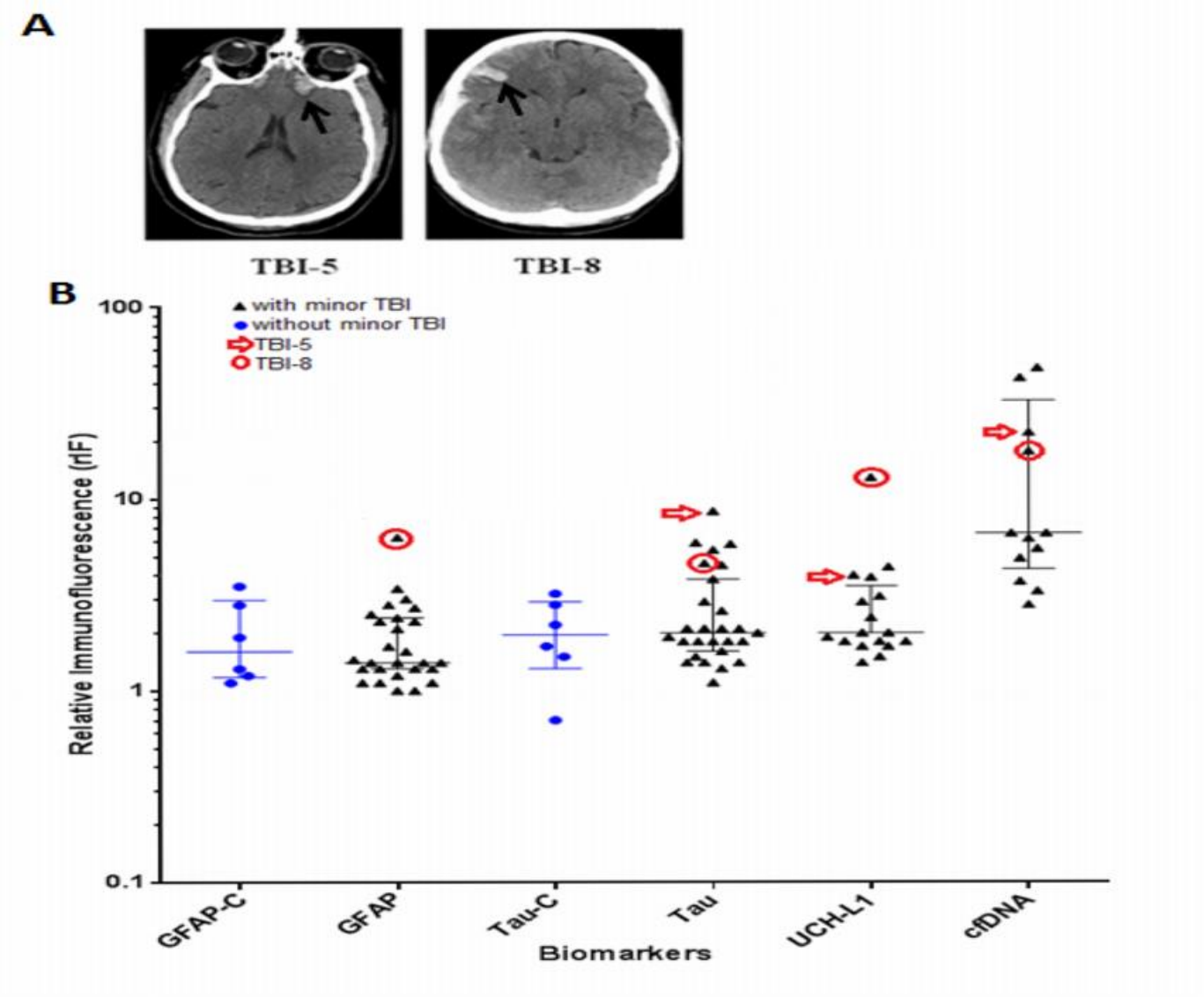

Figure 10.1: A) CT scan images showing contusion in patient #5 and #8 with minor traumatic brain injury (TBI) (black arrow). B) Scattered dot plots illustrating distribution of relative immunofluorescence (rIF) (median with inter-quartile range) values for GFAP, Tau, UCH-L1 and cfDNA in TBI cohort, and GFAP and Tau in non-TBI cohort (represented as GFAP-C and Tau-C, respectively). Blue dots represent the rIF values for Tau and GFAP in patients with no history of head trauma. Black triangles represent the rIF values for Tau, GFAP, UCH-L1 and cfDNA in patients with history of head trauma. rIF values for patient #5 are denoted by red arrow; rIF values for patient #8 are encircled in red. GFAP: glial fibrillary acidic protein; UCH-L1: ubiquitin Cterminal hydrolase L1; cfDNA: cell-free DNA.

In aggregate, these results validate the association between elevated plasma GFAP, UCH-L1, and structural TBI demonstrated on head CT. The results further suggest the utility of plasma

Tau protein in this context. Biomarker comparison between mild-TBI and non-TBI subjects We wished to determine whether any of the biomarkers studied can discriminate the plasma collected from minor-TBI patients relative to non-TBI patients without abnormal head CT. Because of the limited volume of samples collected, we were only able to complete this analysis for plasma GFAP and Tau. We additionally excluded subjects 5 and 8 from this analysis since we were interested to characterize the value of these biomarkers in head CT negative TBI patients. Receiver operator characteristic curve were calculated to determine the area under the curve (ROC-AUC) for GFAP and Tau. Based on the ROC-AUC, the optimal rIF values for discriminating minor-TBI plasma from non-TBI plasma was 1.75 for Tau and 1.35 for GFAP. Using these cut-offs, the sensitivity and specificity of discriminating plasma between minor TBI and non-TBI patients. In this analysis, Tau and GFAP performed similarly, with sensitivity of 72% and 64%, respectively, and specificity of 50% for both proteins. The combinations of GFAP and Tau did not significantly improve the sensitivity or specificity relative to the individual biomarker.

Table 1.1: A) Correlation between different biomarkers and cumulative Rivermead symptom scores; ǂ: p≤0.01 (B) Heat-map demonstrating the correlation between different biomarkers. Pearson correlation coefficient, r is mentioned in each box.

A

	Rivermead Cumulative Scores		
Biomarker	r	R^2 (adjusted)	*P* value
GFAP	0.68	0.18	0.01ǂ
Tau	0.81	0.63	< 0.001ǂ
UCHL1	0.79	0.59	< 0.001ǂ
cfDNA	0.07	-0.08	0.81

B

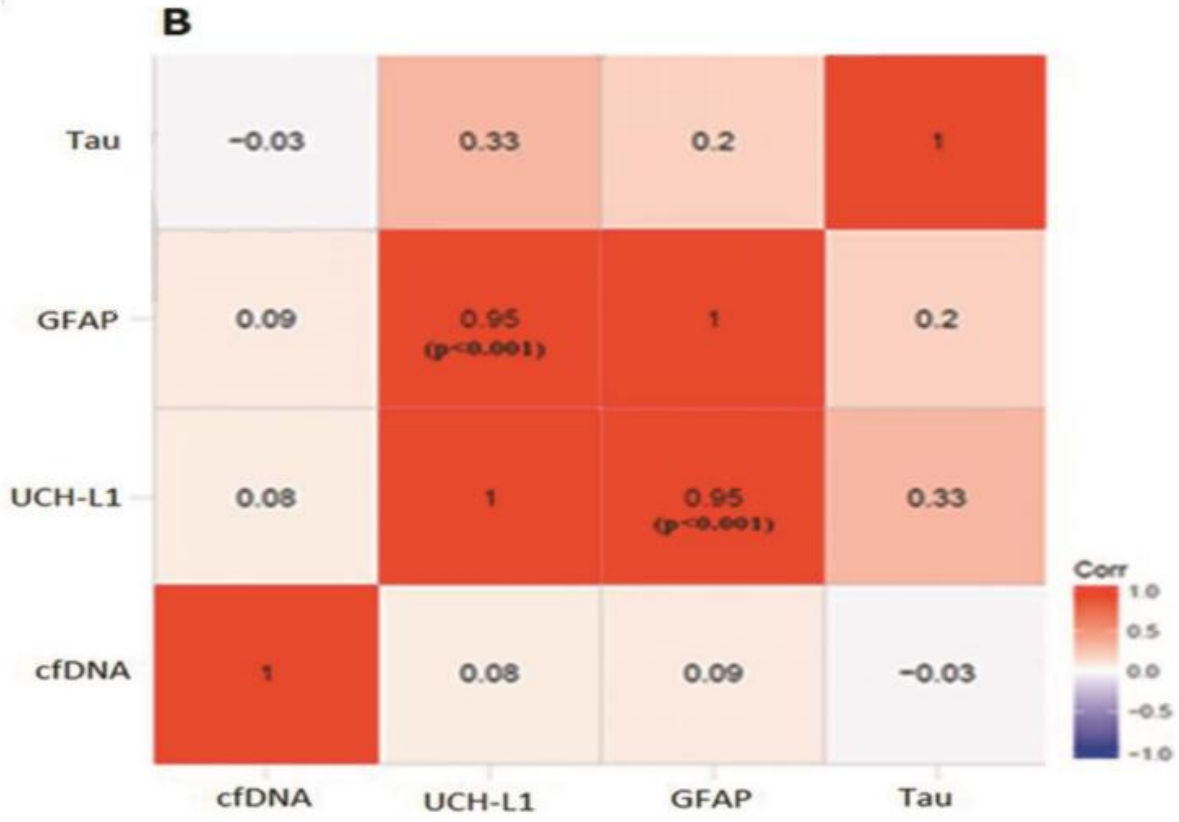

Biomarker comparison between subjects with and without post-concussive symptoms We next determined whether the presence of post-concussive symptoms is associated with elevated plasma GFPA, UCH-L1, Tau, or cfDNA. To this end, the Rivermead Post Concussion Symptoms

Questionnaire (RPCSQ), a validated instrument for assessment of post-concussive symptoms following mild TBI,16,17 was administered to study subjects by a trained study coordinator at one-month follow-up. RPCSQ score was obtained for all 27 minor-TBI subjects. The highest cumulative RPCSQ scores were observed in the two patients with CT imaging abnormalities. No significant correlation was observed between the cumulative RPCSQ and cfDNA. However, we observed significant, positive correlation between plasma GFAP, UCH-L1, and Tau and cumulative RPCSQ (Figure 3A). Specifically, the higher RPCSQ scores were associated with higher plasma biomarkers. The Pearson correlation between GFAP, UCH-L1, and Tau and cumulative RPCSQ were 0.68, 0.79, and 0.81, respectively (all $p < 0.01$). In a correlation matrix analysis, we found that plasma GFAP and UCH-L1 levels were highly correlated ($r= 0.95$, $p<0.001$) (Figure 3B). These results suggest plasma GFAP, UCH-L1 and Tau may be useful as predictive biomarker of post-concussive syndrome. Pertaining to each of the individual items on the RPCSQ, Plasma UCH-L1 and GFAP exhibited the highest correlation to sensitivity to noise and light ($r=0.96$ and 0.91, respectively, both $p<0.001$). Plasma UCH-L1 and Tau showed highest correlation with headache ($r=0.74$ and 0.78, respectively, both $p<0.001$), sleep disturbance ($r=0.69$ and 0.84, respectively, both $p<0.001$), and cognitive symptoms, including forgetfulness ($r=0.76$ and 0.74, respectively, both $p<0.001$), poor concentration ($r=0.68$ and 0.76, respectively, both $p<0.001$), and time required for information processing ($r=0.77$ and 0.81, respectively, both $p<0.001$). In contrast, cfDNA exhibited a strong correlation with depression ($r=0.79$, $p<0.01$) and dizziness ($r=0.69$, $p<0.01$).

Table 2.1: Correlation between different traumatic brain injury (TBI) biomarkers and Rivermead Questionnaire symptoms. Statistically significant ($p<0.05$) Pearson co-efficient (r) is mentioned in bold format in box. - represents symptoms that were not recorded in minor TBI patients.

Biomarker / Symptom	UCH-L1	Tau	GFAP	cfDNA
Headache	**0.74**	**0.78**	**0.65**	-0.05
Nausea/Vomiting	0.15	**0.69**	0.14	0.32
Dizziness	-0.23	-0.43	-0.22	**0.69**
Noise sensitivity	**0.96**	0.12	**0.91**	0
Light sensitivity	**0.96**	0.12	**0.91**	0
Blurred vision	-	-	-	-
Double vision	-	-	-	-
Sleep disturbance	**0.69**	**0.84**	0.53	-0.05
Fatigue	**0.62**	**0.70**	0.41	-0.03
Irritable	**0.57**	**0.88**	0.48	-0.09
Depressed	0.45	0.21	0.35	**0.79**
Frustration	-	-	-	-
Restlessness	**0.77**	**0.82**	**0.68**	0.02
Forgetful	**0.76**	**0.74**	**0.69**	-0.11
Time for information processing	**0.77**	**0.81**	**0.63**	-0.01
Poor concentration	**0.68**	**0.76**	0.57	-0.13

METHODS

Study Design Research protocol (IRB #120345X) was approved by the University of California San Diego Institutional Review Board. Study subjects were patients who sought care at the Hillcrest UC San Diego Medical Hospital Emergency Department. Each patient underwent blood draw as per standard-of-care. Informed consent was obtained from each participating patient by a dedicated research assistant on the day of presentation. Competency of consent were

determined by the University of California San Diego Brief Instrument for Assessing Decisional Capacity for Clinical Research (UBACC) 10 item scale administered by the trained clinical coordinator. Competency for consent was further confirmed by the attending Emergency Room faculty physician. Blood samples that remain after standard laboratory chemistry were collected, and no blood draw beyond the standard-of-care venipuncture was performed. The residual blood was collected from the chemistry lab the day after the presentation after adequate laboratory values were reported to the Electronic Medical Record. Hemolyzed samples were not collected. The volume of the residual blood ranged from 100 μl to 1.5 ml. Samples were collected from consecutive patients who presented with minor TBI, defined by Glasgow Coma Scale (GCS) of > 13.32 In parallel, patients who presented with non-TBI and non-neurologic complaints were identified from the Emergency Ward dashboard.

Patients who required major medical intervention, such as cardiac catheterization or surgical intervention were excluded from the study to minimize risk of adding stress of study participation to the patient. Residual blood after completion of standard chemistry was collected from these patients in the same manner as described above. Samples were transported to the UCSD Biorepository where they were de-identified and stored as processed plasma by centrifugation at 1300 rpm for 10 minutes followed by 3000 rpm for 10 minutes. Samples were stored at -80 C before analysis. Procedures for de-identification and human subject protection were performed in compliance to UCSD HRPP policy. For all study subjects, participation in this study did not alter the standard of care, including the routine one-month post-presentation follow-up for patients with minor TBI. For the patients who presented with minor TBI, they underwent standard-of-care work-up as determined by the attending Emergency Ward faculty physician, including non-contrast computed tomography (CT) scan of the head. The only exception to the above is that the

Rivermead Post Concussion Symptoms Questionnaire (RPCSQ)16,17 was administered by a trained study coordinator at this one month follow-up. ACE-based processing of plasma samples ACE chips were purchased from Biological Dynamics, Inc. (San Diego, CA). A syringe pump set to withdrawal mode served to regulate fluid flow across the ACE chip. Tygon tubing (inner diameter, 0.020 inches; outer diameter, 0.060 inches) was attached with superglue to either end of the chip, both ends were capped with syringe needles, and a 1 ml syringe was attached to one end. Twenty-five μl of thawed plasma was drawn onto the chip. An alternating current (AC) electric field was applied to the chip for 10 minutes at 14 volts peak-to-peak and 15 kHz to immobilize extracellular vesicles and other nanoparticles onto the microelectrode edges. With the AC field still on, the ACE chip was then washed with 200 μl of 0.5X PBS for an additional 10 minutes. The time taken for the entire process was 20 min for the ACE-based isolation, plus an additional 45-90 minutes for antibody binding steps (Figure 1A). On-chip immunofluorescent analysis Two biomarkers were tested simultaneously on each chip, using FITC and TRITC filter sets on the microscope. To enable access of the antibodies to proteins within the luminal space of the vesicles, EV membranes were permeabilized using 0.1% saponin for 10 minutes. To label cfDNA, the selective dye YOYO-1 was added to a concentration of 1:5000. Antibody incubations were for 45-90 minutes at room temperature, or, if recommended by the manufacturer, overnight at 4 oC for optimal binding. For directly conjugated Alexa Fluor 488-anti GFAP antibody (BD Pharmingen), samples were washed with PBS, then visualized and photographed for further analysis. For anti-Tau or anti-UCH-L1 (Life Technologies; Cell Signaling Technology), following the wash, Alexa Fluor 594-conjugated secondary antibody (Novex, Life Technologies) was incubated for an additional 60 minutes at room temperature. Following an additional wash, samples were viewed on the microarray chips using an Olympus BX51W epifluorescence microscope with a 4X

objective and imaged with Olympus software. All image acquisition parameters were the same for the same fluorophore.

To quantify relative levels of fluorescent antibody-labeled Tau, GFAP, UCH-L1, and cfDNA for each sample, photographic images of each ACE-chip were imported to ImageJ ("FIJI"; National Institutes of Health). A circle was drawn around each of eight electrodes, and pixels measured. Background subtracted was the minimum number of pixels measured for each electrode, and averages and standard deviations were calculated. Direct 3D representations of the images were created using the "3D interactive viewer" plug-in for ImageJ.

Statistical Analysis

Models were used to predict the severity of injury with the probability of intracranial abnormality post TBI. The probability threshold was chosen as that which minimizes the Euclidean distance from point (0,1), or the upper-left corner, on the receiver operating characteristic (ROC) curve. ROC curve were calculated to determine the area under the curve (ROC-AUC) for different biomarkers. Based on the ROC-AUC, the optimal rIF values for discriminating minor-TBI plasma from non-TBI plasma were calculated for different biomarkers. Model predictions were compared to observed diagnoses and performance metrics were calculated, including sensitivity, specificity, positive predictive value (PPV), negative predictive value (NPV), and the area under the ROC curve (AUC). Heat maps were constructed and Pearson correlation coefficients were calculated between GFAP, UCH-L1, Tau, cfDNA, and cumulative RPCSQ score. Correlation analysis between GFAP, UCH-L1, Tau, cfDNA, and individual RPCSQ symptoms was also performed. All analyses were carried out using open-source statistical analysis software (R version 3.5.0).

DISCUSSION

In this proof-of-principle study, we determined whether plasma isolated from minor TBI patients can be analyzed using an ACE-microarray platform. 12 Because this platform had not been previously tested in this context, we selected TBI biomarkers with substantial literature supporting their utility in the study of TBI, including GFAP, UCH-L1, and Tau. We additionally tested whether cfDNA may serve as a useful biomarker. Our pilot data with the ACE-microarray platform support the utility of GFAP, UCH-L1, and Tau as plasma biomarker for TBI. Despite inherent constraints associated with the limited sample size, our pilot data are largely consistent with the previously published studies, including TRACK-TBI studies. 8,10 As such, we believe our data support ACE-microarray as a platform for blood-based biomarker study in patients suffering from minor TBI.

In comparison to the currently available methods of plasma analysis, the ACE micro-array platform presents several major advantages. First, ~25 μl of plasma is required, in comparison to other analytic platforms that require larger volumes. It is important to note that the entirety of this study was performed using blood left-over from standard chemistry tests. As such, if validated, the ACE micro-array platform may be added to the standard chemistry set without additional blood collection. Additionally, the ACE-microarray platform minimizes the number of steps in terms of sample transfer, and thereby reduces the risk for cross-contamination or sample mix-up. The only sample transfer step in the ACE-microarray platform was loading of the plasma onto the chip. In contrast, serial dilution of samples is typically required for sandwich enzyme-linked immunosorbent assays (ELISA). Finally, the chip can be subjected to multiplex immuno-fluorescent study to simultaneously assess biomarkers beyond Tau, GFAP, and UCH-L1. A particularly intriguing result in this study involves the correlation between sub-domains of the

RPCSQ and selected plasma biomarkers. Our results indicate that plasma UCH-L1, GFAP, Tau, and cfDNA levels correlated with different symptoms in the physical RPCSQ cluster domain. If validated, these results would suggest that the different aspects of post- concussive syndrome arise from pathophysiologic processes that ultimately lead to the release of the distinct biomarkers. A corollary of this hypothesis would suggest that medication that mitigates select patho-physiologic processes may be helpful to prevent or arrest post-concussive symptoms that compromise the patient's quality of life. While this proof-of-principle study is, by definition, limited in its sample size and pilot in nature, the general demographic of the study population largely mirrors those of larger series, including the demographic of the study population, the proportion of minor TBI patients with abnormal head CT,18 and the recapitulation of the association of GFAP, UCH-L1, and Tau with various aspects of TBI.3

In this context, we believe that future prospective studies aimed to validate the utility of the ACE-microarray platform for TBI biomarker development is warranted. Our proof-of-principle study provides pilot data supporting the utility of the ACE microarray platform for plasma biomarker analysis in TBI patients.

CHAPTER 3:

"On-chip Isolation and Mulit-Omic Analysis of Peripheral Blood Nanoparticulae"

ABSTRACT:

Early detection and precision oncology lead the medical research community into the new decade with opportunities to expose and treat diseases with less invasive, less toxic and more effective therapies to prevent disease progression. Extracellular vesicles (EVs) including exosomes, nucleosomes and other cell-derived nanoparticles carry an invaluable payload of disease related biomarkers. Information from such entities offers researchers a methodology for disease detection, diagnosis and treatment. Technical challenges in the efficient isolation and collection of EVs, exosomes and other nanoparticles has limited our ability to leverage important information contained within these nanovesicles. Here we have demonstrated the use of an electrokinetic microarray for the isolation, identification, collection and analysis of EV-associated biomarkers in whole blood samples from Chronic Lymphocytic Leukemia (CLL) patients. Such biomarkers include proteins, RNA and DNA. Cell-derived nanoparticles were isolated from peripheral blood samples, imaged and collected for both on-chip and downstream analyses in approximately two hours, confirm ROR1 biomarker upregulation. Use of an electrokinetic microarray device offers a versatile, sensitive and efficient assay with potential applications in point-of-care or early detection/diagnosis as well as complex personalized therapeutic design and monitoring.

INTRODUCTION:

Healthcare research continues to develop more advanced, more intricate disease therapies within precision oncology that are improving the chances for positive patients' outcomes [123,124]. Simultaneously, new detection and diagnostic technologies along-side improvements in monitoring are allowing doctors to carefully define disease condition, patient progress and therapeutic efficacy in real time[125,126]. Where standard approaches of chemotherapy, radiation and other cancer treatments take an aggressive line in bombarding the tumor with toxic drug cocktails, precision oncology harnesses the power of detailed information to develop a treatment approach with pin-point accuracy instead [127]. With so many differences in stages of disease and phases of the detection, diagnosis, therapy and monitoring, the sources of critical information are immense [128]. These unique sources can evolve with the progression of treatment or disease state as well. Defining a methodology and a technique that allows true standardization for doctors to interrogate biomarkers at all different phases is necessary to trust and understand subtle differences that offer significant contributions to treatment decisions. The ultimate goal is to develop an approach that unifies these powerful sequential steps, under one versatile and dependable technology.

Methods for information collection and analysis historically relied on single-nucleotide polymorphism mapping and comparative analysis. As technologies advance and expand for genomic profiling, biomarker detection, epigenomic profiling and transcriptomic activity to focus more on mutation identification and classification. Nucleic acid sequencing technologies have improved the clarity of expression profiles and have enhanced detection capabilities of low copy numbers for early diagnosis and prognostication [129]. Epigenomics has recently become a niche of particular research focus with in-depth study of histone modification, transcription factor occupancy and DNA methylation patterning[130].

Extracellular vesicles (EVs) including exosomes, nucleosomes and other nanoparticles may offer a viable and direct avenue for obtaining this valuable information. Extracellular vesicles can be found in blood, plasma, serum, urine as well as host fluids as well as in growth media from bacteria and other single celled organisms. Healthy and unhealthy cells produce EVs; however, many disease conditions exhibit a significant release of these EVs into circulation as a result of change or disruption to cellular metabolism, cell damage or cell stress. These EVs exhibit characteristics uniquely representative of their cells of origin and can contain cargo ranging from but not limited to, mRNA, miRNA, vRNA, rRNA, DNA, protein and enzymes [131,132]. Blood has rich concentrations of highly active RNases and DNases that quickly destroy most cell free nucleic acids that get released into circulation. Extracellular vesicles encapsulate and protect these labile particles in a highly stable lipid-bilayer, keeping them viable for capture, concentration stabilization and analysis [133]. Extracellular vesicles cover a vast range of particles produced by many different organisms and cell types. A with significant number in range from 50-200 nanometers in diameter are often referred to as exosomes [134]. The metabolism and the nature of the cell of origin significantly influence the physical nature and quantity of EVs. Certain cancer conditions for example will produce extremely high concentrations of smaller EV's while others will generate at more normative rates and sizes despite specific disease pathology [135]. EVs have been determined to serve a multitude of functionalities from necrotic waste disposal to cell-to-cell communication, still the range of purposes and mechanisms by which the bioparticulate payload is encapsulated and functionalized is still largely unexplained [136,137].

Accessing the potentially invaluable content encapsulated within EVs poses some difficult challenges. The nanoscale size and the relatively low buoyant density make most traditional nanoparticle isolation protocols ineffective[138]. Nanoscale filtration is also made difficult by EVs

nature to clump together and stick to vials, pipettes and filter bodies. The lipid bilayer outer membrane also limits the use of surfactants to ease flow processes. The current gold standard for EV isolation and concentration involves many hours of labor intensive, multi-step filtration and ultracentrifugation. These different approaches and processes take anywhere from 12-15 hours up to 24-hour overnight spin protocols depending on the sample and experimental specifics [139–141]. Immunoaffinity capture techniques are problematic for applications of detection and diagnosis as they only capture a sub-population of exosomes. Recent developments of nanoplasmonic devices even demand up to 60 hour protocols for the isolation of exosomes from buffer solutions [139]. A number of new technologies have emerged that are making fast progress towards a rapid isolation platform using electrokinetic microarrays to process materials or particles of interested out of various patient samples. These devices use a combination of microfluidic and electrokinetic forces to isolate nanoparticles and microparticles from any range of human sample types. Many of the systems rely on immunofluorescent antibodies for selective capture, identification, imaging and analysis [142–144]. Other developing methods of detection include measurement of mechanical forces of flow on EV/particle-tethered nanobeads, electrochemical sensors, nanopore extrusion and surface plasmon resonance. Processing samples on most of these platforms requires a filtration step prior to device application which can further alter the results collected from experimentation. Many of these devices face challenges of damaging sheer stresses, clogging, inhibitive flow rates and throughput limitations which are primarily attenuated by specific device architectures. However, these reconciliatory design elements are often sample specific and limit device versatility and application potential. Some recent developments have presented the use of magnetic beads coupled with tagged lipids to bind to EVs outer bilayer for electromagnetic isolation [70]. Unfortunately, sub-50% isolation efficiencies for EV's in human plasma suggest interference due

to highly active binding elements found in unprocessed samples, limit the practical potential for this technology [145]. This approach will also need to consider different lipid associations and compositions for a wide range of target EV populations which will likely exhibit significant difference between disease conditions. None of these aforementioned technologies have the capacity to receive and process whole blood directly as many require multiple steps of sample preparation and dilution and decisively fall short of the demands placed on a device used for clinical applications[70,146].

The developments of a novel alternating current electrokinetic (ACE) microarray device from Biological Dynamics, a laboratory in San Diego, California, has produced a string of successful methods and protocols for the isolation and concentration of EV's and nucleic acids from various sample types [67–69]. This same device has shown a wide range of applications and sample compatibilities. Our research group has successfully isolated and collected high molecular weight DNA, bacteria and bacteriophage from undiluted plasma samples and whole blood [65,66,119,121]. Most recently, Lewis *et al.* used the Biological Dynamics dielectrophoretic (DEP) platform to conduct a principle analysis of glioblastoma diagnostic exosome/extracellular vesicle based biomarkers [72]. These results show impactful progress and clear evidence that this DEP microarray device might offer enough versatility to perform a comprehensive complete omic or "multiomic"analysis of a single patient sample, all in one sequential protocol.

RESULTS:

In this study, we present results demonstrating isolation, identification and collection of RNA, DNA, extracellular vesicles and protein biomarkers all carried out on a single ACE microarray chip from a single Chronic Lymphocytic Leukemia human whole blood sample. Using

this protocol, RNA DNA and A ROR-1 transmembrane protein biomarker was identified in 2 hours, and subsequent elution, stabilization, and amplification allowed for RNA and DNA PCR protocols to confirm genetic markers. This assay proves to be versatile, quantitative, sensitive and efficient. In this work we challenged the limit of information that this device can be extracted from a 50 μL ample of whole blood. Immunofluorescent-based quantitative analysis performed on labeled ROR-1 protein biomarkers from the complete sample cohort (n=15) enabled cross comparison to healthy individuals and FACS data collected as a gold standard control. Immunofluorescent data was consistent with results from FACS analysis on same patient samples, as well antibody assay correctly identified relative highs, lows and healthy control samples.

Design and Optimization of Immunofluorescent Assay:

In this work, the developing ACE microarray device from Biological Dynamics (San Diego, CA), was used to capture and isolate EV's from 6 CLL patient whole blood samples, and 12 CLL patient plasma samples. The platform consists of a single ~25 μL primary flow channel that serves as the sole reaction chamber for patient sample interrogation. The microfluidic flow channel passes over 1000 platinum electrodes arranged on a metal-oxide-semiconductor microchip. An inlet and outlet tube allow for sample introduction and microfluidic sample control via the outlet syringe/syringe-puller connection. This work is the first evidence of a technology capable of isolating and protecting for downstream analysis, the complete range of multiomic bioparticulates from a single 50μL peripheral blood sample. The particle manipulation follows a seven-step protocol; 1) Sample introduction 2) Target material capture 3) Wash/isolation 4) Stain 5) Image 6) Elute 7) Downstream analytics. Altogether, the complete protocol required 2 hours from sample receipt to biomarker confirmation and target collection ready for analysis and processing.

As mentioned, 6 CLL whole blood samples and 12 CLL patient plasma samples were processed through the device and genetic and biomarker material were successfully isolated, imaged and stabilized for more in-depth analysis. Following a seven-step protocol, patient whole blood sample was introduced to the microelectrode array, and extracellular vesicles, exosomes and other nanoparticles were isolated and captured in the high field region of the chip. After a 10-minute PBS wash, on-chip fluorescent detection of RNA particles was confirmed with CYTO RNASelect stain. Another fluidic wash allowed for imaging of the target RNA. Figure 6 shows fluorescent images taken of the RNA protected and encapsulated in the EV's and exosomes for patients MJH-CLL-13, MJH-CLL-15, and MJH-CLL-18. 3D surface plots (right) illustrate a clear representation of the relative fluorescent intensity for comparison to the raw fluorescent capture (left) for each sample. Nanoparticle collection is concentrated along the high-field region on the outer edges of the electrodes. Fluorescent imaging showed significant differences between all positive CLL samples processed as compared to healthy control samples, with relatively minor differences between trials run with whole blood versus plasma.

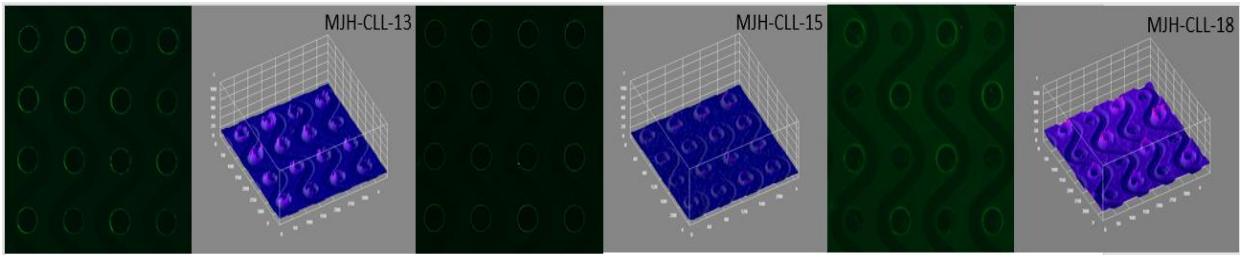

Figure 11.1: DEP microarray fluorescence from RNA extracted from CLL patient plasma. DEP isolated RNA was stained with Thermo Fischer CYTO RNASelect 488 fluorescent stain. ROR-1 specific RNA was confirmed via 2-step RNA stabilization and ssDNA amplification using New England Biolabs Fusion Taq High Fidelity qPCR reagent kit.

Fluorescent images identifying the ROR1 transmembrane-protein biomarker presence on the same sample subset, MJH_CLL_13, MJH-CLL-15, and MJH-CLL-18 are shown in Figure 7 and also include the relative fluorescent intensities via 3D surface plots to the right of each. Both

whole blood and patient plasma samples showed significant fluorescent signals indicating upregulation of the ROR1 protein, while healthy controls maintained consistently negative, with only background fluorescence detected in the image analysis. Figure 8 shows the cleaner and clearer images taken for biomarkers isolated and imaged from plasma as opposed to whole blood. Though signals are strong from both whole blood assays and plasma assays, the plasma based protocol offers much clearer, brighter and more defined signals. ROR1 presence also showed an interesting inverse correlation with the results from FACS analysis for the same patient samples. When relative fluorescent intensity was measured, samples reporting high presence of ROR1 protein in exosomes and extracellular vesicles generally showed low percent presence of ROR1 protein on B-cell lymphocytes, and vice versa, when analyzed via FACS analysis. For comparison, the same whole blood and plasma samples were processed through the existing gold standard Qaigen (Hilden, Germany) exoEasy Maxi Kit protocol, which can only be run with plasma, requires a minimum 200μL, suggests >500μL and requires sample filtration prior to EV isolation. ROR1 protein was not visualized on samples processes using the Qaigen kits, however target material was eluted and processed through PCR for validation of ccf-DNA and RNA presence.

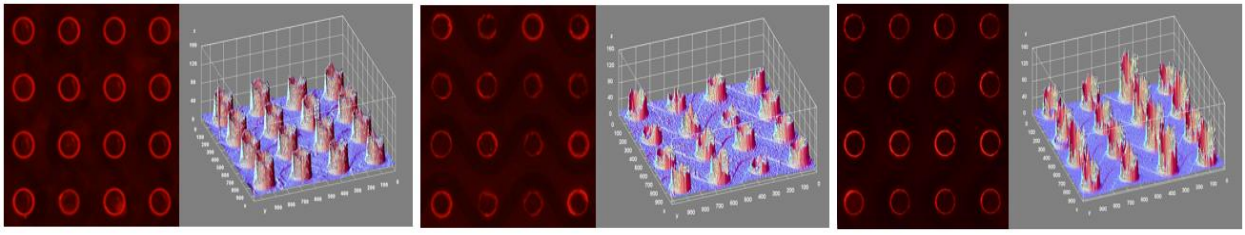

Figure 12.1: DEP microarray section and 3-D fluorescent intensity plot from chip isolation of CLL specific extracellular vesicles from CLL human patient whole blood sample. Stained for ROR-1 transmembrane protein using two-step immunofluorescent protocol with ABCAM ROR-1 antibody at 1:800 dilution in PBS. (Left) Patient sample MJH-CLL-13 (Center) Patient sample MJH-CLL-15 (Right) Patient sample MJH-CLL-18. 3-D image renderings show relative fluorescence for each respective sample, images analysis performed using FIJI software.

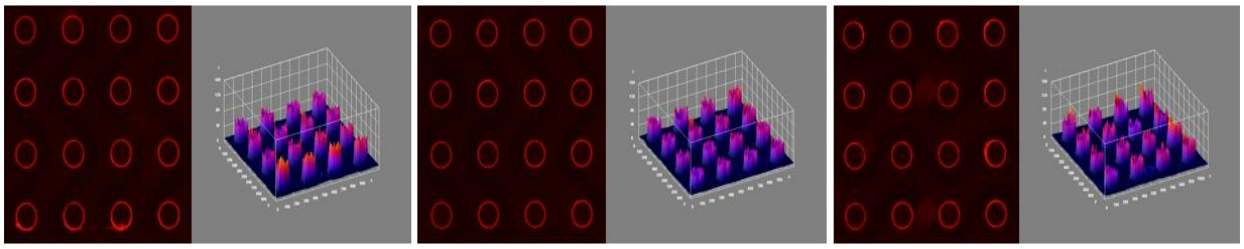

Figure 13.1: DEP microarray section and 3-D fluorescent intensity plot from chip isolation of CLL specific extracellular vesicles from CLL human patient plasma sample for comparison to whole blood assay. Stained for ROR-1 transmembrane protein using two-step immunofluorescent protocol with ABCAM ROR-1 antibody at 1:800 dilution in PBS. (Left) Patient sample MJH-CLL-13 (Center) Patient sample MJH-CLL-15 (Right) Patient sample MJH-CLL-18. 3-D image renderings show relative fluorescence for each respective sample, images analysis performed using FIJI software

PCR stabilization and amplification:

Peripheral blood and plasma samples processed on-chip and eluted for subsequent RT-PCR and qPCR amplification both successfully confirmed ROR1 DNA and RNA amplification. Samples eluted from the chip followed the seven-step protocol but were eluted in a 0.5x diluted TE buffer for better compatibility with downstream molecular biology protocols. Target RNA was released from the EV's and stabilized to single stranded c-DNA and directly afterwards was amplified and measured via q-PCR. The resultant c-DNA samples were amplified using two carefully designed primer sets, the first forward primer targeting the exon1-exon2 junction, and the reverse targeting the exon5-exon6 junction. The second set was designed with the forward primer spanning the exon3-exon4 junctions with a reverse primer coding within exon6. These specific primer designs allowed assurance that during RNA specific thermal cycling, DNA would not be amplified and mask our potential result. The successful amplification of target RNA transcripts also confirms the validity of RNASelect fluorescent imaging.

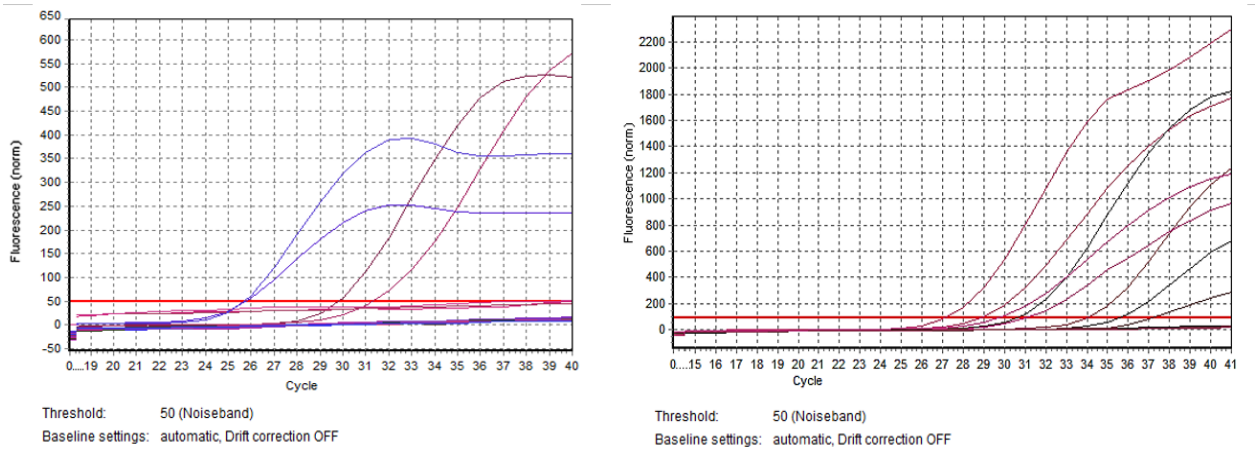

Figure 14.1: qPCR DNA amplification curves for DEP isolated CF-DNA samples from CLL patient plasma: MJH-CLL-13, MJH-CLL-15 and MJH-CLL-18. DNA was amplified using Q-5 High Fidelity PCR kit from New England Biolabs, Ipswich, Massachusetts. Samples were amplified on an Eppendorf Mastercycler Pro-S thermal cycler.

Captured and eluted ccf-DNA was amplified using random hexamers and the One Taq Phusion High-Fidelity DNA Polymerase from New England biolabs. Of the 15 plasma samples processed and eluted from on-chip isolation protocols, RNA was successfully stabilized and amplified from 14 samples. Of 10 total whole blood samples, RNA was successfully stabilized an amplified from 6 total samples. With a complete sample cohort of n=28, 20 total samples were successfully processed from isolation to RNA fluorescent imaging, ROR1 protein immunofluorescent imaging, elution of RNA and DNA for amplification and confirmation of the target gene upregulation. 60% of whole blood samples were successfully interrogated and analyzed to the protocols full set of targets, where 93% of trials conducted using patient plasma samples were successful to the experiment's full objective.

DISCUSSION

Leveraging the invaluable information that is encapsulated in extracellular vesicles and exomes-type nanoparticles a versatile, dependable, and affordable technology is necessary[70]. The

current industry gold standard requires expensive equipment as well has meticulous and laborious protocols that take hours or days to complete. These long processes allow for many points of technical error and or sample damage. The Biological Dynamics microarray device offers improvements and answers to all these demands. The device architecture allows for any type of liquid sample interrogation. In this study cell lysates in buffers controlled for favorable electrochemistry and concentration were processed with similar ease as whole blood CLL samples thickened by the high concentration of B-cell lymphocytes as an effect of the patient's advanced condition. The technology can process a wide range of sample sizes, drawing conclusive evidence from samples as small as 20 μL, while showing capacity to process nearly 250μL of human plasma before microelectrodes reach full capture saturation. It offers rapid processing, needing only 25 minutes to achieve 50 μL of isolation and elution/collection of EV's and exosomes from a human plasma sample. This can be as much as a 10 to 12 hours of time saved, which becomes greater still, if one accounts for the multiple intermediate analytical steps that can be designed into the isolation/capture protocol. Moreover, it is unclear the effects or damages incurred during these long sequential steps and aggressive ultracentrifugation and how they may alter or effect the final diagnosis. The microarray device allows for the sample to be processed and target material to be isolated and captured without exposure to extreme temperatures, sheer forces, or filtration. This comprehensive protocol offers a viable technology for early disease detection, effective analysis for diagnostics, as well as monitoring capabilities all based on a semi-invasive blood based liquid biopsy.

Though finger-prick diagnostics have proven unfeasible and unreliable for disease detection and diagnostic applications, this technology proves the semi-invasive intravenous blood draw can truly offer doctors a window into a patient's health, disease condition or progress within

a therapeutic treatment plan. Greater efficacy and success rates are achieved via human plasma analysis verses human whole blood analysis with this method, however the functionality is clear for both sample compositions. The main challenges are presented by the extended washed required for whole blood processing. The whole blood processes' demand for overwhelming wash steps impacted fluorescent imaging of target material as increased background, likely due to non-specific binding occurring between the antibodies and the many transmembrane proteins present within red blood cell's cell membrane. These problems proved problematic for downstream molecular biology as well. Difficulties balancing the PCR chemistry for amplification of nucleic acid targets can likely be attributed to the presence of enzymes, sugars and metalloproteins associated ruptured red blood cells. The differences in subsequent processing could also have been a result of the combined effects from interferences in particle kinetic and lower effective isolation of target material for whole blood sample as compared to plasma. With red blood cells making up 40-45% whole blood's volume, the whole blood samples would be expected to contain 40-45% less EV and exosomes carrying plasma, and thus, less target material for isolation. Adjustments to device architecture could be a solution to the extended washes and the increased stress placed on whole blood samples. A taller flow chamber without sharp curves or corners would reduce sheer interfaces that cause the need for longer wash steps and likely rupture cells.

Immunofluorescent imaging results were validated using a carefully organized set of positive and negative control samples coordinated with an established algorithm for calculating the fluorescent intensity. The algorithm, designed using the Fiji Image analysis software (NIH) calculates the fluorescent intensity in a region of interest around each electrode, separately calculates an average background fluorescence signal that is then subtracted from each ROI to determine true fluorescent signal intensity. First, a set of two distinct polyclonal and monoclonal

antibodies were selected based on literature representing similar assays. Both monoclonal and polyclonal antibodies accounted for potential variability in orientation, nature and affinity of the targeted ROR1 transmembrane protein. The HEK 293 cell lysate positive control was carefully designed to facilitate an optimal collection and isolation event. The cell line was chosen based on literature having shown a high expression and concentration of the ROR1 protein within this cell line. The lysate was diluted to offer a thin, non-viscous, particle rich sample with calculated electrochemistry to optimize the device activity and collection field. This high concentration positive allowed for careful titration of both antibodies to better establish a saturation point and an effective dilution for the initial trials. The healthy human plasma negative control allowed for a low baseline to help establish the background subtraction for relative fluorescence calculations. The healthy negative control also allowed for antibody validation based on levels of non-specific binding of the antibody to any of the many IgG, albumin and membrane proteins that are naturally present in human peripheral blood. Using these careful steps, it was determined that the Abcam polyclonal antibody offered the experiment both the activity, specificity and consistency needed for sound conclusive results. The confidence in the antibody trials was key to noticing the interesting inverse correlation between presence of ROR1 transmembrane protein and ROR1 presence on B-cell Lymphocytes. This inverse presence may be representative of different points of origin for the EVs at different phases of CLL cancer progression or could even be some means of variation between patient to patient disease expression. A greater scrutiny of a longitudinal sample cohort could clarify the source and the reasoning for this different location for this genetic upregulation.

The specific order of the particle isolation and particle staining was carefully established with consideration for material liability, wash steps, and cross contamination. The RNASelect

staining of RNA particles was performed first due to the high activity and volatility of RNase enzymes in blood and plasma samples. Even with careful wash steps and RNase inhibitors, the staining and imaging had to be performed on a truncated incubation and wash time sequence to avoid sample degradation. Nevertheless, fluorescence intensity was noticeably lower due to RNA degradation and signal fading, just within the two to four-minute time window for subregion selection and image exposure/capture. The reintroduction of remaining sample allowed for isolation and ROR1 immunofluorescent imaging. Initially the antibodies were introduced and left to incubate overnight at 4 °C to offer optimal binding kinetics and was expedited to a 45-minute room temperature incubation once dilution concentrations and step-by-step protocols were tested more rigorously.

Protecting the nucleic acids, particularly RNA, during intermediate wash steps, elutions and reagent mixing demanded careful consideration. After immunofluorescence images were captured, the elution protocol allowed for release of the protective polyHEMA perm layer and the pipetting out of target EV and exosome sample. RNase/DNase-free microcentrifuge tubes were prepared with a single microliter of RNase inhibitor to ensure protection of the eluted samples' nucleic acid content. Once the eluted sample and RNase inhibitor was well mixed, the TWEEN-20 spike was added to dissolve the lipid bilayer protective membrane of the EV's and release the RNA. Even with these precautions, PCR proved difficult. Difficulties could most reasonably be ascribed to the high concentration of contaminants and aggregate bioparticlae that were present in the sample. The large chains of the primary and secondary antibodies likely created a significant interference for molecular kinetics during the thermal cycling process. New approaches involving cycling immunofluorescence and the release of these antibody chains can and will likely offer better and easier PCR-based verification of target biomarkers and gene presence. The device also

attracts and captures a great deal of blood derived aggregate proteins and debris, that could be greatly reduced to offer greater sample purity and make for simpler kinetics in PCR thermal cycling.

MATERIALS & METHODS:

Blood and Plasma samples:

Blood and plasma samples were collected at the Moores Cancer Center in San Diego, CA and provided by the Thomas Kipps research laboratory. Blood samples were collected from 18 patients with positive chronic lymphocytic leukemia diagnosis, all blood was drawn during clinical treatment for their conditions. Negative controls were drawn from 3 healthy volunteers. (IRB number 171884) Whole blood samples were drawn into lithium heparin coated collection tubes and stored at 4C for no longer than 48 hours. Plasma samples were drawn into the same lithium heparin coated collection tubes and centrifuged for 15 minutes at 1100 RCF, plasma supernatant was pipetted into 2.5 mL RNase/DNase-free Eppendorf brand microcentrifuge tubes.

Cell lines, culture and Lysate:

A human kidney cancer cell line (HEK293) was used to establish a positive ROR1 control. HEK293 was cultured in DMEM supplemented with 10% fetal bovine serum, and 1% penicillin-streptomycin antibiotic growth media. Cells were grown through 3 passages and split and harvested at 70-80% confluency. Cells were centrifuged at 500 RCF for 5 minutes, culture media was aspirated, cell pellet was washed with PBS (Sigma-Aldrich), followed by a final centrifuge spin, again at 500 RCF for 5 minutes to prepare for cell lysate. Cell pellet was dissociated in RIPA lysis buffer and incubated on ice for 15 minutes and vortexed every 5 minutes and returned to ice. Lysate media was centrifuged a final spin, at 13,000 RCF for 5 minutes, lysis buffer decanted, and

final pellet was suspended in a 0.5x PBS buffer to offer maximum electrochemical compatibility with electrokinetic isolation parameters. Cell lysate was aliquoted and stored at -20 C in RNase/DNase free Eppendorf microcentrifuge tubes.

ACE Microarray Device:

The on-chip isolation and capture assay was run on the Biological Dynamics alternating current electrokinetic (ACE) microarray device. The offers a ~25 μL primary flow chamber that supports the rapid isolation of the Ev's, proteins and nucleic acids. The device interface hosts 1000 platinum microelectrodes, 60 μm in diameter evenly patterned in 3 panels across a 15 mm chip. The platinum electrodes are fabricated on a silicon substrate foundation and insulated by silicon-dioxide (SiO2), finally a porous poly(2-hydroxyethyl methacrylate) (polyHEMA) hydrogel was grown across the entire chip surface followed by a cover plate. A cross-sectional side view of the chip's respective layers is shown in Figure 5A. Figure 5B shows a COMSOL simulation of an active microelectrode subsection, displaying high field regions and magnitude and distribution of the electric field gradient along the chips surface. The chip requires a simple potassium buffered saline (PBS) pretreatment that allows for a more affable crossflow of thick whole blood samples and allows for a greater activation of the polyHEMA/electrode interface. Immediately following, the primary flow chamber was evacuated to help reduce sample/buffer mixing, and the blood sample was introduced to the device and the alternating current is applied. Specific frequencies are used to target desired material of interest. For Ev's and nucleic acids, a 10Vpp and 14kHz, AC signal was applied. Using a syringe puller set at 3μL/min flow rate, is drawn across the active microelectrode array and through the primary flow chamber. After just 10 minutes of capture RNA, DNA and EV's were ready for isolation, and a 0.5x diluted PBS wash buffer was applied to remove excess sample. After a 15-minute wash step, the material of interest was ready for

fluorescent staining and imaging. Depending on staining method and reagent application, sequential introduction and wash steps may be necessary. Concentrated target material can subsequently be eluted from the primary flow chamber and processed through various PCR protocols or successive analysis.

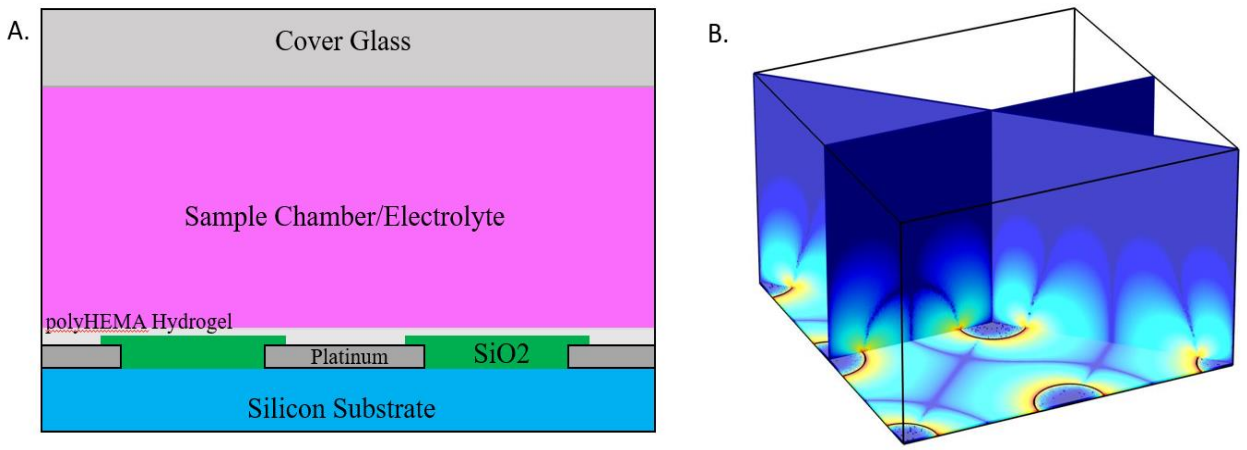

Figure 15.1: A) 2-D cross sectional diagram of ACE microarray chip. Electrodes repeat in both x and y lateral directions. The silicon substrate supports platinum electrodes and SiO2 covers the exposed substrate. The polyHEMA hydrogel coat then evenly covers the entire interface of the chip. Electrolytic sample allows for conductance between electrodes and chip activation, while the cover glass constrains the flow chamber. B) 3-D simulation of activated electrodes. Red orange and yellow rings depict high field regions immediately encompassing the electrodes, where DEP field strengths are greatest and target material is collected. The long diagonal plane runs through the center of same-polarity electrodes, the short plane runs through opposite-polarity electrodes.

Immunofluorescent and fluorescent stain:

Immunofluorescent and fluorescent staining was performed directly on chip and was imaged using fluorescent microscopy. ROR-1 target biomarker protein was targeted for its known upregulation in chronic lymphocytic leukemia conditions as well as its transmembrane location/orientation. Thanks to this convenient accessibility, direct antibody binding required no additional treatments or steps post capture and isolation. An unconjugated ABCAM (Cambridge, MA) anti-ROR-1 polyclonal antibody was introduced to isolated EV's and incubated between 45-

60 minutes at room temperature. An Invitrogen (Carlsbad, CA) Texas Red goat anti-rabbit secondary antibody was coordinated with anti-ROR1 primaries, incubations were again 45-60 minutes. Samples were washed with 0.5x PBS buffer, then visualized and imaged for further analysis. All samples and protocols were monitored continuously throughout microarray activity using an Olympus BX51W epifluorescence microscope with a 4x objective and imaged using Olympus software. All images were collected on the same acquisition specifications.

On chip RNA fluorescent staining was performed using a Thermofischer (Carlsbad CA) CYTO RNASelect 488 (FITC) minor groove binding stain. Blood samples were introduced to the device and material of interest was captured and isolated using the same 10-minute collection and 15-minute wash steps, as well the same 10Vpp and 14kHz, AC signal was applied. Because viable RNA was only expected to be found within the protective lipid bilayer of the extracellular vesicles, the outer membranes were permeablized using a 0.1% concentration saponin buffer for 10 minutes directly on chip. RNASelect stain was incubated for 10 minutes at room temperature, washed an imaged using the same Olympus BX51W epifluorescence microscope and 4x objective, using Olympus imaging software.

RNA and DNA extraction from whole blood samples:

Isolation from whole blood sample was done in two semi-batch interrogations. 50μL aliquots of individual whole blood samples were introduced to the ACE microarray device at a time and interrogated for 10 minutes to isolate EV's and nucleic acid material of interest. For this target isolation, two cycles of 25μL of blood sample were interrogated by a 10Vpp and 14kHz, AC signal. A syringe puller set to 3μL/min draw rate, controlled sample movement across the active microelectrode array. After just 10 minutes total capture (2 cycles for 5 minutes each) RNA,

DNA and EV's were ready for isolation, and a 0.5x PBS wash buffer was applied to remove excess sample. A 15-minute wash step purified the material of interest for fluorescent staining and imaging. After the 90-minute ACAM ROR1 indirect immunofluorescent protocol was complete, an elution protocol liberated the samples from the chip. The AC signal was adjusted to a voltage of 18-20 Vpp with a 5Hz signal frequency. Elution or "push-off" signal was pulsed to avoid chip burnout and sample damage. Once the detachment of the polyHEMA coating was visually confirmed, the inlet and outlet hoses were removed, and the remaining sample was aspirated using an Eppendorf pipette, and 1x PBS was buffer. 1 μL of Invitrogen (Carlsbad, CA) SUPERase RNase inhibitor was added to protect target RNA, and eluted material was lysed with a 1% concentration of Tween-20 to release the nucleic acid samples for immediate processing.

Fluorescently Labeled ROR1 Biomarker Quantification

To establish a quantitative measure of the levels of fluorescent labeled ROR1 protein biomarkers isolated from samples, it was first necessary to establish high and low (positive and negative) control measurements as a zero baseline. Healthy human peripheral blood and plasma samples were both tested to establish a zero baseline for a background fluorescence subtraction. This zero-baseline allowed for the quantitation algorithm to account for non-specific binding interactions between labeled antibodies and various blood-based proteins, lipids and plasma elements. The HEK293 kidney cancer cell lysate, together with the ABCAM Anti-ROR1 antibody was used to establish a positive control range to coordinate dilution rates, incubation schedules, wash schedules and imaging parameters. The cell lysate also offered the ability to control electrolyte concentrations and sample viscosity to establish a capture and isolation standard under blood/plasma-like concentrations as well as optimal system conditions.

The positive and negative control standards also allowed for a careful antibody validation and dilution titration to ensure fluorescent signaling was truly representative of the target material being captured from patient samples. Two initial antibodies were selected based on literature publications of similar application; the first a BD Pharmingen (San Jose, CA) mouse isotype, anti-ROR1, monoclonal unconjugated; the second an Abcam (Cambridge, MA) rabbit isotype, anti-ROR1, polyclonal unconjugated. Validation proved the latter to offer much more rapid binding nature along with strong selectivity at a 1:800, antibody to phosphate buffered saline (PBS) dilution, and thus all trials used the polyclonal Abcam anti-ror1 antibody. All experimental protocols relied on PBS for dilution and wash steps. 0.5x PBS was proven to serve better for any protocol steps which required chip activation however to offer better biocompatibility, for all steps performed on inactive chips, 1.0xPBS was applied.

An image processing algorithm was established using ImageJ image software ("FIJI", National Institute of Health, Bethesda, MD). First, a subsection of 25 (5x5) electrodes from the mircoarray were selected based on consistency and uniformity of fluorescent signal. Eight electrodes from that subset were then selected for the same characteristics, and a circular region of interest is highlighted around each electrode. Pixels are measured to establish individual color intensity, allowing for a background subtraction, a resultant mean fluorescent intensity and a standard deviation calculation. 3D surface extrusion plots of the selected microarray sub sections were rendered using the "3D interactive viewer" plug-in for ImageJ.

RT-PCR and q-PCR stabilization and amplification:

RNA extractions from whole blood samples were stabilized to cDNA using the ProtoScript II First-Strand cDNA synthesis kit. An Eppendorf MasterCycler Pro-S thermal cycler was set to

a 98 degree, 30 second denaturation step followed by 35 cycles of, 98 degrees for 10 seconds, 57 degrees for 30seconds, and 72 degrees for 30 seconds, finished with a 72 degree, 10 minute final extension. Second-step cDNA and DNA qPCR amplification was performed using One Taq Phusion High-Fidelity DNA Polymerase (New England Biolabs). Direct ccf-DNA amplification was performed using two primer sets carefully designed avoid non-specific DNA amplification. Forward primer #1 targeted the exon1-exon2 junction where the #1 reverse primer targeted the exon5-exon6 junction. Forward primer #2 was selected to span the exon3-exon4 junctions with the #2 reverse primer coding within exon6. Thermal cycler parameters were set to a 5-minute initial denaturation step at 98 degrees followed by 40 cycles of 98 degree denaturation for 15 seconds, 66 degree annealing for 15 seconds and 72 degree extension for 15 seconds. The PCR results were analysis via digital graph and excel data reports collected on Eppendorf MasterCycler software.

CHAPTER: 4

"Bacterial Outer Membrane Vesicles as a Microbiomic Addition to Liquid Biopsy-Based Disease Detection"

ABSTRACT:

The never-ending race to defeat cancer has called upon every field of science and has taken contributions from scientific and medical institutions world-wide. The "cure" the world is looking and waiting for may not be a treatment at all, however. The answer to defeating these life-threatening conditions may lie in pushing detection technologies as far forward as possible. Unique conditions like triple negative breast cancer have forced researchers and clinicians to find different leverage points to diagnose, treat and eliminate these cancers. Advances in early detection are now leveraging cancer derived biological nanoparticles or vesicles that carry unique information about disease and patient condition. Another way forward for these technologies may be via bacteria derived vesicles that may be excreted from the unique microbiome that inhabits the tumor microenvironment.

Here we have developed an early validation for the collection and isolation of these microbiomic outer membrane vesicles (OMV) on a dielectrophoretic microarray device for early detection and diagnostic applications. The validation of these particles not only opens new avenues for early detection, but also new access points to characterize the tumor microenvironment more clearly. These OMVs were cultures from a common Dh5-alpha *Escherichia coli (E.coli)* bacteria,

spiked into and isolated from whole blood samples using an electrokinetic microarray device. Researchers ability to access and interrogate these microbiomic particles could expand the bank of key biomarkers for tumor characterization, condition diagnosis and ultimately treatment design.

INTRODUCTION

The effect of invasive microbes on the human body and its healthy functioning systems has been recognized for thousands of years. Both written and fossil records show evidence of antibiotic applications in ancient Egyptian culture as many as 3000 years ago[147,148]. During the 1800's, theories of "miasma" or "polluted bad air" gave way to the works of Pasteur and Koch and their contributions to modern germ theory[149]. History's organized scientific efforts brought us through the 20th century and Paul Ehrlich's early hypotheses regarding what would prove to be gram-positive and gram-negative bacteria and eventually his discovery of arsphenamine as an early treatment for syphilis[150,151]. The 20th century would also bring Metchnikoff's investigations of probiotics, Alexander Flemming's discovery of penicillin and the challenges of antibiotic resistance. The relationship of bacteria to cancer and the exploration of bacteria as a marker of cancerous disease conditions would follow soon after[152]. Much of this understanding started with doctors' connection of an abnormal gut and fecal microbiome to gastrointestinal and colonic cancers. These correlations have since expanded to breast, ovarian and lung cancers with numerous others under thorough investigation[153–156].

Directed efforts to explore the prosperity of the human microbiome led to a better understanding of the systemic effects of probiotics, invasive and opportunistic microbes and unique discoveries like bacterial minicells in the 1960's[157]. Advances in understanding and technology produced clearly defined characterizations between gram-positive and gram-negative

derived vesicles and an exploration of minicell biogenesis. Initial isolation methods relied on 10,000-15,000 x g centrifugal density separations. As the developments of the ultracentrifuge offered processing capabilities beyond 100,000x g, different bacterial vesicle subgroups were defined and various bioactivities were clarified[158]. Characterization efforts quickly described the diversity of minicells and defined new particles as outer membrane vesicles (OMVs) while inciting suggestions that they may be useful for diagnostic or therapeutic applications like drug delivery[159,160].

There is increasing evidence that certain bacteria are associated with the development of different types of cancer[161,162]. Often these bacteria are taking advantage of the necrotic regions within the tumor where the immune response is suppressed, and oxygen levels are low. Ovarian cancer is one of these diseases. Studies looking at the bacterial content of ovarian tumor tissue and nearby healthy tissue reveal that the tumors show a significant increase in the species *Acinetobacter lwoffii* as well a significant decrease in other microbe abundance and biodiversity[163].

Tumor tissue has leaky vasculature, which could allow for bacteria in the tumor to be released into circulation. Investigations of the blood from colon cancer patients has shown extremely high levels of bacterial DNA in the buffy coat and blood plasma[164]. Other particles secreted by bacteria, such as outer membrane vesicles could also be released and circulate without immune response or detection; similar to eukaryotic extracellular vesicles or exosomes. Both provide sources of potential biomarkers for early cancer detection and diagnosis. The presence of bacteria can also indicate that the tumor is expanding aggressively, allowing the presence of bacterial derived biomarkers to potentially assist in differentiation of slow growing tumors from ones that are more aggressive.

This study validates the use of dielectrophoresis as a capable technology for the capture and isolation of bacteria derived biomarkers and OMVs. First, a model *Escherichia coli (E.coli)* bacterium was designed to offer as an aggressive growing, anaerobic bacterium that exhibited a fluorescent outer cell membrane to form traceable OMVs and minicells. Then, an *in vitro,* tumor-like environment and method was created for effective bacterial induction of mini cell formation, OMVs and other naturally occurring bacterial particulates. Minicell and outer membrane vesicles were isolated using a protocol of high-speed centrifugation, filtration and finally ultracentrifugation to create a purified concentrate to be introduced to the samples. In order to determine the optimum alternating current (AC) frequency for detection, various concentrations of bacterial vesicle in blood and plasma samples were created and quantified and evaluated. Finally, isolated OMV and minicells were analyzed using a series of Fluorescence-Activated Cell Sorting (FACS) analyses to confirm the particles were in fact vesicles, and not simply ambient fluorescent protein in the sample. OMVs and bacterial minicells may offer a way for researchers and clinicians to confirm the presence of particular cancer specific bacterium in patient blood samples. They may also help describe critical aspects of the tumor microenvironment for a more comprehensive understanding of the patient's condition. This work proves that bacteria, bacterial vesicles and bacterial microparticulates show real potential for creating more comprehensive biomarker cocktails to detect, diagnose and treat various cancers and other disease conditions.

RESULTS:

Design and Incubation Parameters for *E. coli* Bacteria Cultures for OMVs and Minicells

DH5-Alpha *E. coli* was chemically transformed using two different plasmids (sfGFP-N1 pET-39b(+) and pET-28), each offering direct fluorescent imaging of collected bacteria and

particles produced from the resultant cultures. sfGFP-N1 pET-39b(+) was cloned from a pSFGFP-N1 stab purchased from Addgene,(Watertown, Massachusetts) and a pET39b(+) plasmid from Novagen/Thermo Fisher (Waltham, Massachusetts). Bacterial streaks for both variants showed Green Fluorescence Protein(GFP) fluorescence in nearly all colonies. Both bacterium variants were grown successfully under hypoxic, acidic conditions at 37°C in a CO_2 buffered incubator and produced vesicles and minicells. Concentration and GFP content of the vesicles produced by the sfGFP-N1 pET-39b(+) vector transformed *E. coli* were more uniform and consistent. The pET-28 vector produced a clear overexpression of GFP that was found in abundance in the filtered and isolated sample but was difficult to distinguish from viable OMVs and minicells. Due to imaging technique, the fluorescent protein contained within an OMV or minicell is essentially indiscernible from an ambient or aggregate fluorescent protein that has been excreted from the template *E. coli*.

E. coli OMV Validation and Analysis

Complete 1L Lysogeny broth *E. coli* cultures were aliquoted into equal 250mL centrifuge containers and spun at 10,000 G for 20 minutes to separate all live bacteria from the culture broth. Supernatant was then transferred to Amicon filtration flasks prepared with 10 Kilo Dalton filters for concentration. Filters were pre-soaked in a 5% TWEEN-20 solution to ensure OMVs and target material did not stick to column filters. Culture supernatant was concentrated to 200mL. Remaining sample was then aliquoted and balanced into a Beckman Coulter Ultracentrifuge for final OMV isolation. Samples were spun in a SW-32ti mini swinging bucket rotor at 120,000 G, for 90minutes. Supernatant was discarded and resulting pellet was resuspended in 1.0X PBS for -80C storage. Samples were validated using FACS analysis to confirm fluorescent proteins were encapsulated in the OMVs and not simple aggregate collected in the sample.

AC Signal and Isolation Assay

OMVs, minicells and bacterial particles were collected from the whole blood and plasma. The spiked plasma samples showed more clear and concentrated collection patterns than did the whole blood spiked samples. In trials, isolating material from samples spiked with 20% particle content showed signs of electrode saturation. Samples interrogated by AC signals above 18Vpp and 10kHz showed little to no signs of collection. Figures 10 A & B show the comparative difference between the live bacteria isolations (left) and OMV spike plasma isolations (right).

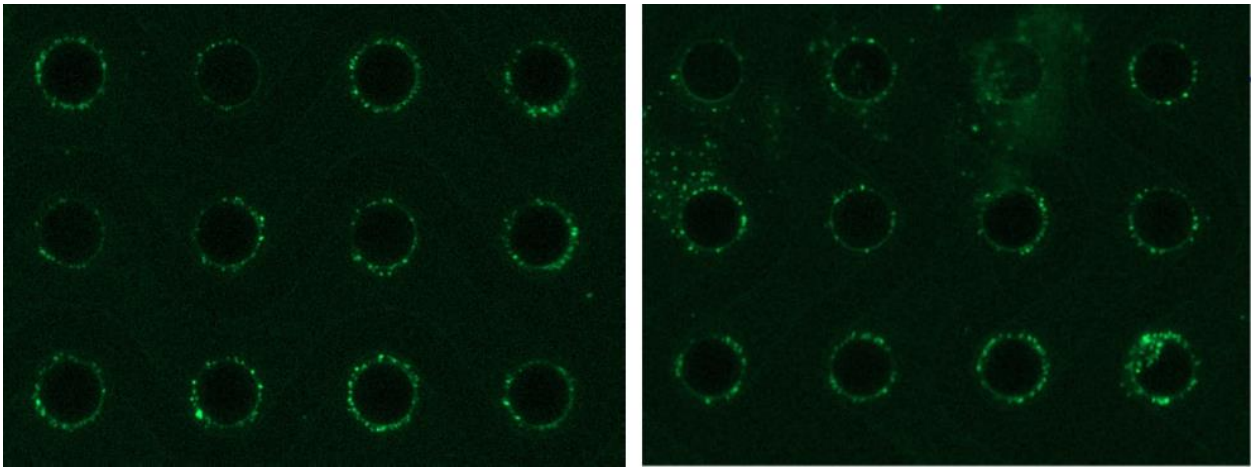

Figure 16.1: Plasma sample isolations show noticeable differences in signal clarity when compared to whole blood isolations. Electrode saturation and activation proved to be about equal, however clumps and clouds created by the red blood cells when exposed to the high voltages reflect significant amounts of fluorescence creating an overwhelming background during quantification.

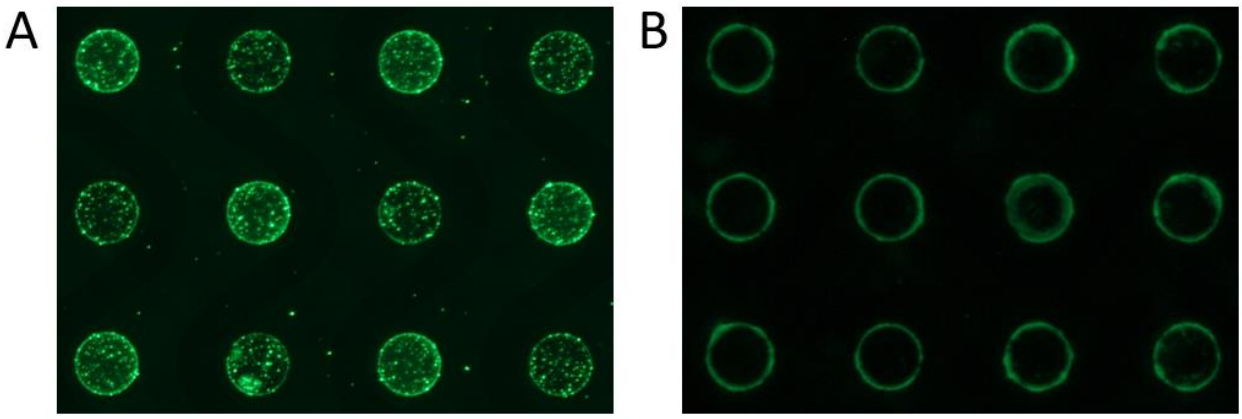

Figure 17.1: A) transformed DH5-Alpha *e. coli* bacteria, spiked into blood and isolated using a 10KHz, 10vpp system signal. B) Processed and purified OMVs spiked into whole blood, isolated using the same 10Khz, 10vpp applied signal.

DISCUSSION

For standardization, both *E. coli* variants underwent the same chemical transformation process. Though the dual layered cell envelop of gram-negative bacteria may require a more complex folding sequence to produce a viable minicell or vesicle, DH5-Alpha competent cells were chosen. DH5-Alpha competent cells were chosen as the model system based on numerous reports of OMV and minicell production, including the original discoveries having come from *E. coli*, along with the resilient and aggressive replicating nature. The two GFP vectors were carefully chosen as well. The pET-28 GFP vector was chosen for its extreme overexpression. Our hope was that the over expressive nature would push the GFP into the periplasmic space and result in non-specific translocation of the vector into the ideal region for encapsulation in the target OMVs and minicells. It would be difficult to definitively claim whether this overexpression resulted in a periplasmic translocation without more precise characterization, however it successfully produced the desired fluorescent OMVs and minicells. The concentration of sound and complete vesicles was relatively lower in comparison to the aggregate proteins and particles making the second

variant more attractive for further trials. The second vector was designed with a specifically targeted translocation within the periplasmic space. This allowed for greater encapsulation and more effective OMV and minicell formation. Further examination of the biogenesis of the OMVs and minicells of these *E. coli* variants in this particular environment would offer clarity to the nature of the vesicles. Based on reported literature, it is most likely that these particles are a result of overly aggressive replication during which, erratic cell division occurs resulting in unintended minicells. The minicell formation most likely initiates between the cell elongation phase and the formation of the septum during the division of the nuclear clusters at the initiation of cell division. Evidence lends towards the outer membrane vesicles being formed more consistently throughout the bacteria's life cycle as a means of cell-to-cell communication or material transfer. These relative phase differences for biogenesis will likely result in drastically different nature and carrying capacity and it will likely determine the scope of what can be achieved through the detection of these particles.

The BD FACS Symphony Analyzer allowed us to analyze the rough nature of the initial particles isolated from the culture media. For this sample analysis, the FACS technology is restricted by its lower range of detection. With a size limitation somewhere in the 300-400 nanometers range, it can only offer confirmation of minicells and not OMVs. Thus, we cannot confirm the presence of OMVs within our samples. The use of TWEEN-20 does, however, allow confirmation of formed and structured bodies that were disassociated and untraceable in the respective sample analyses.

It was well understood and expected that the isolation signals for OMVs and minicells would be different from that of eukaryotic extracellular vesicles (EVs) and exosomes however the magnitude was difficult to estimate. Multiple contributing factors play into the necessary isolation

frequency and signal strength necessary for successful capture and isolation of a target material. Factors to be considered in this effort included the unique double walled membrane of the *E. coli* *versus* the single lipid bilayer composition of the human derived EVs and exosomes. To establish an early understanding of what kind of interaction our samples would exhibit with the chip electric field and electrochemistry, a live *E. coli* culture was introduced to the chip, manipulated and captured for isolation. This allowed us to determine if the bacteria could survive the necessary field strengths necessary for isolation and ultimately the intensity of the electrode-media-lipopolysaccharide outer membrane interaction.

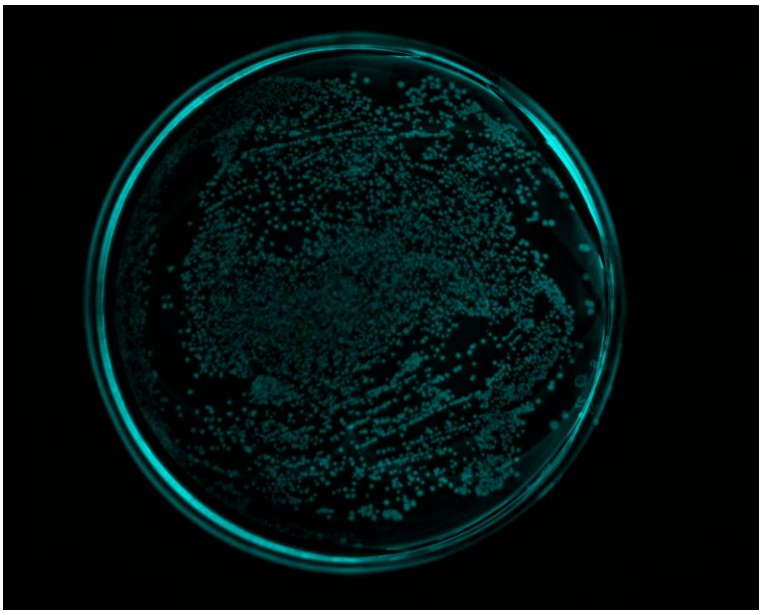

Figure 18.1: *E. coli* eluted from a standard whole blood extraction on chip protocol. (10% spike into whole blood, 10KHz, 10Vpp) is shown above after a 24 hour incubation at 37 degrees C, on a 2% agrose/LB broth plate. This shows clear evidence of viable GFP expressing bacterial colonies from the full protocol and elution. This allowed a better understanding of the intensity and stress induced on sample particles during the exposure to the electric field gradient.

The particle density may vary widely depending on the kinetics of formation the vesicle as well the OMVs contents. Lastly, the lipopolysaccharide tendrils on the extracellular membrane carry and respond to charge differently than the non-charged lipid bilayer membrane of EVs and

exosomes. This charge will cause a response to the time averaged electrophoretic force, which for lipid membranes is negligible. With all factors taken into consideration, rough estimate ranges allowed for tuning and optimal isolation. Initial signal validation trials relied on blood plasma due to the simplified kinetics due to the absent red blood cells. Additionally, the complex microfluidics of red blood cells clustering and migrating slowly during wash cycles can make clear imaging difficult, due to the lost target material as well as red blood cell signal interference. The final AC signal of 10kHz at 10Vpp allowed for collection, capture and protection of the fragile particles during washes. More so than eukaryotic derived EVs and exosomes, the OMVs and minicells were prone to burn out and degradation due to electric field effects and joule heating around high field zones on the electrode surfaces.

MATERIALS & METHODS

E. coli Cell Transformation:

In this work, two different *Escherichia coli* bacteria were designed using recombinant DNA technologies to achieve the desired OMV and minicell particles. A DH5-Alpha competent *E. coli* was used to establish a model for the production of bacterial OMVs and minicells. To simplify downstream processing, the *E. coli* was transformed with a pET-28 GFP fluorescent vector and induced using 0.5M Isopropyl-beta-D-thiogalactoside (IPTG) to allow for direct fluorescent imaging. A standard LB broth was mixed in house for the pET-28 plasmid expansion growth. A GeneJET Plasmid MaxiPrep kit (Thermo-Fischer Scientific, Waltham, MA) was used to isolate the pET-28 implant plasmid, and a chemical transformation was used to implant the fluorescent vector into the DH5-Alpha competent *E. coli*. Once implanted, a 6-hour culture readied the sample for induction, and the 0.5M IPTG was added at a 1:1000 concentration for a final

concentration of 0.5 mM and incubated overnight at 37°C. After overnight growth, the cells were steaked on a 2% agarose-LB broth plates, with 0.1% kanamycin antibiotic to allow isolation of a successfully transformed and induced cells. Three successfully transformed colonies were selected, cultured and cryopreserved at -80°C as a reserve. A second periplasmic SuperFolder GFP plasmid was grown using psfGFP-N1 and pET-39b(+) vectors to clone a second GFP protein sequence with a targeted implantation region. The two vectors were grown using standard LB broth in a 37°C incubation. psfGFP-N1 was gel-purified for 750 base pair fragments and digested using HindIII-HF and NotI-HF from New England Biolabs (Ipswich, MA) per the manufacturer's instructions. pET-39b(+) was also isolated using gel purification and ligated to the sfGFP-N1 cut vector to create the necessary sfGFP-N1 pET-39b(+) vector for chemical transformation into DH5-Alpha competent *E. coli*. The transformed culture was screened using the same plate streak incubation, and successfully fluorescent colonies were cultured and cryopreserved at -80°C. This second vector allowed for the inclusion of a site-specific plasmid that placed the fluorescent protein into the periplasmic region of the outer membrane, increased the amount of encapsulated fluorescent protein, and ultimately created fluorescent OMVs and minicells.

In vitro Cell culturing:

The DH5-Alpha competent *E. coli* was chosen for its particularly aggressive replication rate and resilient nature. To mimic the volatile microenvironment created by tumor growth, a 37°C hypoxic incubation was created using an airlock-S-bubble grommet. To help buffer the preparation and processing from O_2 exposure, the Erlenmeyer culture flask was kept in a CO_2 buffered incubator. The bacteria were cultured in a 1L Erlenmeyer flask with an acidic LB broth adjusted to a pH of 6.5 using 1M HCl to emulate the tumor microenvironment, with 0.1% kanamycin to

select for target bacterial growth. LB broth and kanamycin antibiotic were prepared in house. All culture broths and equipment were autoclaved to reduce risk of contamination. Cultures were grown a full 24 hours past the standard 80-90% confluence to impose another level of stress on the cells. Though aeration was not of concern for the bacteria, both cultures were incubated on a low set mixing table to keep uniform growing conditions throughout the sample.

Minicell/OMV/Particle Concentration:

Due to the uncertain ability to induce the necessary stress on the bacterial cultures to motivate substantial OMV and minicell production, a 1L culture was established to ensure a suitable resultant sample. Once cultures were ready for separation, the bacteria were transferred to four, 300mL high-speed centrifuge canisters and spun at 20,000x g and 4°C for 20 minutes to separate all cells, large cell material and large aggregate material. Sample supernatant was transferred to a 500mL Amicon Ultra pressure-based concentrator system (Sigma-Aldrich, Kenilworth, New Jersey) and processed through a 10kDa filter for concentration. The concentrated sample was then placed into a Beckman-Coulter Optima Max-XP Table-top Ultracentrifuge (Brea, CA) and spun at 120,000x g and 4°C for 2 hours using a (----I have to look up rotor type---) using. The final sample was resuspended in 500μL of sterile 1xPBS, aliquoted into 2.5 mL Low-bind RNase/DNase free Eppendorf microtubes and stored at -80°C.

Particle Characterization:

The depth of particle analysis accessible to this study was limited to Fluorescence-Activated Cell Sorting (FACS) analysis. This was made easier by the fluorescent labeled particles we had designed. Our samples were organized in gradually increasing concentrations starting with the pure PBS buffer as a blank or baseline, 5%, 10%,15% and 20% particle concentration. Each

sample was paired with a second sample of equal concentration which was given a 1% TWEEN-20 addition to disassociate any organized, encapsulated particles. All 10 samples were run on a BD Biosciences FACS Symphony Analyzer (Franklin Lakes, NJ) and data was recorded and analyzed with BD device specific software.

Sample Preparation & on-chip Isolation:

Initial particle isolation was performed using healthy normal human plasma as a sample base for the 5%,10%,15% and 20% cultured particle additions. Healthy human normal samples were collected by the Knight Cancer Institute biorepository under IRB # 18572. Once AC signals and isolation protocols had been validated using spiked plasma samples, the same sample concentrations were created using healthy human whole blood samples, and the same isolation was performed. Particles were isolated from both plasma and blood samples using the Dielectrophoretic ACE microarray device from Biological Dynamics (San Diego, CA). The device was activated with an AC signal of 12Vpp and 12kHz for 10 minutes of direct isolation, followed by a 10-minute wash with the AC signal remaining on. Whole blood samples were interrogated by the same signal, but wash cycles were 20-minutes to allow complete removal of red blood cells.

BIBLIOGRAPHY

1. Mottelay, P. F. Bibliographical History of Electricity and Magnetism. *Charles Griffin Co* 732 (1922).

2. Abraham, M. *The classical theory of electricity and magnetism*. (Blackie, 1932).

3. Hatfield, H. S. *Reports from Commissioners and Inspectors*. (1924).

4. Pohl, H. A. The Motion and Precipitation of Suspensoids in Divergent Electric Fields. *J. Appl. Phys.* **22**, 869–871 (1951).

5. www.ncbi.nlm.nih.gov. dielectrophoresis. (2020).

6. States, U. United States Patent and Trademark Office. *http://patft.uspto.gov/netahtml/PTO/search-adv.htm* http://patft.uspto.gov/netahtml/PTO/search-adv.htm (2020).

7. Abd Rahman, N., Ibrahim, F. & Yafouz, B. Dielectrophoresis for Biomedical Sciences Applications: A Review. *Sensors (Basel, Switzerland)* vol. 17 (2017).

8. Pethig, R. Review-where is dielectrophoresis (DEP) going? *J. Electrochem. Soc.* **164**, B3049–B3055 (2017).

9. Viefhues, M. & Eichhorn, R. DNA dielectrophoresis: Theory and applications a review. *Electrophoresis* vol. 38 1483–1506 (2017).

10. Hughes, M. P. Fifty years of dielectrophoretic cell separation technology. *Biomicrofluidics* **10**, 1–9 (2016).

11. Regtmeier, J., Eichhorn, R., Viefhues, M., Bogunovic, L. & Anselmetti, D. Electrodeless dielectrophoresis for bioanalysis : Theory , devices and applications. *Electrophoresis* 2253–2273 (2011) doi:10.1002/elps.201100055.

12. Castellanos, A., Ramos, A., Gonzalez, A., Green, N. G. & Morgan, H. Electrohydrodynamics and dielectrophoresis in microsystems: scaling laws. **36**, 2584.

13. Weng, P.-Y., Chen, I.-A., Yeh, C.-K., Chen, P.-Y. & Juang, J.-Y. Size-dependent dielectrophoretic crossover frequency of spherical particles. **10**, 11909.

14. Saucedo-Espinosa, M. A., Rauch, M. M., LaLonde, A. & Lapizco-Encinas, B. H. Polarization behavior of polystyrene particles under direct current and low-frequency (less 1kHz) electric fields in dielectrophoretic systems. **37**, 635–644.

15. Heineck, D. P. High-Conductance Electrokinetic Device Charactrerization and Design. (University of California San Diego, 2017).

16. Pethig, R. Review Article — Dielectrophoresis : Status of the theory , technology , and applications. **022811**, (2013).

17. Pethig, R. Limitations of the Clausius-Mossotti function used in dielectrophoresis and electrical impedance studies of biomacromolecules. *Electrophoresis* **40**, 2575–2583 (2019).

18. Allen, P. B. Dipole interactions and electrical polarity in nanosystems: The Clausius-Mossotti and related models. *J. Chem. Phys.* **120**, 2951–2962 (2004).

19. Heineck, D. P., Heller, M. J., Sarno, B. G. & Kim, S. Electrochemical Attack and Corrosion of Platinum Electrodes in Dielectrophoretic Diagnostic Devices. 1–11.

20. Malmberg, C. G. & Maryott, A. A. Dielectric constant of water from 0 to 100. **56**, 1–8 (1956).

21. Gallo-Villanueva, R. C. *et al.* Joule heating effects in optimized insulator-based dielectrophoretic devices: An interplay between post geometry and temperature rise. *Electrophoresis* **40**, 1408–1416 (2019).

22. Hagedorn, R., Fuhr, G., Müller, T. & Gimsa, J. Traveling-wave dielectrophoresis of microparticles. *Electrophoresis* **13**, 49–54 (1992).

23. Vykoukal, J. *et al.* A Combined Dielectrophoretic and Field-Flow Fractionation Microsystem for Biomedical Separation and Analysis. *Micro Total Anal. Syst. 2000* 127–130 (2000) doi:10.1007/978-94-017-2264-3_29.

24. Martinez-Duarte, R., Camacho-Alanis, F., Renaud, P. & Ros, A. Dielectrophoresis of lambda-DNA using 3D carbon electrodes. *Electrophoresis* **34**, 1113–1122 (2013).

25. Drews, A. M. RATCHETED CONTACT CHARGE ELECTROPHORESIS. (2014).

26. Hermanson, K. D., Lumsdon, S. O., Williams, J. P., Kaler, E. W. & Velev, O. D. Dielectrophoretic assembly of electrically functional microwires from nanoparticle suspensions. *Science (80-.).* **294**, 1082–1086 (2001).

27. Richetti, P., Prost, J. & Barois, P. Two-Dimensional Aggregation and Crystallization of a Colloidal Suspension of Latex Spheres. *J. Phys. Lettres* **45**, 1137–1143 (1984).

28. Velev, O. D., Prevo, B. G. & Bhatt, K. H. On-chip manipulation of free droplets. *Nature* **426**, 515–516 (2003).

29. Vijayaraghavan, A. *et al.* Dielectrophoretic assembly of high-density arrays of individual graphene devices for rapid screening. *ACS Nano* **3**, 1729–1734 (2009).

30. www.siliconbiosystems.com. deparray-system. (2020).

31. N. A. M. Yunus, N. F. Ismail, N. G. G. and D. A. 'Analysis of dielectrophoresis AC electrokinetic in equilibrium using Matlab,'. in *Asia Pacific Conference on Postgraduate Research in Microelectronics and Electronics* (2017).

32. Hilton, S. H. & Hayes, M. A. A mathematical model of dielectrophoretic data to connect measurements with cell properties. *Anal. Bioanal. Chem.* 2223–2237 (2019) doi:10.1007/s00216-019-01757-7.

33. Guerrieri, G. M. ; N. M. ; A. L. ; L. A. ; M. T. ; R. A lab-on-a-chip for cell detection and manipulation. *IEEE* (2003).

34. Guerrieri, N. M. ; A. R. ; G. M. ; L. A. ; A. L. ; M. T. ; R. A CMOS chip for individual cell manipulation and detection. *IEEE* (2003).

35. Cox, B. D. Patent Application Publication (10) Pub . No .: US 2002 / 0124603 A1. **1**, 1–5 (2002).

36. Fabbri, F. *et al.* Detection and recovery of circulating colon cancer cells using a dielectrophoresis-based device: KRAS mutation status in pure CTCs. *Cancer Lett.* **335**, 225–231 (2013).

37. Manaresi, F. Z. B. G. M. N. DEPArray™ Technology for Single CTC Analysis. *Circ. Tumor Cells* (2016).

38. Sabuncu, A. C., Liu, J. A., Beebe, S. J. & Beskok, A. Dielectrophoretic separation of mouse melanoma clones. *Biomicrofluidics* **4**, (2010).

39. Barisik, M. & Beskok, A. Wetting characterisation of silicon (1 , 0 , 0) surface. **7022**, (2013).

40. Ai, Y. *et al.* DC electrokinetic particle transport in an l-shaped microchannel. *Langmuir* **26**, 2937–2944 (2010).

41. Koklu, M., Park, S., Pillai, S. D. & Beskok, A. Negative dielectrophoretic capture of bacterial spores in food matrices. *Biomicrofluidics* **4**, (2010).

42. Zhang, Y., Park, S., Yang, S. & Wang, T. An all-in-one microfluidic device for parallel DNA extraction and gene analysis. 1043–1049 (2010) doi:10.1007/s10544-010-9458-6.

43. Park, S., Zhang, Y., Wang, T. H. & Yang, S. Continuous dielectrophoretic bacterial separation and concentration from physiological media of high conductivity. *Lab Chip* **11**, 2893–2900 (2011).

44. Barisik, M. & Beskok, A. International Journal of Thermal Sciences Temperature dependence of thermal resistance at the water / silicon interface. *Int. J. Therm. Sci.* **77**, 47–54 (2014).

45. Gu, W., Cheng, P., Ghosh, A., Liao, Y. & Liao, B. Detection of distributed static and dynamic loads with electrolyte-enabled distributed transducers in a. doi:10.1088/0960-1317/23/3/035015.

46. Ghorbanian, J. & Beskok, A. Scale effects in nano - channel liquid flows. *Microfluid. Nanofluidics* **20**, 1–11 (2016).

47. Ghorbanian, J. A phenomenological continuum model for force-driven nano-channel liquid flows. *J. Chem. Phys.* **184109**, (2016).

48. Koklu, A., Sabuncu, A. C. & Beskok, A. Electrochimica Acta Rough Gold Electrodes for Decreasing Impedance at the Electrolyte / Electrode Interface. *Electrochim. Acta* **205**, 215–225 (2016).

49. Enhancement of dielectrophoresis using fractal gold nanostructured electrodes. 1458–1465 (2017) doi:10.1002/elps.201600456.

50. Mansoorifar, A., Koklu, A., Raj, G. V & Beskok, A. Electrical Impedance Measurements of Biological Cells in Response to External Stimuli. (2018) doi:10.1021/acs.analchem.7b05392.

51. Mansoorifar, A., Koklu, A. & Beskok, A. Quantification of cell death using an impedance-based microfluidic device. *Anal. Chem.* **91**, 4140–4148 (2019).

52. Heller, M. J. An Active Microelectronic Device For Multiplex DNA Analysis. *IEEE Eng. Med. Biol.* **104**, (1996).

53. Edman, C. F. *et al.* Electric field directed nucleic acid hybridization on microchips. **25**, 4907–4914 (1997).

54. Heller, M. J. Rapid determination of single base mismatch mutations in DNA hybrids by direct electric field control. **94**, 1119–1123 (1997).

55. Active Microelectronic Arrays for DNA Hybridization Analysis" in DNA Microarrays: A Practical Approach. *Oxford Univ. Press* (1999).

56. An Integrated Microelectronic Hybridization System for Genomic Research and Diagnostic Applications", in Micro Total Analysis Systems. *Kluwer Acad. Publ.* (1998).

57. Heller, M. J. & Forster, A. H. Active microelectronic chip devices which utilize controlled electrophoretic fields for multiplex DNA hybridization and other genomic applications

Nucleic acids. 157–164 (2000).

58. Sosnowski, R., Heller, M. J., Tu, E., Forster, A. H. & Radtkey, R. Active microelectronic array system for DNA hybridization , genotyping and pharmacogenomic applications. **12**, 181–192 (2002).

59. Cheng, J. *et al.* Preparation and hybridization analysis of DNA/RNA from E.coli on microfabricated bioelectronic chips. **16**, 541–546 (1998).

60. Cheng, J., Sheldon, E. L., Wu, L., Heller, M. J. & O'Connell, J. P. Isolation of cultured cervical carcinoma cells mixed with peripheral blood cells on a bioelectronic chip. *Anal. Chem.* **70**, 2321–2326 (1998).

61. Huang, Y. *et al.* Dielectrophoretic cell separation and gene expression profiling on microelectronic chip arrays. *Anal. Chem.* **74**, 3362–3371 (2002).

62. Krishnan, R., Sullivan, B. D., Mifflin, R. L., Esener, S. C. & Heller, M. J. Alternating current electrokinetic separation and detection of {DNA} nanoparticles in high-conductance solutions. *Electrophoresis* **29**, 1765–1774 (2008).

63. Krishnan, R. *et al.* Interaction of nanoparticles at the {DEP} microelectrode interface under high conductance conditions. *Electrochem. commun.* **11**, 1661–1666 (2009).

64. Hoerter, J. A. H., Krishnan, V., Lionberger, T. A. & Walter, N. G. siRNA-like double-stranded RNAs are specifically protected against degradation in human cell extract. *PLoS One* **6**, e20359 (2011).

65. Sonnenberg, A., Marciniak, J. Y., Krishnan, R. & Heller, M. J. Dielectrophoretic isolation of {DNA} and nanoparticles from blood. *Electrophoresis* **33**, 2482–2490 (2012).

66. Sonnenberg, A. *et al.* Dielectrophoretic isolation and detection of cfc-DNA nanoparticulate

biomarkers and virus from blood. *Electrophoresis* **34**, 1076–1084 (2013).

67. Sonnenberg, A. *et al.* Rapid electrokinetic isolation of cancer-related circulating cell-free DNA directly from blood. *Clin. Chem.* **60**, 500–509 (2014).

68. Ibsen, S. *et al.* Recovery of Drug Delivery Nanoparticles from Human Plasma Using an Electrokinetic Platform Technology. *Small* **11**, 5088–5096.

69. Ibsen, S. D. *et al.* Rapid Isolation and Detection of Exosomes and Associated Biomarkers from Plasma. (2017) doi:10.1021/acsnano.7b00549.

70. Lewis, J. M., Heineck, D. P. & Heller, M. J. Detecting cancer biomarkers in blood: challenges for new molecular diagnostic and point-of-care tests using cell-free nucleic acids. **15**, 1187–1200.

71. Lewis, J. M. *et al.* Integrated Analysis of Exosomal Protein Biomarkers on Alternating Current Electrokinetic Chips Enables Rapid Detection of Pancreatic Cancer in Patient Blood. *ACS Nano* **12**, 3311–3320 (2018).

72. Lewis, J. *et al.* A Pilot Proof-Of-Principle Analysis Demonstrating Dielectrophoresis (DEP) as a Glioblastoma Biomarker Platform. *Sci. Rep.* **9**, 1–10 (2019).

73. Zhao, K., Larasati, Duncker, B. P. & Li, D. Continuous Cell Characterization and Separation by Microfluidic Alternating Current Dielectrophoresis. *Anal. Chem.* **91**, 6304–6314 (2019).

74. Chen, X. *et al.* Microfluidic dielectrophoresis device for trapping, counting and detecting Shewanella oneidensis at the cell level. *Biosens. Bioelectron.* **99**, 416–423 (2018).

75. Su, I. H. *et al.* Dielectrophoresis System for Testing Antimicrobial Susceptibility of Gram-Negative Bacteria to β-Lactam Antibiotics. *Anal. Chem.* **89**, 4635–4641 (2017).

76. Chang, L. *et al.* Dielectrophoresis-assisted 3D nanoelectroporation for non-viral cell transfection in adoptive immunotherapy. *Lab Chip* **15**, 3147–3153 (2015).

77. Henslee, E. A., Sano, M. B., Rojas, A. D., Schmelz, E. M. & Davalos, R. V. Selective concentration of human cancer cells using contactless dielectrophoresis. *Electrophoresis* **32**, 2523–2529 (2011).

78. Douglas, T. A. *et al.* A feasibility study for enrichment of highly aggressive cancer subpopulations by their biophysical properties via dielectrophoresis enhanced with synergistic fluid flow. *Electrophoresis* **38**, 1507–1514 (2017).

79. Soltanian-Zadeh, S. *et al.* Breast cancer cell obatoclax response characterization using passivated-electrode insulator-based dielectrophoresis. *Electrophoresis* **38**, 1988–1995 (2017).

80. Elitas, M., Yildizhan, Y., Islam, M., Martinez-Duarte, R. & Ozkazanc, D. Dielectrophoretic characterization and separation of monocytes and macrophages using 3D carbon-electrodes. *Electrophoresis* **40**, 315–321 (2019).

81. Guillaume Mernier, Rodrigo Martinez-Duarte, Rajwinder Lehal , Freddy Radtke, P. R. Very High Throughput Electrical Cell Lysis and Extraction of. 574–581 (2012) doi:10.3390/mi3030574.

82. Jaramillo, M. D. C., Torrents, E., Martínez-Duarte, R., Madou, M. J. & Juárez, A. On-line separation of bacterial cells by carbon-electrode dielectrophoresis. *Electrophoresis* **31**, 2921–2928 (2010).

83. Iswardy, E. *et al.* A bead-based immunofluorescence-assay on a microfluidic dielectrophoresis platform for rapid dengue virus detection. *Biosens. Bioelectron.* **95**, 174–180 (2017).

84. Ding, J., Lawrence, R., Jones, P. & Hayes, M. A. Concentration of Sindbis virus with optimized gradient insulator-based dielectrophoresis. *R. Soc. Chem. Anal.* **141**, 1997–2008

(2016).

85. D'Amico, L., Ajami, N. J., Adachi, J. A., Gascoyne, P. R. C. & Petrosino, J. F. Isolation and concentration of bacteria from blood using microfluidic membraneless dialysis and dielectrophoresis. *Lab Chip* **17**, 1340–1348 (2017).

86. Yan, S. *et al.* Isolating plasma from blood using a dielectrophoresis-active hydrophoretic device. *Lab Chip* **14**, 2993–3003 (2014).

87. Yan, S. *et al.* On-chip high-throughput manipulation of particles in a dielectrophoresis-active hydrophoretic focuser. *Sci. Rep.* **4**, (2014).

88. Yang, F. *et al.* Extraction of Cell-Free Whole Blood Plasma Using a Dielectrophoresis-Based Microfluidic Device. *Biotechnol. J.* **14**, (2019).

89. Alinezhadbalalami, N., Douglas, T. A., Balani, N., Verbridge, S. S. & Davalos, R. V. The feasibility of using dielectrophoresis for isolation of glioblastoma subpopulations with increased stemness. *Electrophoresis* **40**, 2592–2600 (2019).

90. Tsutsui, H. *et al.* Efficient dielectrophoretic patterning of embryonic stem cells in energy landscapes defined by hydrogel geometries. *Ann. Biomed. Eng.* **38**, 3777–3788 (2010).

91. Bajaj, P., Marchwiany, D., Duarte, C. & Bashir, R. Patterned Three-Dimensional Encapsulation of Embryonic Stem Cells using Dielectrophoresis and Stereolithography. *Adv. Healthc. Mater.* **2**, 450–458 (2013).

92. Song, H. *et al.* Continuous-flow sorting of stem cells and differentiation products based on dielectrophoresis. *Lab Chip* **15**, 1320–1328 (2015).

93. Laux, E. M., Kaletta, U. C., Bier, F. F., Wenger, C. & Hölzel, R. Functionality of dielectrophoretically immobilized enzyme molecules. *Electrophoresis* **35**, 459–466 (2014).

94. Cao, Z. *et al.* Dielectrophoresis-Based Protein Enrichment for a Highly Sensitive Immunoassay Using Ag/SiO2 Nanorod Arrays. *Small* **14**, (2018).

95. Jones, P. V., Salmon, G. L. & Ros, A. Continuous Separation of DNA Molecules by Size Using Insulator-Based Dielectrophoresis. *Anal. Chem.* **89**, 1531–1539 (2017).

96. Barik, A. *et al.* Graphene-edge dielectrophoretic tweezers for trapping of biomolecules. *Nat. Commun.* **8**, (2017).

97. Shekhar, S., Stokes, P. & Khondaker, S. I. Ultrahigh density alignment of carbon nanotube arrays by dielectrophoresis. *ACS Nano* **5**, 1739–1746 (2011).

98. Collet, M. *et al.* Large-scale assembly of single nanowires through capillary-assisted dielectrophoresis. *Adv. Mater.* **27**, 1268–1273 (2015).

99. Seichepine, F., Rothe, J., Dudina, A., Hierlemann, A. & Frey, U. Dielectrophoresis-Assisted Integration of 1024 Carbon Nanotube Sensors into a CMOS Microsystem. *Adv. Mater.* **29**, (2017).

100. Tang, S. Y. *et al.* Creation of Liquid Metal 3D Microstructures Using Dielectrophoresis. *Adv. Funct. Mater.* **25**, 4445–4452 (2015).

101. Cha, S. H. *et al.* Fabrication of nanoribbons by dielectrophoresis assisted cold welding of gold nanoparticles on mica substrate. *Sci. Rep.* **9**, (2019).

102. Freer, E. M., Grachev, O., Duan, X., Martin, S. & Stumbo, D. P. High-yield self-limiting single-nanowire assembly with dielectrophoresis. *Nat. Nanotechnol.* **5**, 525–530 (2010).

103. Jose, J. *et al.* Individual Template-Stripped Conductive Gold Pyramids for Tip-Enhanced Dielectrophoresis. *ACS Photonics* **1**, 464–470 (2014).

104. Leiterer, C. *et al.* High precision attachment of silver nanoparticles on AFM tips by dielectrophoresis. *Anal. Bioanal. Chem.* **408**, 3625–3631 (2016).

105. Rabbani, M. T., Schmidt, C. F. & Ros, A. Single-Walled Carbon Nanotubes Probed with Insulator-Based Dielectrophoresis. *Anal. Chem.* **89**, 13235–13244 (2017).

106. Constantinou, M. *et al.* Rapid determination of nanowires electrical properties using a dielectrophoresis-well based system. *Appl. Phys. Lett.* **110**, (2017).

107. Rozynek, Z. *et al.* Formation of printable granular and colloidal chains through capillary effects and dielectrophoresis. *Nat. Commun.* **8**, (2017).

108. Ahadian, S. *et al.* Fabrication of poly(ethylene glycol) hydrogels containing vertically and horizontally aligned graphene using dielectrophoresis: An experimental and modeling study. *Carbon N. Y.* **123**, 460–470 (2017).

109. Becker, F. F. *et al.* Separation of human breast cancer cells from blood by differential dielectric affinity. *Proc. Natl. Acad. Sci. U. S. A.* **92**, 860–864 (1995).

110. Chan, K. L., Gascoyne, P. R. C., Becker, F. F. & Pethig, R. Electrorotation of liposomes: verification of dielectric multi-shell model for cells. **1349**, 182–196.

111. Asbury, C. L. & van den Engh, G. Trapping of {DNA} in nonuniform oscillating electric fields. *Biophys. J.* **74**, 1024–1030 (1998).

112. Washizu, M. & Kurosawa, O. Electrostatic Manipulation of DNA in Microfabricated Devices. *Trans. Ind. Appl.* **26**, 1165–1172 (1990).

113. Washizu, M., Kurosawa, O., Arai, I., Suzuki, S. & Shimamoto, N. Applications of electrostatic stretch-and-positioning of DNA. *IEEE T. Ind. Appl* **31**, 447–456 (1995).

114. Hölzel, R., Calander, N., Chiragwandi, Z., Willander, M. & Bier, F. F. Trapping single molecules by dielectrophoresis. *Phys. Rev. Lett.* **95**, 18–21 (2005).

115. Krishnan, R. & Heller, M. J. An {AC} electrokinetic method for enhanced detection of {DNA} nanoparticles. *J. Biophotonics* **2**, 253–261 (2009).

116. Manouchehri, S. *et al.* Dielectrophoretic recovery of {DNA} from plasma for the identification of chronic lymphocytic leukemia point mutations. *Int. J. Hematol. Oncol.* **5**, 27–35.

117. Ibsen, S. *et al.* Recovery of Drug Delivery Nanoparticles from Human Plasma Using an Electrokinetic Platform Technology. 5088–5096 (2015) doi:10.1002/smll.201500892.

118. Heller, M. J., Marciniak, J., Ibsen, S., Skowronski, E. & Sonnenberg, A. Dielectrophoretic (DEP) isolation and detection of cancer related cell Free DNA, RNA and exosome biomarkers from blood and plasma (Abstract # 600). *NSTI Adv. Mater. - TechConnect Briefs 2015* **3**, 71–74 (2015).

119. Sonnenberg, A. *et al.* Rapid Electrokinetic Isolation of Cancer-Related Circulating Cell-Free DNA Directly from Blood BACKGROUND : **509**, (2014).

120. Mccanna, J. P., Sonnenberg, A. & Heller, M. J. Low level epifluorescent detection of nanoparticles and DNA on dielectrophoretic microarrays. **873**, 863–873 (2014).

121. Heller, M. J., Krishnan, R. & Sonnenberg, A. Detection of Cancer-Related DNA Nanoparticulate Biomarkers and Nanoparticles in Whole Blood. in *TechConnect World 2010* 372–375 (2010).

122. De Peña, A. C. *et al.* Analysis of bacteriophages with insulator-based dielectrophoresis. *Micromachines* **10**, (2019).

123. Chae, Y. K. *et al.* Path toward Precision Oncology : Review of Targeted Therapy Studies and Tools to Aid in De fi ning " Actionability " of a Molecular Lesion and Patient Management Support. 2645–2656 (2017) doi:10.1158/1535-7163.MCT-17-0597.

124. Barbieri, C. E. *et al.* The Emergence of Precision Urologic Oncology : A Collaborative Review on Biomarker-driven Therapeutics. *Eur. Urol.* **71**, 237–246 (2017).

125. Mathai, R. A. *et al.* Potential Utility of Liquid Biopsy as a Diagnostic and Prognostic Tool for the Assessment of Solid Tumors : Implications in the Precision Oncology. 1–17 doi:10.3390/jcm8030373.

126. Mankoff, D. A., Farwell, M. D., Clark, A. S. & Pryma, D. A. Making Molecular Imaging a Clinical Tool for Precision Oncology A Review. **3**, 695–701 (2020).

127. Gerstung, M. *et al.* Precision oncology for acute myeloid leukemia using a knowledge bank approach. *Nat. Genet.* **49**, 332–340 (2017).

128. Yu, K. H. & Snyder, M. Omics profiling in precision oncology. *Mol. Cell. Proteomics* **15**, 2525–2536 (2016).

129. Monzon, F. A. *et al.* Multicenter validation of a 1,550-gene expression profile for identification of tumor tissue of origin. *J. Clin. Oncol.* **27**, 2503–2508 (2009).

130. Cohen, R. L. & Settleman, J. From cancer genomics to precision oncology - Tissue's still an issue. *Cell* **157**, 1509–1514 (2014).

131. Gallo, A., Tandon, M., Alevizos, I. & Illei, G. G. The majority of microRNAs detectable in serum and saliva is concentrated in exosomes. *PLoS One* **7**, 1–5 (2012).

132. Zhou, H. *et al.* Circulating RNA as a novel tumor marker: An in vitro study of the origins and characteristics of extracellular RNA. *Cancer Lett.* **259**, 50–60 (2008).

133. Lässer, C. *Identification and analysis of circulating exosomal microRNA in human body fluids*. *Methods in Molecular Biology* vol. 1024 (2013).

134. Théry, C. *et al.* Minimal information for studies of extracellular vesicles 2018 (MISEV2018): a position statement of the International Society for Extracellular Vesicles and update of the MISEV2014 guidelines. *J. Extracell. Vesicles* **7**, (2018).

135. Caby, M. P., Lankar, D., Vincendeau-Scherrer, C., Raposo, G. & Bonnerot, C. Exosomal-like vesicles are present in human blood plasma. *Int. Immunol.* **17**, 879–887 (2005).

136. Muller, L., Hong, C.-S., Stolz, D. B., Watkins, S. C. & Whiteside, T. L. Isolation of biologically-active exosomes from human plasma. *J. Immunol. Methods* **411**, 55–65 (2014).

137. Whiteside, T. L. The potential of tumor-derived exosomes for noninvasive cancer monitoring. *Expert Rev. Mol. Diagn.* **15**, 1293–1310 (2015).

138. Liang, K. *et al.* Nanoplasmonic quantification of tumour-derived extracellular vesicles in plasma microsamples for diagnosis and treatment monitoring. *Nat. Biomed. Eng.* **1**, 1–11 (2017).

139. Im, H. *et al.* Label-free detection and molecular profiling of exosomes with a nano-plasmonic sensor. *Nat. Biotechnol.* **32**, 490–495 (2014).

140. Etayash, H., McGee, A. R., Kaur, K. & Thundat, T. Nanomechanical sandwich assay for multiple cancer biomarkers in breast cancer cell-derived exosomes. *Nanoscale* **8**, 15137–15141 (2016).

141. Zhao, Z., Yang, Y., Zeng, Y. & He, M. A microfluidic ExoSearch chip for multiplexed exosome detection towards blood-based ovarian cancer diagnosis. *Lab Chip* **16**, 489–496 (2016).

142. Ilkhani, H., Sarparast, M., Noori, A., Bathaie, S. Z. & Mousavi, M. F. Electrochemical aptamer/antibody based sandwich immunosensor for the detection of EGFR, a cancer biomarker, using gold nanoparticles as a signaling probe. *Biosens. Bioelectron.* **74**, 491–497 (2015).

143. Jeong, S. *et al.* Integrated Magneto-Electrochemical Sensor for Exosome Analysis. *ACS Nano* **10**, 1802–1809 (2016).

144. Sarno, B. G., Heineck, D. P., Heller, M. & Ibsen, S. D. Dielectrophoresis: Developments and Applications from 2010 to 2020. *Electrophoresis* (2020).

145. Wan, Y., Cheng, G., Lui, X. & Hao, S.-J. Rapid Magnetic Isolation of EV via Lipid-based nanoprodes. *Nat. Biomed. Eng.* **47**, 549–562 (2017).

146. Thind, A. & Wilson, C. Exosomal miRNAs as cancer biomarkers and therapeutic targets. *J. Extracell. Vesicles* **5**, 1–11 (2016).

147. Medina, E. & Pieper, D. H. *Tackling threats and future problems of multidrug-resistant bacteria*. *Current Topics in Microbiology and Immunology* vol. 398 (2016).

148. Microbiology Society. The history of antibiotics | Microbiology Society. 1 https://microbiologysociety.org/members-outreach-resources/outreach-resources/antibiotics-unearthed/antibiotics-and-antibiotic-resistance/the-history-of-antibiotics.html%0Ahttps://microbiologysociety.org/members-outreach-resources/outreach-resources/antib (2017).

149. Last, J. M. *A Dictionary of Public Health*. (Westminster College, Pennsylvania: Oxford University Press, 2007).

150. Nobelprize. Paul Ehrlich - Biographical. *Nobleprize* 1 https://www.nobelprize.org/prizes/medicine/1908/ehrlich/biographical/%0Ahttp://www.nobelprize.org/nobel_prizes/medicine/laureates/1908/ehrlich-bio.html (2014).

151. Kaufmann, S. H. E. Immunology's foundation: The 100-year anniversary of the Nobel Prize to Paul Ehrlich and Elie Metchnikoff. *Nat. Immunol.* **9**, 705–712 (2008).

152. Aminov, R. I. A brief history of the antibiotic era: Lessons learned and challenges for the future. *Front. Microbiol.* **1**, 1–7 (2010).

153. Banerjee, S. *et al.* The ovarian cancer oncobiome. *Oncotarget* **8**, 36225–36245 (2017).

154. Fan, X. *et al.* Human oral microbiome and prospective risk for pancreatic cancer: A population-based nested case-control study. *Gut* **67**, 120–127 (2018).

155. Yan, X. *et al.* Discovery and validation of potential bacterial biomarkers for lung cancer. *Am. J. Cancer Res.* **5**, 3111–3122 (2015).

156. Singh, J. *et al.* Bifidobacterium longum, a lactic acid-producing intestinal bacterium inhibits colon cancer and modulates the intermediate biomarkers of colon carcinogenesis. *Carcinogenesis* **18**, 833–841 (1997).

157. Adler, H. I., Fisher, W. D., Cohen, A. & Hardigree, A. A. MINIATURE escherichia coli CELLS DEFICIENT IN DNA. *Proc. Natl. Acad. Sci.* **57**, 321–326 (1967).

158. Mayrand, D. & Grenier, D. Biological activities of outer membrane vesicles. *Can. J. Microbiol.* **35**, 607–613 (1989).

159. Tudor, J., Hashimoto, T. & Conti, S. F. Presence of nuclear bodies in some minicells of Escherichia coli. *J. Bacteriol.* **98**, 298–299 (1969).

160. Giacalone, M. J., Sabbadini, R. A., Chambers, A. L., Pillai, S. & McGuire, K. L. Immune responses elicited by bacterial minicells capable of simultaneous DNA and protein antigen delivery. *Vaccine* **24**, 6009–6017 (2006).

161. Kuehn, M. J. & Kesty, N. C. Bacterial outer membrane vesicles and the host-pathogen interaction. *Genes Dev.* **19**, 2645–2655 (2005).

162. Cameron, S. J. S. *et al.* A pilot study using metagenomic sequencing of the sputum microbiome suggests potential bacterial biomarkers for lung cancer. *PLoS One* **12**, 1–17 (2017).

163. Zhou, B. *et al.* The biodiversity Composition of Microbiome in Ovarian Carcinoma Patients. *Sci. Rep.* **9**, 1–11 (2019).

164. Zhang, J., Mi, L., Wang, Y. & Zhang, D. Detection of Bacterial DNA in Serum from Colon Cancer Patients: Association with Cytokine Levels and Cachexia. *J. Cancer Ther. Res.* **1**, 19 (2012).